DESIGN OF FABRICATION FRIENDLY & HIGHLY SENSITIVE SURFACE PLASMON RESONANCE-BASED PHOTONIC CRYSTAL FIBER BIOSENSORS

by

Md. Moinul Islam Khan (160021011)
Fariha Mehjabin (160021095)
Jubair Alam Chowdhury (160021085)
Mohibul Islam (160021077)

A Thesis Submitted to the Academic Faculty in Partial Fulfillment of the Requirements for the Degree of

BACHELOR OF SCIENCE IN ELECTRICAL AND ELECTRONIC ENGINEERING

Department of Electrical and Electronic Engineering
Islamic University of Technology (IUT)
Gazipur, Bangladesh

March 2021

DESIGN OF FABRICATION FRIENDLY & HIGHLY SENSITIVE SURFACE PLASMON RESONANCE-BASED PHOTONIC CRYSTAL FIBER BIOSENSORS

Approved by:

Prof. Dr. Mohammad Rakibul Islam

Supervisor and Professor
Department of Electrical and Electronic Engineering
Islamic University of Technology (IUT)
Boardbazar, Gazipur-1704.

Date: ……

Table of Contents

ACKNOWLEDGEMENTS

All praise to the almighty Allah (SWT), for He, has kept us alive in this COVID-19 pandemic and given us the capability and opportunity to finish this work perfectly with extraordinary results. It would not have been possible for us to finish this work without His blessings. Secondly, our heartfelt gratitude goes to our honorable supervisor, Professor Dr Mohammad Rakibul Islam, for his continuous support, helpful attitude, and most importantly, his constant patience during the learning phases. Without his motivation and guidance, we could not have come this far. We are also grateful to all the teachers of the Electrical and Electronic Engineering Department for their helpful attitude, valuable suggestions, and constructive criticism during the research work. After that, thanks to all our family members for supporting us in every phase of our life. Finally, we want to convey our gratitude to all the seniors, juniors, and well-wishers who have helped us accomplish our goal.

ABSTRACT

Many researchers have shown their excellence in the field of PCF-based SPR biosensors. In recent years, great designs showing high sensing performance have been proposed. However, the challenge for designing is that most of the designs either exhibit high sensitivity but have a drawback of having higher confinement loss or showing low sensitivity with lower loss. Most importantly, the designs may become complicated in order to achieve high sensitivities. We tried to minimize this tradeoff, gained higher sensitivities with considerably lower losses, and made four unique designs. Our research is distinctive, and the PCF-SPR biosensors are easy to fabricate and highly sensitive. All of our prototypes have a strategic pattern of circular air holes inside the fiber, which leads to a superior sensing performance. The evaluation of all the sensor characteristics has been done by employing the finite element method (FEM) of COMSOL Multiphysics. The gold (Au) layer used just around the fiber in our designs acts as the plasmonic material, and the layer of TiO_2 increases the adhesivity of the gold and the fiber. We have optimized all the fiber parameters to achieve the best result in terms of sensitivity. We derived a maximum amplitude sensitivity (AS) of 5060 RIU^{-1} with a maximum sensor resolution of 1.98×10^{-6} from one sensor. The same sensor exhibited a maximum wavelength sensitivity (WS) of 41500 nm/RIU with a maximum sensor resolution of 2.41×10^{-6}. Moreover, the maximum figure of merit (FOM) procured was 1068.7 for this sensor. This sensor has also shown a fabrication tolerance limit of ±10%. Additionally, the temperature and strain sensitivities of that sensor are estimated to be 0.75 nm/°C and 3 pm/με, respectively, along with a resolution (temperature) of 1.33×10^{-1} °C. Another sensor of ours showed an excellent birefringence of 2.23×10^{-3}, whereas all other performance parameter values were almost identical. One of the remaining sensors exhibited extremely low confinement loss. The maximum value of confinement loss for that sensor was found to be 3.73 dB/cm, which is extraordinary. The last sensor is exceptional in the sense that we have analyzed its performance for two different plasmonic materials (Gold and AZO) and found that it can sense analytes with very low refractive indices when AZO is used. The overall analyte sensing range of all our sensors is 1.31 to 1.43. All the designs are discussed elaborately in our thesis in the upcoming chapters. With their enhanced performance in terms of sensitivity, we believe that our SPR based PCF biosensors can potentially contribute a lot in detecting unknown analytes and medical diagnostics applications.

List of Tables

List of Figures

List of Equations

List of Acronyms

AI	Amplitude Interrogation
ALD	Atomic Layer Deposition
AS	Amplitude Sensitivity
AZO	Aluminium doped Zinc Oxide
CL	Confinement Loss
CVD	Chemical Vapor Deposition
DNA	Deoxyribonucleic Acid
DWDM	Dense Wave Division Multiplexing
EM	Electro-Magnetic
EML	Effective Material Loss
FEM	Finite Element Method
FOM	Figure of Merit
FWHM	Full Width at Half Maximum
HDPE	High Density Poly Ethylene
IR	Infra-Red
ITO	Indium Tin Oxide
m-RNA	Messenger RNA
PBG	Photonic Band Gap
PCF	Photonic Crystal Fiber
PML	Perfectly Matched Layer
PMMA	Poly Methyl Methacrylate
RI	Refractive Index
RIU	Refractive Index Unit

RNA	Ribonucleic Acid
RW	Resonance Wavelength
SPP	Surface Plasmon Polariton
SPR	Surface Plasmon Resonance
SPW	Surface Plasmon Wave
TiN	Titanium Nitride
TIR	Total Internal Reflection
TM	Transversely Magnetic
WI	Wavelength Interrogation
WS	Wavelength Sensitivity

List of Symbols

n_{eff}	Effective Refractive Index
n	Real Part of Effective Refractive Index
k	Imaginary Part of Effective Refractive Index
n_{silica}	Refractive Index of Silica without Strain
n'_{silica}	Refractive Index of Silica with Strain
λ	Wavelength of Light
B_1	Sellmeier Constant
B_2	Sellmeier Constant
B_3	Sellmeier Constant
C_1	Sellmeier Constant
C_2	Sellmeier Constant
C_3	Sellmeier Constant
T	Temperature
ε_z	Strain
P_e	Elastic-optic Constant
ε_{Au}	Permittivity of Gold
ε_∞	High-frequency Permittivity
ω	Angular Frequency
ω_D	Plasma Frequency
γ_D	Damping Frequency
$\Delta\varepsilon$	Weighting Factor
Γ_L	Spectral Width
Ω_L	Oscillator Strength

n_t	Refractive Index of TiO_2
ε_b	Background Permittivity
α	Confinement Loss
k_0	Wavenumber
S_A	Amplitude Sensitivity
S_λ	Wavelength Sensitivity
R	Resolution
B	Birefringence
L	Sensor Length
S_T	Temperature Sensitivity
$S_{\varepsilon z}$	Strain Sensitivity
p	Pitch
d	Diameter
h	Height
w	Width
t_{PML}	PML Thickness
t_a	Analyte Layer Thickness
t_g	Gold Layer Thickness
t_t	TiO_2 Layer Thickness
r_c	Radius of the Sensor Core
Λ	Distance between two air hole centers
a	Air Hole Center to Cluster Center Distance
p_1	Fiber Center to Cluster Center Distance

Chapter 1

Introduction

1.1 Background

The biosensor is referred to as an analytical device that integrates a biological sensing element (enzyme, antibody, or nucleic acid) with a physical (mass, optical, or electrochemical) transducer, where the resultant signal is further converted into an electronic one (figure 1.1) [1]. In recent years, due to having the intense and advanced research potentiality, the application field of biosensors has been grown exponentially. The biosensors can be categorized into six different groups based on the signal transduction method: mass, optical, magnetic, electrochemical, thermal, and micromechanical sensors. The optical sensors [2]–[5] are the most impressive inventions in sensing applications.

Optical biosensors offer distinct advantages over many other profiling technologies applied for monitoring and analyzing molecular interactions. It represents the most common type of biosensor, which has drawn the researcher's attention for the past couple of decades due to its wide range of application in the various established fields such as drug discovery, healthcare, food quality control, biotechnology industry, and environmental safety monitoring [6]–[10]. As it has instant sensing ability, which makes this sensor an efficient and advanced one. Also, due to compact size, high sensitivity, accuracy, immunity to external disturbance, and cost-effectiveness of the sensors, it has become a favored option for the researcher's community to explore.

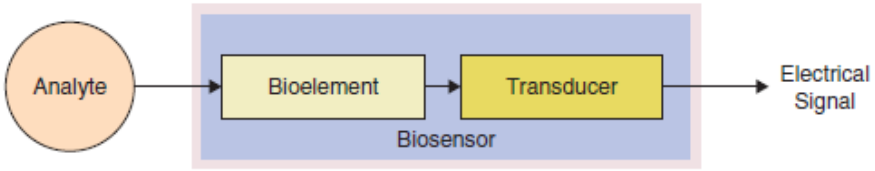

Figure 1.1: A biosensor's schematic representation

In 1970, optical fiber was first invented by Corning Glass Works. Then GaAs semiconductor lasers were simultaneously discovered to transmit the light through the links of fiber optic. After that, in 1975, the original fiber optic framework was created where GaAs semiconductor lasers were utilized. The second era of fiber optic communication was initiated

in the mid-1980s where scientists have worked with InGaAsP semiconductor lasers. With the advancement of technology, fiber optic communication has currently entered into its fifth era, where the correspondence frameworks employ the DWDM (Dense Wave Division Multiplexing) method for increasing the information rates.

Optical biosensors basically depend on the intensity of light or magnetic field as a result of biochemical interaction. This biosensor's main working principle is it transforms the incident light rays into electrical signals, which can detect the intensity of electromagnetic waves and sense the change of the corresponding analyte. The scientists have exploited different methods such as interferometry (reflectometric white light interferometry [11] and modal interferometry in optical waveguide structures [12]), fluorescence spectroscopy [13], spectroscopy of guided modes of optical waveguides (grating coupler [14], resonant mirror [15]) and surface plasmon resonance (SPR) [6], [16].

Based on the sensing technique, this optical method can be divided into two groups. The first one is label optical biosensor which includes fluorescence-based biosensors where multi-step detection protocols are needed. This method also requires washing steps and additions of reagents. However, it shows some limitations like toxic waste, reduction in efficiency, short-term stability, time-consuming, degradation of the biomolecule, and so on. The other one is renowned as the label-free technology. Here, it can allow real-time monitoring without the need for labeling. Moreover, this technique has the capability to generate a signal directly without additionally added probes that carry labels to provide the signals [17], [18]. SPR, resonant mirrors, and interferometers maintain the label-free technology for higher accuracy and efficiency. SPR-based optical sensors have played a predominant role in the development of fiber-optic communication. We are experiencing a conspicuous impact of surface plasmon resonance based biosensors in a diverse range of applications in real life for the past couple of decades.

Surface plasmons are defined as the rise of the quantized TM (transversely magnetic) p-polarized electromagnetic wave because of the incident of the combined oscillation of electrons, which takes place at the metal-dielectric interface [19]. Matching of the wave vector of the incident wave and that of surface plasmon results in a phenomenon called surface plasmon resonance [20]. SPR mainly occurs as a result of the incident of transverse magnetic (TM) wave, which excites the electrons within the metal–dielectric interface. Therefore, surface plasmon wave (SPW) is developed and circulated through the core-cladding region. In this condition, at a very particular wavelength, leaky core mode happens to couple with surface plasmon polariton (SPP) mode. This specific wavelength is termed resonance wavelength

(RW), and this condition is known as the phase-matching condition [21]. The SPP mode and the phase-matching state are susceptible to the analyte refractive index (RI), and with the slight change in the environmental RI, the RW gets potentially deviated to either a higher or lower wavelength. Thus, the analyte can be identified precisely by perceiving the fluctuation of the resulting RW considering various analyte RI [22].

SPR-based optical sensors have drawn the intense attention of researchers because of their unique and well-established characteristics, high robustness, compact and straightforward probe design as well as higher sensitivity. Owing to the advantageous behavior of SPR sensors, they are being explored in numerous fields, for instance, maintaining water quality, food safety observation, glucose inspection, medical diagnostics, real-time monitoring, gas detection, biosensing, strain sensing, and temperature sensing [6]–[10], [23]–[27]. Additionally, the integration of nano-electronic and nano-photonic components for obtaining ultra-compact optoelectronic devices is made possible due to SPR technology [28], [29].

The exploration of SPR based biosensors started in 1983 when Liedberg *et al.* introduced SPR biosensors in the field of gas detection and biosensing [23] and presented the method which is renowned as the prism-coupling. Prism-based SPR sensors work based on point cross-examination technique. However, the prism-based SPR sensor is ineligible to use in remote sensing because it includes different optical and mechanical parts, which makes the sensor bulky in size. To limit these constraints, researchers have replaced the prism with fiber, which has gained importance because of the promising features like atypical dispersion, high nonlinearity, endless single-mode behavior, label-free detection, adjustable high birefringence, and also high integrity and portability [30], [31]. Therefore, fiber-based sensors are suitable for remote sensing. After diverse research, an improved version of the sensor is invented, renowned as a photonic crystal fiber (PCF)-based SPR sensor. It can provide higher sensitivity and lower resonance peak than other fiber-based sensors [32]–[37], which results in better accuracy when detecting an unknown analyte. Moreover, the PCF-based sensors can surely entitle a better authority on the transient field by altering the structural parameters like pitch, the bore of the air holes, and the total count of different shaped rings and air cavities.

1.2 Problem Statement

SPR sensors have attained significant attention from researchers due to their suitability for desired sensing applications and promising characteristics. To date, numerous numbers of optical sensors based on SPR techniques are explored. Basically, the sensors are employing

two types of sensing mechanisms. The conventional one is the internally metal-coated PCF sensor, where the metal film is coated internally [38]. This mechanism has some cons, such as emptying and re-filling the fiber is time-consuming. Moreover, the internally coated layer is very delicate, making the fabrication and structure a complex one. It also needs extra steps and maintenance to operate perfectly, making it unsuitable for easier sensing. A D-shaped PCF sensor with improved structure is suggested to limit the impediments. However, this type of sensor adds fabrication complexity [39]. The flat portion needs perfect polishing to get an accurate result which makes the fabrication process even more difficult as well as expensive. The modern sensing approach is the externally metal-coated PCF, where the metal coating is placed outside the fiber. The most common plasmonic materials that are used in these sensing processes are gold, silver, aluminum, etc. Most of the plasmonic materials get oxidized due to an aqueous environment, resulting in a decrease in sensing accuracy [40]. Based on the placement and size of the air holes, the fabrication complexity of the sensor as well as the costing can be increased. To sum up, the limitations encountered in previously reported SPR based sensors are as follows:

- Complex design
- Fabrication adversity
- Higher confinement loss
- Weak evanescent field
- Inaccurate sensing behavior
- Uneconomical costing

1.3 Research Objective

The initial phase of the optical sensors was based on the transmission sector. But the latest EML value achieved has the lowest value of 0.009 [41]. So, further decrement of the value is unnecessary because that will only cause complicacy in the design structure. The same scenario goes for the confinement loss and other parameters. That is why this transmission field has become a saturated one with almost no scope for further improvement. Thus, researchers

are nowadays giving less attention to this sector because SPR is more promising and has a lot of opportunities to research than transmission applications.

Our research's main objective was to design and investigate the influence of novel and unique designs of PCF biosensors based on SPR. The specific aims of the research are as follows:

- ✓ To measure amplitude sensitivity (AS) & wavelength sensitivity (WS) from refractive index changing the range of wavelength.
- ✓ Conducting an in-depth literature review related to SPR sensors.
- ✓ Use of plasmonic materials externally of the PCF structure for more accurate detection & better performance.
- ✓ Investigation of the performance and graphical outcomes due to small changes in different parameters.
- ✓ Simulation of different parameters by changing the thickness of different fiber layers like Gold, Titanium dioxide (TiO_2) and analyte, etc.
- ✓ Comparison between our proposed PCF-SPR sensors with other sensors of different journals.

1.4 Motivation

The PCF sensors based on SPR technology have been a focus to the researchers due to their advantageous characteristics. The sensitivity of this type of sensor depends on the evanescent field, which is indicated towards the cladding region through the core, and that causes the free electrons to oscillate, and SPW is created along the metal-dielectric surface. In that instance, the phase matching situation occurs and makes it dependable on even a slight change in analyte RI. With the change of RI, the fluctuations of RW are determined and further observed in a graphical form.

SPR is considered a field that is yet to explore. This sector has extraordinary scope for further improvement. So, scientists are still making an effort to make it useful to the fullest. These biosensors present highly sensitive, compact, and high-frequency monitoring without any sample pre-treatment steps that are time-consuming.

The application field of these sensors ranges from biochemical and biotechnological fields to healthcare, security, etc. As we can observe, this technique is so versatile that it has a vast and spectacular area of implications. Therefore, the proper emphasis should be given to the nourishment of this technology. This sensor has an established analysis method that can

take a few minutes to produce the result with accuracy, whereas the other sensors previously used in laboratories were very delicate, time-consuming and the maintenance cost was huge. Additionally, these biosensors can be used to assay bacteria, virus, antibody-antigen, DNA, mRNA, RNA, hormone, hemoglobin, protein, etc. If we talk about the upcoming research opportunities, it has shown a promising behavior which includes an ambition to further use in the near future in electronics, physics, medical analyses, and software. Thus, at present, SPR is labeled as the most auspicious area of performing research work.

1.5 Thesis Framework

This thesis report is constructed with eleven distinct chapters. A brief synopsis of the upcoming ten chapters is provided in this section.

Chapter 2 presents a detailed discussion on PCF and the classifications of it. The background history is also analyzed in this segment. The reason behind PCF-based sensors came into being, and the cause of having superiority over other techniques is specified here. Finally, the algorithm, method, and software used to achieve the graph and simulations are also enlisted.

Chapter 3 gives a brief description of SPR technology. Here, the information about the working principle of SPR is remarked. Also, an overview of evanescent field, SPP, SPW, resonance, implementations of SPR based sensors is shown in this chapter.

Chapter 4 contains the analysis and detailed information regarding SPR based PCF sensors and the reason behind why it has become the popular choice among the researcher's community. Different categories of sensors such as prism-based, D-shaped, and sensors based on several sensing techniques (internal, external) are also brought into the light. Here, the comparison between several types of sensors using the plasmonic materials gold, silver and the necessary usage of additional coating (Graphene, TiN, TiO_2) is delivered.

Chapter 5 provides the basic terms and equations that are significant for optimization and analysis. The essential equations utilized for design purposes such as the Sellmeier equation (for RI of silica), Drude–Lorentz model equation (for RI of gold), and the equation for RI of TiO_2 are defined. For exploiting sensor performance, important parameters like FOM, amplitude sensitivity, confinement loss, wavelength sensitivity, resolution, birefringence,

sensor length, strain, and temperature sensitivity are needed, and they are also characterized in this chapter.

Chapter 6 depicts our proposed bi-polarized as well as a hexagonal lattice PCF-based SPR biosensor with ultra-high sensitivity where the air holes are arranged in a manner so that it can further improve the sensing performances of this sensor. Several fiber design parameters such as perfectly matched layer (PML), analyte, metallic channel thickness, pitch distance, and diameter of air holes are optimized to obtain the optimal sensing performances.

Chapter 7 portrays another research work of ours where we introduced a practically simple circular-shaped lattice, which is more beneficial in terms of practical fabrication. Here, gold is utilized to laminate the exterior of the design. An additional lean layer of TiO_2 is applied to emphasize the adhesion of the gold layer on the fiber as well as to achieve high sensitivity.

Chapter 8 represents the work in which we offered the external sensing approach of a PCF-SPR sensor with excellent sensitivity. The circular air cavities in the blueprint are disposed of in a strategic order to enhance the performance as a sensor as well as to make its fabrication feasible. The Finite Element Method (FEM) has been utilized to optimize all the fiber parameters like the gold and Titanium-di-oxide layer thicknesses, the air hole diameters to achieve the best sensitivity, and sensor resolution and birefringence.

Chapter 9 illustrates the design structure we have introduced a practically simple, regular circular-shaped cladding based PCF SPR biosensor where a thin layer of gold or AZO (2% wt of Al in ZnO) can be used as the plasmonic material which is deposited at the outer plane of the structure to enable external sensing and also to increase the flexibility. Variation of plasmonic layer thickness, area of PML, pitch, and diameter of the circle are surveyed to obtain the best results.

Chapter 10 demonstrates the available fabrication processes and the feasible methods to give it a physical shape. Some significant methods such as Stack and Draw Method are described. Also, the techniques used for fabrication, such as the Chemical Vapor Deposition Technique (CVD) and the Atomic Layer Deposition (ALD) Technique, are given importance for the enhancement of the sensitivity of a sensor.

Chapter 11 concludes with the conclusion, the future expectations as well as the aims and socio-economic impact.

Chapter 2

Photonic Crystal Fiber

2.1 Introduction

Photonic-crystal fiber (PCF) is a special class of optical fiber having excellent waveguiding properties. It has a better capability to confine light compared to the traditional optical fibers out there. Researchers have found a wide range of PCF applications like fiber optic interchanges, fiber lasers, non-linear gadgets, high control transmission, different gas sensors, data transmission in the THz regime, etc. PCFs generally are formed of a micro-structured arrangement having undoped silica as the background material, and air holes are present typically throughout the length of the fiber. The central region is known as the core, and cladding is the region surrounding the core. However, the background material used here is not limited to silica alone [42]. Different crystal fibers such as Teflon [43], PMMA [44], TOPAS [45], [46], HDPE [47] are commonly used. Among them, TOPAS is regarded as the most suitable material for waveguide propagation due to extraordinary water barrier properties [46], great biosensing characteristics [48]. For porous fiber, birefringence is one of the crucial parameters which is effective for polarization-maintaining sensing applications [49].

Now the structure of the core and cladding regions of a PCF carries a significant role in fiber performance. Initially, the honeycomb cladding structure was suggested by J. Laegsgaard *et al.* [50]. After that, a large number of designs have increased because of the improvement of design flexibility and fabrication facility. Some efficiently implemented designs are square [51], hexagonal [52], octagonal [53], spiral [54], circular [55] and hybrid [56]. In contrast to other fibers, substantial attention has been given to the porous core fibers due to their capability of maintaining low EML (effective material loss), high birefringence, and higher power into the core region simultaneously [57]. Thus, we can see a vast number of designs of PCF are possible, and good results can be obtained using photonic crystals.

2.2 PCF in Brief

A conventional optical fiber has a core that has a higher refractive index than the cladding. A high refractive index material is doped in the core region to make its refractive index higher than the silica cladding. Germanium is usually used to increase the refractive index of the core, and Fluorine is usually used to decrease the refractive index.

Photonic Crystal Fiber is a low-loss dielectric medium that is constructed using a periodic array of microscopic air holes, and it goes along the whole fiber length [58]. Light is trapped in the core in PCF, and it gives a better waveguide to photons than standard optical fiber. A solid silica core in PCF provides the core guidance of the optical signal. This core is surrounded by a periodic air-hole array in the cladding. As the effective cladding index is lower than the core refractive index, the light signal can be guided by total internal reflection along the silica defect core. The air-holes add up to the low index cladding, and the core is usually formed by making a larger air hole in its position or removing an air hole from the center of the structure. PCFs have some design freedom, like, core radius, number of rings, air hole diameter, and pitch (air hole to air hole distance). Application of guiding properties can be gained by modulating these parameters as the guiding properties of optical fibers depend on the refractive index, and the refractive index of PCFs depends on those design freedoms [59].

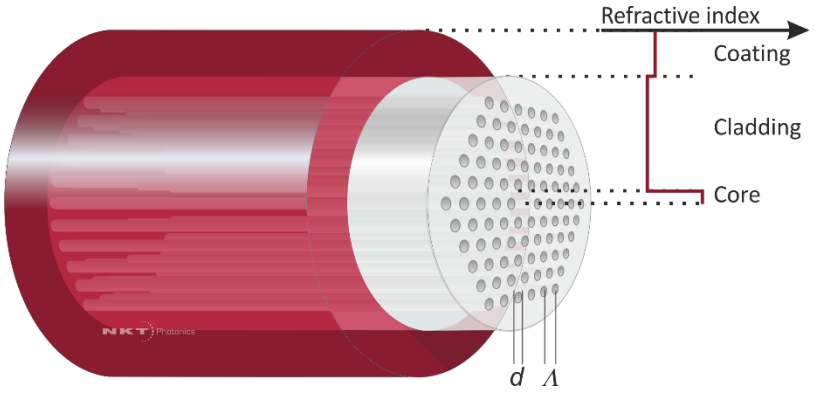

Figure 2.1: Cross-sectional view of a Photonic Crystal Fiber

2.2.1 Classification of PCF

In conventional fiber optics, there is a constant difference in the refractive indices of the core and the cladding region. Due to this difference, light-waves can easily travel across the core region by the phenomenon of refraction. But, in this case, as the distance of

propagation increases, the transmission loss also increases. So, we need to ensure the use of repeaters and amplifiers for communicating over long distances with better quality.

However, in the case of photonic crystal fibers (PCF), light-waves are entrapped within the core region, which ensures much better wave-guiding properties compared to the existing conventional optical fibers. The background material used in the case of photonic crystal fibers increases the flexibility of the fiber and also reduces the overall manufacturing cost. The fabrication procedure for PCFs is better than traditional optical fibers. There are generally two main classes of photonic crystal fibers:

- **Index-Guiding Fibers:** Here, a solid-core is present like the traditional ones. Light waves are entrapped within the core by the phenomenon of total internal reflection.
- **Photonic Bandgap (Air Guiding) Fibers:** These types of fibers contain periodic micro-structured arrangements and a low index material core. The refractive index in the core is lower compared to the cladding region made of photonic crystals. The light-waves are guided through the fiber with the process of photonic bandgap, which is different from total internal reflection.

2.2.2 High Index Guiding Fibers

M-TIR is the abbreviation of total internal reflection in the case of optical fibers. They depend on a high-index core, where generally pure silica is used, and the micro-structured providing the low refractive index surrounds it. This region of cladding is highly wavelength dependent which is not the same as pure silica, and due to this, photonic crystal fibers are very much different from conventional optical fibers. For example, as the refractive index is strongly dependent on wavelength, it facilitates us to design endless single-mode fibers, which only support a single mode regardless of the wavelength. Besides, we can easily manipulate the dispersion-properties of the fibers, which makes it possible to design optical-fibers having an irregular dispersion characteristic at visible wave-lengths.

As there is a combination of small cores and phase-matching condition which is similar to available sources, it is viable to create using the photonic crystal fiber technology a very coherent super-continuum generation. Now, it is possible to make optical fibers having large mode-field diameters having control over the refractive-index profile, which in turn facilitates higher beam-quality fiber guidance and amplification.

2.2.3 The Bandgap effect

It is another type of optical fiber with a mechanism different in properties from the M-TIR guiding optical-fibers. The strategic micro-structured arrangement in the cladding region of PBG fibers ensures the creation of photonic bandgaps. Here, the light-waves of a certain range of wavelengths cannot pass through the fibers. In the PBG fibers, the core regions are formed by creating a defect in the structure of the fiber, and thus it creates a region in which light can easily propagate. The light can only pass easily through the defective area as it creates a low index-guiding core. We cannot expect this type of advantage in the traditional fibers, and the low index-guiding characteristics of the photonic bandgap fibers create a large area of potential possibilities. So, in this process, we can guide light-waves through air or every compatible gas through the material of the fiber.

2.2.4 Hollow-Core and Solid-Core Fibers

Hollow-core fiber is one of the special classes of photonic bandgap fibers. Here the electromagnetic field is confined within an air-filled core. But through the air-core fibers, light is only guided in a limited spectrum like the other photonic bandgap fibers. The common bandwidth is 200 nm for fibers guiding around 1550 nm. Beneath this region is the anti-guiding core region.

There are many promising applications if we can guide light waves through hollow cores, such as we can deliver high power without risking the health of the fiber, we can sense different gases, and ensure very low-loss guidance through the vacuum. The hollow-core fibers have other advantageous properties, which are not usually found in the other traditional fibers. Their insensitivity to bending and overall diminished sensitivity to Kerr effect, transient behavior in case of temperatures, and the Faraday effect make them more useful. Moreover, they exhibit high dispersive properties like abnormal dispersion values. Here, the material inside the core contributes very little, so the overall dispersion of photonic bandgap fibers stays at a higher degree where the wave-guide dispersion dominates.

There is another important type of photonic bandgap guiding fibers which is known as the solid-core PBG fibers. In this class of fiber, the electromagnetic field is confined within a solid-core, and in the cladding regions, there are arrays of high-index regions embedded inside the material silica. These types of fibers can guide light waves through a limited region of the spectrum. The process of amplification and lasing can be done easily

by the filtering effect combining with a core doped with rare earth material like Yb at a newer wavelength with weaker fiber gain. This combination of doped-solid-core photonic bandgap fiber and the especially dispersive characteristics ensures a wide range of possibilities to the laser community.

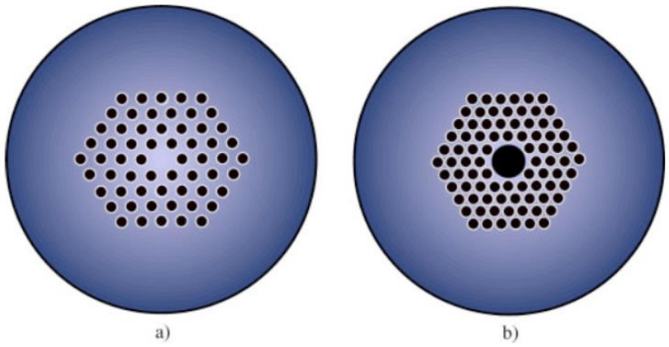

Figure 2.2: Cross-sectional view of (a) Solid Core Fiber, (b) Hollow Core Fiber

Chapter 3

Surface Plasmon Resonance

3.1 Introduction

SPR (surface plasmon resonance) is an optical phenomenon created when the desired frequency of the photons of propagating light and the frequency of the electrons of that surface match. A surface plasmon resonance (SPR)-based sensor identifies transient varieties within the refractive record at a point. The introduction of various standard gadgets for evaluating fabric adsorption onto planar metal (frequently gold or silver) surfaces or onto the exterior of metal nanoparticles is the focus of this biosensor.

3.2 Working Principle of SPR

SPR procedures energize and distinguish collective motions of free electrons (known as surface plasmons) in which light is centered onto a metal film through a glass crystal, and the consequent reflection is recognized at a particular angle of propagating light makes a faint line within the reflected beam which contains a riches of data. A move within the reflectivity bend speaks to an atomic official occasion taking put on or near the metal film, or a conformational alter within the atoms bound to the film. By checking this move vs. time, analysts can think about atomic official occasions and official energy without the bother of a name.

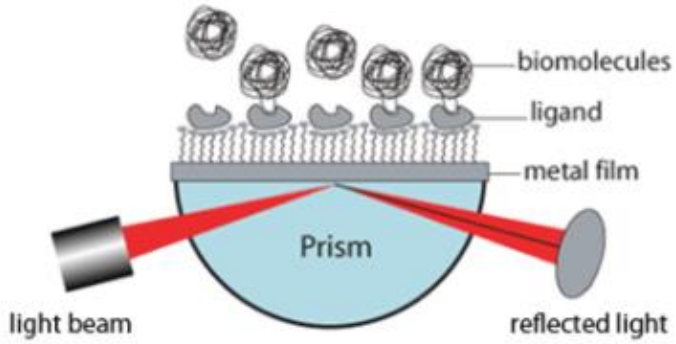

Figure 3.1: A light is impacted by a prism on a metal film and the reflected beam is captured and analyzed

3.3 Reason of Interest in SPR Technology

In recent years SPR based biosensor has drawn intense attention to the researchers due to its high robustness, high sensitivity, and well-established characteristics. Food safety, protection, medical testing, bimolecular analyte detection, and medical diagnostics are potential SPR technology applications [60]. Due to (i) the freedom to change optical parameters by design via the geometry of the structure, (ii) lightweight, and (iii) controllable birefringence, SPR modes enabled by PCF have gained considerable attention, making it suitable for a variety of sensing applications [20], [61]–[65].

3.4 Literature Review

The question may arise what SPW (surface plasmon wave) is and what about the evanescent field. In this portion, these questions will be discussed.

3.4.1 Surface Plasmon Wave

We have already become familiar with the SPR biosensor. In the SPR biosensor, a thin metal layer has been coated on glass, and a chip of sensor is added between the surface and the aqueous compartment. That metal is chosen to be gold for its chemical stability, and it also exhibits significant resonance peak shifts. When the propagating light passes through the substrate, the frequency matches the oscillation created of free electrons on the interface between the metal and dielectric. Moreover, it results in the surface plasmon wave. This SPW is quite sensitive as it can be differed by changing the refractive index. This surface plasmon wave is the main basis surface plasmon resonance.

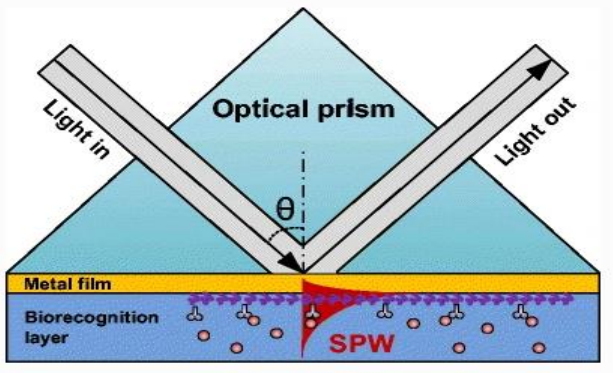

Figure 3.2: Review of Surface Plasmon Wave

3.4.2 Evanescent Field

As light is reflected at angles near the critical angle, a significant portion of the power is transmitted into the cladding or medium that surrounds the core. The evanescent wave is a phenomenon that lasts only a short distance from the interface and loses power exponentially as distance increases. The evanescent field has been used to enable real-time interrogation of surface-specific recognition events [66]. Fiber optics are also claimed to use absolute internal reflection to direct the light energy down the fiber, but a section of the internally reflected wave extends into the optical cladding a small distance beyond the core boundary. That is the evanescent wave's property, which can be exploited by removing the fiber cladding to allow the evanescent wave to expand into substances surrounding the fiber core beyond the core boundary.

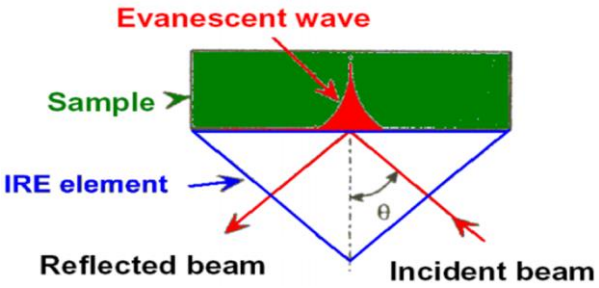

Figure 3.3: Evanescent Wave in Optical Fiber

3.5 Implementation of SPR

SPR can be used in different applications. Nowadays, especially in the medical sector, like for the diagnosis of the human hepatitis B virus, SPR plays an important role. Also, for the detection of biomolecular materials, SPR has been used. With the help of SPR, different biochemical samples have been tested. The presence of viruses in blood samples can easily be discovered. SPR allows the detection of molecular interactions in real-time and without the use of any labels. On the contrary, traditional sensors requiring labels for detection can answer questions on the binding specificity and possibly the affinity; SPR provides information on the specificity, affinity, kinetics, thermodynamics, and concentration of interaction for a wide range of molecules. The presence of harmful gases in a complex mixture can easily be found with the help of this biosensor within a very short time and at a very low cost.

3.6 Advantages of SPR

Although there is a range of bio-detecting devices available, SPR technology makes tracking restricted activity on a sub-atomic level easier and more accurate than at any other time in recent memory. Now here we will go through a few of the main benefits of using surface plasmon resonance:

- ✓ ***Label-Free Detection:*** SPR recognizes contrasts in the refractive record, so no name is needed for discovery. We may observe the bio-subatomic cooperation between a variety of proteins, DNA/RNA, and small particles in real-time.

- ✓ ***Small Sample Sizes:*** To run experiments, SPR needs an insignificant measure of the test. Researchers and some medical professionals would be able to use less expensive materials, save money, and make surface plasmon reverberation more affordable and usable.

- ✓ ***Reusable Sensor Chips:*** Another smart benefit of SPR is the ability to repurpose sensor chips. Sensor chips directly affect the nature of the data and are an integral component of bio detecting. With so much depending on the sensor chip's efficiency and execution, it is becoming increasingly important to remember that these chips can be reused.

- ✓ ***Ability to handle complex samples:*** Surface Plasmon reverberation can be used even in cases where only rough examples are available for research. SPR has been used for testing experiments in several muddled frameworks, including serum analysis.

- ✓ ***Real-time Monitoring:*** Essentially, using SPR technology allows researchers to see how various biomolecules interact over time in a simple and generally low-cost manner. It has many uses in the pharmaceutical and therapeutic industries and the fields of inherited qualities and electricity.

3.7 Success Rate and Drawbacks

A special reason for using high sensitivity SPR is its high success rate. Developing small molecule drugs is expensive, extremely time-consuming. The low success rates of other sensors have created the need to find and adopt novel ways to quickly and accurately measure their activity. Now, The SPR biosensor technology has a range of disadvantages also. To begin, keep in mind that biosensors depend on the presence of active biological molecules. Biosensors need the molecule to be active to produce a signal, unlike other analytical technologies such as mass spectrometry or UV spectrometry that can be used to characterize the substance, whether it is properly folded and active or not. Another downside is that, although biosensor instruments are relatively easy to use, designing and executing an assay also necessitates some biochemistry expertise.

Chapter 4

SPR based PCF Sensors

4.1 Overview

PCF-based sensors provide higher sensitivity and lower resonance peaks than other fiber-based sensors, which results in better accuracy when detecting an unknown analyte. Moreover, the PCF-based sensors can surely entitle a better authority on the transient field by altering the structural parameters like pitch, the bore of the air holes, and the total count of different shaped rings and air cavities. SPR is the preferred technique for attaining suitable sensing characteristics. When the SPR based technology merges with the benign feature, it evolves the desired SPR based PCF sensors.

Such a sensor functions based on SPR, and it eventuates when light passes through the fiber. Therefore, the induced evanescent field falls on the plasmonic metal surface leading to the oscillation of free electrons existent there. Thus, the SPW gets excited and circulates along the core-cladding region. At a distinct wavelength, the SPP mode conjoins with the core mode to attain the phase-matching condition between two modes with an equally real part of effective RI. A sharper resonance peak is achieved during this condition at that particular wavelength, and this peak is highly reliant on analyte RI. For this reason, any slight change in RI results in the shifting of resonance wavelength (RW) towards a higher or lower wavelength. Thus, an anonymous analyte can be identified by perceiving the fluctuation of the RW for dissimilar analyte RIs.

The initial stage of the SPR based sensors is prism-based and D- shaped sensors. After many effective researches, PCF sensors were initiated. It has passed a long run due to its evolution process. In recent PCF-SPR sensors, the plasmonic metal layer and the analyte channel through which the substance to be diagnosed is passed are kept either outside or inside the fiber, depending on the type of the sensor. The evolution, variation, and division of PCF sensors based on the SPR technique are described briefly in these next segments.

4.2 Prism based Sensor

In the year 1983, Liedberg *et al.* implemented a prism-coupled SPR biosensor in biosensing fields to detect unknown gases [23]. The exploration of SPR based biosensors started then. In prism-based SPR sensors, the light was transmitted through the prism at a specific angle. Upon light incidence on the metal surface, surface plasmon wave (SPW) originated because of the subsuming of incident light by the metal's active valence electrons. Later, it was perceived that prism-based SPR sensors had some impediments like inaccuracy in sensing application and bulkiness in size due to supplemental complicated opto-mechanical parts, making them unsuited for remote-sensing [67], [68].

4.3 Internal Sensing based Sensor

The internal sensing type sensor was invented to control the obstacles of the prism-based sensors. Internal sensing is the conventional way of sensing where the air holes are coated with metal films, while the analytes are packed within the hole (shown in figure 4.1) [67]–[70]. Practical implementation of the first type is quite complicated as it is difficult to coat the internal fiber holes with metal films and fill them with analytes. These difficulties arise because of the small size of the holes. Besides, maintaining the uniform thickness of the holes is not feasible for fabrication. Another reason is that while measuring, emptying, and refilling the fiber is needed, which is time-consuming. Moreover, frequently filling and emptying can cause a decrease in the sensing characteristics of the sensor.

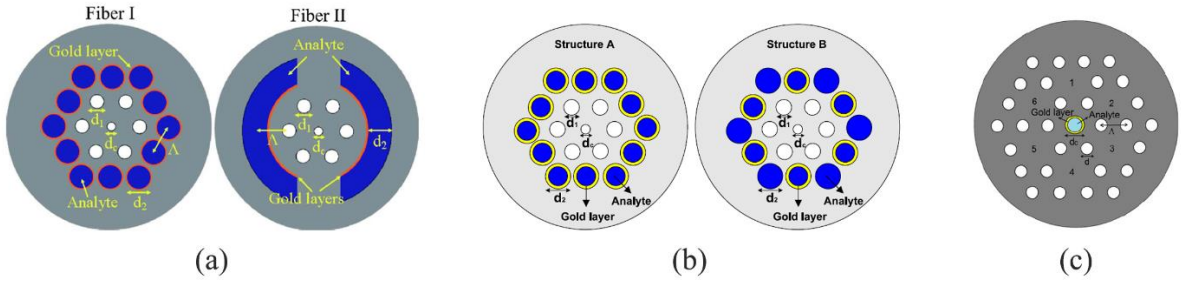

Figure 4.1: Internal Sensing based Sensors

4.4 D-shaped Sensor

The use of D-shaped or exposed-core PCFs can help to overcome the disadvantages of prism-based sensors and internal sensing based sensors [71]–[74]. In the D-shaped PCFs, metal

and analyte are deposited on the exposed area directly (shown in figure 4.2); thus, the sensor fabrication and the analyte changing are simplified. However, the flat portion of the D-shaped PCFs needs polishing, which imposes fabrication difficulty. Still, in practical practice, this type of sensor needs the etching of particular parts of the surface, which also adds complexity for fabrication and makes sensors expensive.

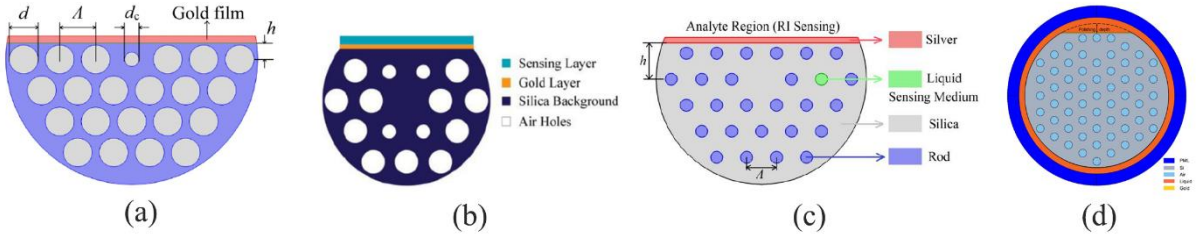

Figure 4.2: D-shaped Sensors

4.5 External Sensing based Sensor

Due to the limitations of internal sensing and D-shaped PCF, external sensing has become the preferred method for analyte detection due to excellent sensing characteristics and the benefit in the fabrication process [75], [76]. It provides the facilities which include cleaning and re-using of a sensor. As the metal coating is positioned outside the fiber (shown in figure 4.3-a), unlike internal sensing, where the metal coating is placed inside the air holes, it does not require any pre-steps before sampling. The sensor simply adheres to the analyte solution, and within few minutes, it exhibits the outcome of the desired sensor performance.

4.6 Plasmonic Material Silver based Sensor

The plasmonic material used in the sensor affects the sensing performance strongly. Silver gives a sharper resonance peak which gives beneficial output in terms of FOM. A silver based sensor is shown in figure 4.3 (b) [77]. Though silver is one of the most conductive materials, it is oxidized easily with time in aqueous circumstances. This phenomenon reduces the sensing accuracy and hampers the sensor performance. Due to this chemical instability of silver (Ag) and other limitations [78], it shows an inaccurate sensing performance.

4.7 Bimetallic Silver-Graphene based Sensor

Silver oxidizes in a hydrous environment, resulting in a decrease in sensing accuracy. An attempt to put a lean coating of graphene has been made to control the oxidization problem, which in practice increases the manufacturing cost along with the fabrication difficulties due to additional layers [79]. A sensor utilizing Silver-Graphene coating is depicted in figure 4.3 (c) [79].

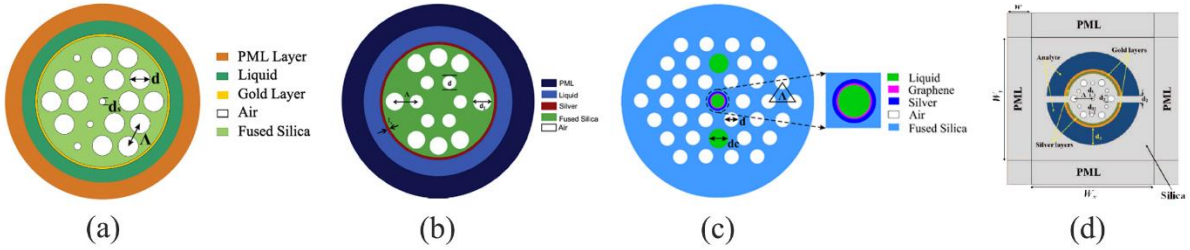

Figure 4.3: (a) External Sensing based sensor, (b) Silver based sensor, (c) Silver-Graphene based sensor, (d) Silver-Gold based sensor

4.8 Bimetallic Silver-Gold based Sensor

This type of SPR-PCF biosensor has two metalized microfluidic slots that are constituted with gold and silver as plasmonic material. This innovative type design was initially proposed by Akowah *et al.* in 2012. Gold is positioned at the top of the silver to prevent oxidation and other chemicals. The structure (shown in figure 4.3-d) has an easier fabrication process due to large micro-fluidic slots [80].

4.9 Bimetallic Silver-TiN based Sensor

Conventional bimetallic designs have Gold-Silver coating where gold is used as a protective layer. But gold has the disadvantage of broader resonance curves that limit the accuracy of detection. So, the newly proposed bimetallic configuration can be based on silver and TiN (shown in figure 4.4-a). The surface of the operating channel is layered with a silver coating. An additional layer of TiN was utilized to protect the silver layer from oxidation and to maintain chemical stability [81].

4.10 Plasmonic Material Gold based Sensor

Though silver has a sharper resonant peak, it exhibits chemically unstable behavior. Thus, recently gold is popularly used due to its chemical stability and the shift of resonant wavelength by a significant amount, which results in proper detection of the analyte [82], [83]. A large number of researches are done on gold-based biosensors. A sensor utilizing Gold as the plasmonic material is displayed in figure 4.4 (b) [83].

4.11 Bimetallic Gold-TiO_2 based Sensor

In this type of sensor, gold is applied as a thin layer to coat the channel. On top of that, the deposition of a TiO_2 film proliferates the surface plasmonic excitation by assisting the adhesion of gold [84]. The rise in the excitation of surface plasmonic increases the evanescent field. It also has high RI than the fiber and provides strong coupling between the leaky core guided and the plasmonic mode whenever placed on the glass creates. Therefore, this layer improves sensing performance. A sensor having Gold-TiO_2 coating is displayed in figure 4.4 (c) [85].

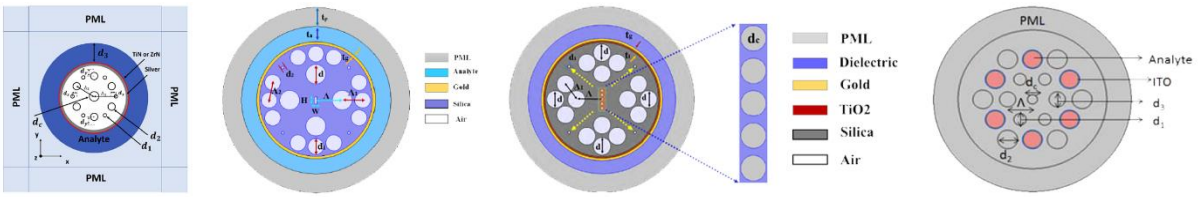

Figure 4.4: (a) Silver-TiN based sensor, (b) Gold based sensor, (c) Gold-TiO_2 based sensor, (d) ITO based sensor

4.12 ITO based Sensor

Using Indium Tin Oxide (ITO), the adjustment of the plasmonic resonance can be performed by varying the inherent characteristics of the materials [38]. Basically, by altering the number of oxygen content and metal atoms, the plasmonic behavior can be controlled. Additionally, ITO is more cost-effective than gold and silver. A sensor utilizing ITO as the plasmonic material is displayed in figure 4.4 (d) [38].

Chapter 5

Material Characterization and Mathematical Formulation

5.1 Introduction

In this chapter, we have discussed the different materials that are used in designing the SPR-based PCF sensors. Silica (SiO_2), Titanium dioxide (TiO_2), Gold (Au), Aluminium doped Zinc Oxide (AZO), etc., are the materials that are commonly used. Here we have demonstrated the equations that can be used to characterize these materials in simulation platforms. It is to be mentioned that only the refractive index (RI) of these materials is of interest. So we have shown only the RI equations of these materials. In some cases, we have provided the permittivity equations since the square-root of permittivity gives the RI. Then we also discussed in this chapter the parameters that help to determine the sensor performance. These parameters include confinement loss (CL), amplitude sensitivity (AS), wavelength sensitivity (WS), temperature sensitivity, strain sensitivity, resolution, birefringence, figure of merit (FOM), sensor length, etc. The formulas that can be used to calculate these parameters are displayed and explained in this chapter.

5.2 Characterization of Materials

In this section, the materials characterization equations are discussed. Here we have focused only on the materials we have used in our research works discussed in chapters 6, 7, 8, and 9. Note that some materials have a complex effective RI. The effective RI of any material can be represented in the complex form of $n_{eff} = n + jk$, where n and k denote the RI's real and complex parts.

5.2.1 Silica (SiO_2)

SPR-based sensors are usually fabricated by putting a lamination of plasmonic metal on the surface of a PCF. The PCF can be made of either some glasses or some polymers. Fused Silica, also known as silicon di-oxide, is vastly preferred as the

background material of the PCF. Generally, an undoped version of silica is used. Due to the following advantageous behaviors, silica is given preference over other glasses and polymers [86]:

- ✓ One of the essential advantages of silica is its chemical stability. It does not show any hygroscopic behavior.
- ✓ Silica exhibits good optical transparency in a wide wavelength range.
- ✓ The mechanical strength of silica is remarkable against pulling and bending.
- ✓ Silica has deficient scattering and absorption loss (around 0.2 dB/km) in the near-IR spectral region. This characteristic can be realized from figure 5.1.
- ✓ At high temperatures, silica can be drawn into fibers.
- ✓ Another advantage of silica is that the fusion splicing of silica performs excellently.
- ✓ The high damage threshold is another advantageous property of silica. Due to this property, silica shows a low tendency of laser-induced breakdown. During the amplification of short pulses in fiber amplifiers, this property plays a vital role.

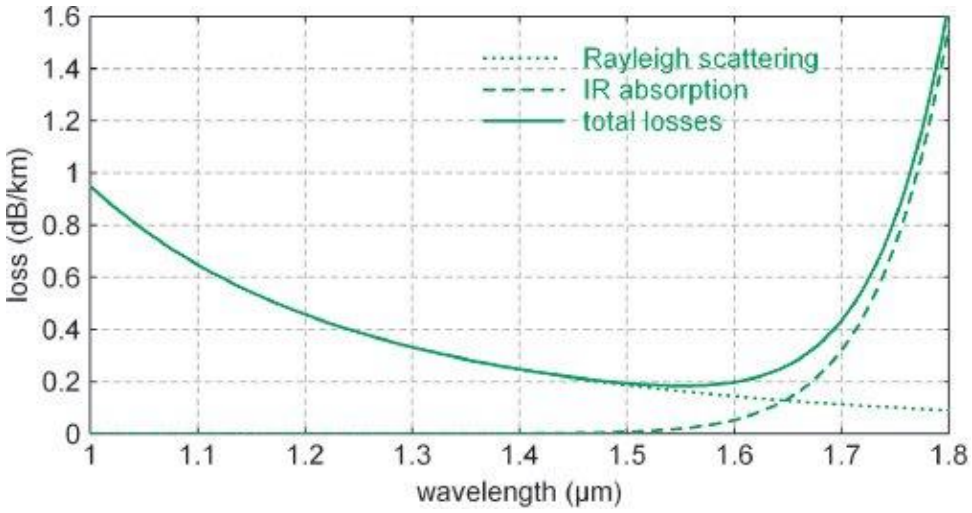

Figure 5.1: Intrinsic losses of silica

The RI property of the fused silica is extracted from the Sellmeier equation given below [9]:

$$n_{silica}(\lambda) = \sqrt{1 + \frac{B_1\lambda^2}{\lambda^2 - C_1} + \frac{B_2\lambda^2}{\lambda^2 - C_2} + \frac{B_3\lambda^2}{\lambda^2 - C_3}} \tag{5.1}$$

Here, n_{silica} represents the RI of silica, and the value of n_{silica} depends on the wavelength of light (λ) and the Sellmeier constants. The Sellmeier constants are listed in table 5.1. It is to

be mentioned that equation 5.1 is valid for the wavelength range of 0.22 µm to 3.71 µm [85]. This formula can be used to estimate the silica RI at a constant temperature of 25 ◦C [87]. Figure 5.2 depicts the RI of silica as a function of wavelength. It is visible from figure 5.2 that the complex part of the silica refractive index is always zero. Therefore, the refractive index of silica is always a real number.

Table 5.1 Sellmeier Constants

Constant	Value
B_1	0.69616300
B_2	0.407942600
B_3	0.897479400
C_1	0.00467914826 µm^2
C_2	0.0135120631 µm^2
C_3	97.9340025 µm^2

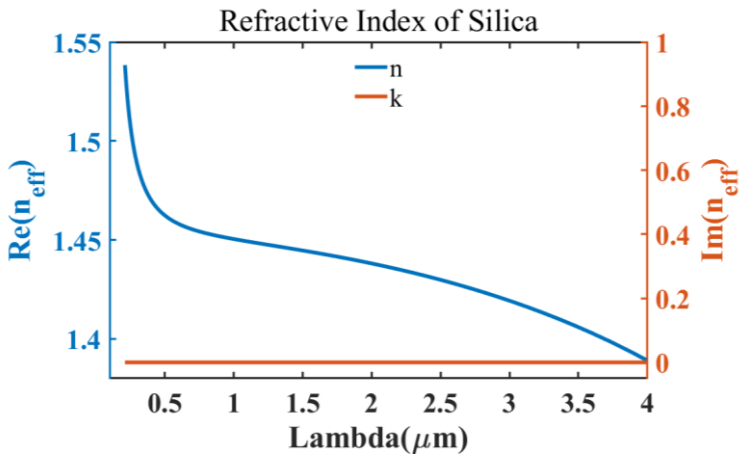

Figure 5.2: Silica RI as a function of light wavelength (temperature 25 ◦C)

When T denotes the temperature in Celsius (◦C) scale, the temperature-dependent Silica RI n_{silica} can also be estimated using the modified Sellmeier equation given below [25]:

$$n^2_{silica}(\lambda,T) = (1.31552 + 6.90754\times10^{-6}T) + \frac{(0.788404 + 23.5835\times10^{-6}T)\lambda^2}{\lambda^2 - (0.0110199 + 0.584758\times10^{-6}T)} + \frac{(0.91316 + 0.548368\times10^{-6}T)\lambda^2}{\lambda^2 - 100} \quad (5.2)$$

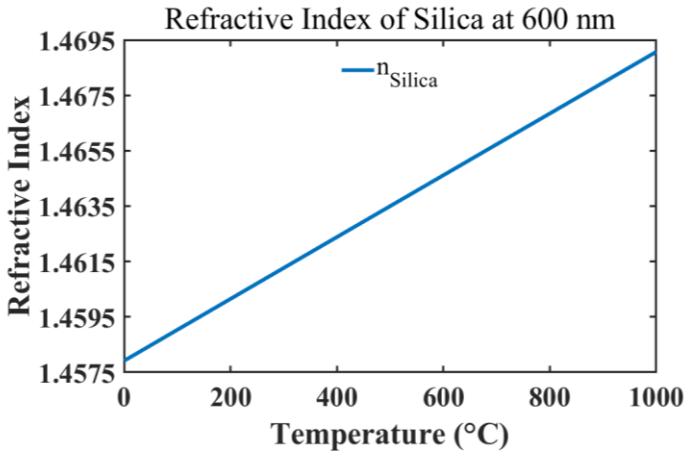

Figure 5.3: Silica RI as a function of temperature (light wavelength 600 nm)

At a constant light wavelength of 600 nm, the silica RI vs. temperature is maifested in figure 5.3. It is realizable from figure 5.3 that the silica RI increases as the temperature is raised.

The above two equations evaluate the silica RI when the applied strain is null. However, when the fiber undergoes any amount of strain, the RI of silica changes owing to the Opto-elastic property. The strain-dependent refractive index of Silica for variable applied stresses can be estimated by the following formula [26], [88]:

$$n'_{silica} = n_{silica}[1 - P_e \varepsilon_z] \tag{5.3}$$

where n_{silica} and n'_{silica} are the silica RI without strain and with strain, ε_z denotes the applied strain, and P_e is the elastic-optic constant. It is to be mentioned that P_e has a magnitude of 0.22 for silica [88]. For varying strain in the range of 0-2000 με, the silica RI is exhibited in figure 5.4. It is realizable that silica RI reduces with the increase of strain.

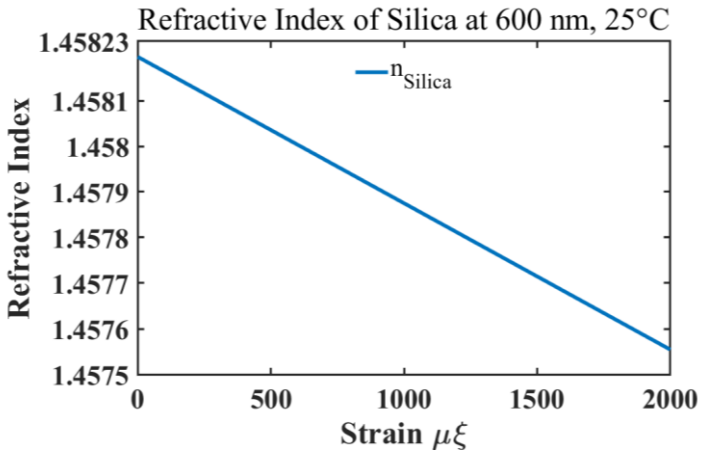

Figure 5.4: Silica RI as a function of strain (light wavelength 600 nm, temperature 25 ◦C)

5.2.2 *Air*

Air is used to fill up the cavities existing in the PCF. The refractive index of air gets altered as the light wavelength is varied. However, this change is very insignificant, which can be realized from figure 5.5.

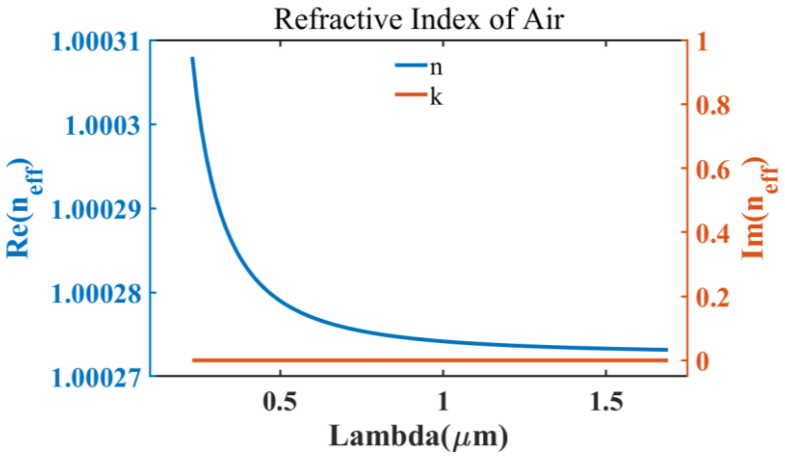

Figure 5.5: Air RI as a function of light wavelength

Figure 5.5 displays the relationship between the air RI and the light wavelength. It is realizable that air RI is always a real value and has a magnitude very close to 1. Therefore, we have considered air RI to be 1 in all our research works.

5.2.3 *Gold*

Gold is a material that has an atomic number of 79. It is symbolized by 'Au' and has a relative atomic mass of 196.96657. The melting point of gold is 1064 °C. We have used gold to laminate the exterior of our SPR sensors. It is vastly used as the plasmonic material due to its advantageous behavior over other plasmonic materials. The advantages that gold provides are [40]:

- ✓ Gold is chemically stable and inert.
- ✓ Gold does not get oxidized in an aqueous environment
- ✓ A sharp resonant peak and a broad resonance peak shift even in an aqueous environment

The dielectric constant of gold can be estimated from the Drude-Lorentz model, and it can be described as below [89]:

$$\varepsilon_{Au} = \varepsilon_{\infty} - \frac{\omega_D^2}{\omega(\omega + j\gamma_D)} - \frac{\Delta\varepsilon.\Omega_L^2}{(\omega^2 - \Omega_L^2) + j\Gamma_L\omega} \tag{5.4}$$

In this equation, ε_{Au} represents the permittivity of gold, ε_∞ represents the high-frequency permittivity with a value of 5.9673. ω is the angular frequency, ω_D and γ_D are plasma and damping frequencies respectively, where $\omega_D = 4227.2\pi$ THz, $\gamma_D = 31.84\pi$ THz. Moreover, $\Delta\varepsilon = 1.09$ is the weighting factor while the oscillator strength is $\Omega_L = 1300.14\pi$ THz, and spectral width is $\Gamma_L = 209.72\pi$ THz.

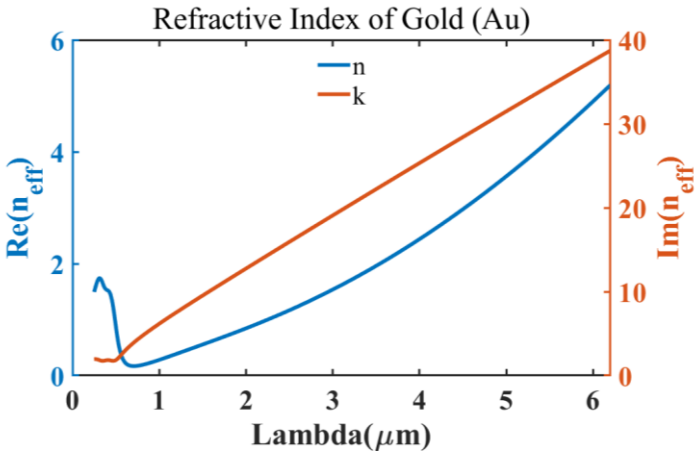

Figure 5.6: Gold RI as a function of light wavelength

It is clear from equation 5.4 that the dielectric constant of gold is a complex number, and it is equal to the squared value of gold RI. So the gold RI can be obtained by square-rooting the dielectric constant, which is another complex value. The real and complex parts of gold RI vs. wavelength curves are plotted in figure 5.6.

5.2.4 Titanium di-oxide (TiO_2)

Inserting a thin layer of titanium di-oxide between the gold and fiber has recently become a widespread practice. TiO_2 film is deposited with a view to increasing the adhesion of gold with the fiber since the gold layer easily flakes off upon the application of gentle pressure [32]. TiO_2 has a high RI and plays the role of a transition metal [90]. Therefore, it helps in alluring the evanescent fields from the core. Moreover, the TiO_2 layer produces a high number of electrons at the surface, and these additional electrons attract the evanescent field from the core to interact actively with the plasmonic material and, therefore, enhances the sensitivity of the SPR-based sensors [85].

The TiO_2 RI vs. wavelength curve is plotted in figure 5.7. When λ and n_t are the wavelength (in Angstroms) and the RI of TiO_2, respectively, the refractive index characteristics of metallic layer TiO_2 can be obtained from the following equation [91]:

$$n_t = \sqrt{5.913 + \frac{2.441\times10^7}{\lambda^2 - 0.803\times10^7}} \tag{5.5}$$

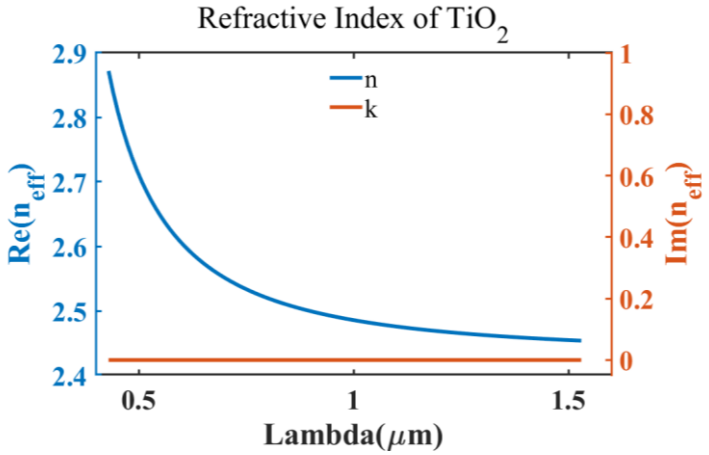

Figure 5.7: TiO_2 RI as a function of light wavelength

5.2.5 Aluminium doped Zinc Oxide (AZO)

Aluminium doped Zinc Oxide (2% wt of Al in ZnO), also known as AZO, is another plasmonic material used as an alternative to gold. Even though aluminium gets affected by oxidation in the hydrous area, it shows promising results. As plasmonic material, AZO has a few advantages over gold. It is noteworthy that a thin gold layer effectuates the formation of island [20]. Moreover, gold has a high plasma frequency, and therefore gold-based sensors operate in the UV or visible region [20]. On the other hand, due to low charge carrier density, AZO has plasma frequency in the near IR region [20]. The evanescent field in the near IR region has high penetration depth, and hence AZO based SPR sensors have a substantial importance in the biomedical sensing applications [20]. Additionally, AZO's charge carrier density can be modified by altering the doping concentration, which gives control over the plasma frequency [20].

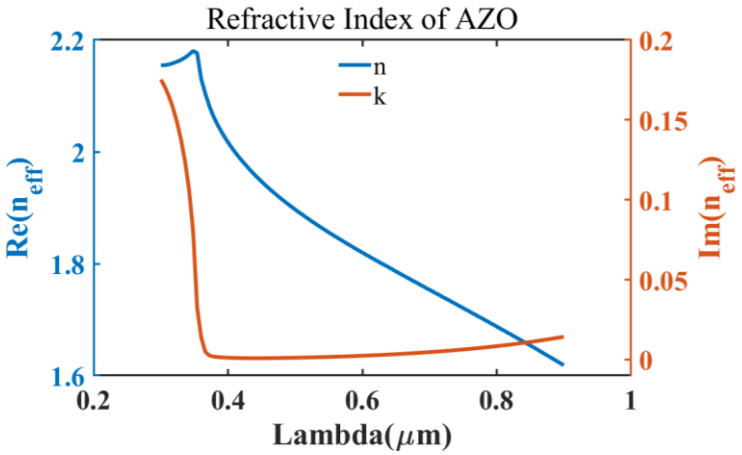

Figure 5.8: AZO RI as a function of light wavelength

The dielectric characteristics of AZO (2% wt) can be expressed as [20], [92]:

$$\varepsilon_{AZO}(\omega) = \varepsilon_b - \frac{\omega_p^{\,2}}{\omega(\omega + j\gamma_p)} + \frac{f_1\omega_1^{\,2}}{(\omega_1^{\,2} - \omega^2 - j\omega\gamma_1)} \tag{5.6}$$

where ε_b is the polarization response of core electrons (background permittivity) and has a value of 3.5402 and ω_p is the plasma frequency having a magnitude of 1.7473 eV. The other parameters, γ_p, f_1, ω_1, and γ_1, have the corresponding values of 0.04486 eV, 0.5095, 4.2942 eV, and 0.1017 eV. Figure 5.8 shows the real and complex parts of the effective RI of AZO as a function of light wavelength.

5.2.6 Ethanol (C_2H_5OH)

Ethanol is a hydrocarbon compound. The symbol of ethanol is C_2H_5OH. The functional group of ethanol is the hydroxyl (-OH) group. Therefore, it is generalized in the group of alcohol. The melting point of ethanol is -114.1 ◦C, whereas the boiling point is 78.37 ◦C. Ethanol is used in many applications such as:

- ✓ perfumes and varnishes manufacturing
- ✓ preserving biological specimens
- ✓ preparing flavorings and essences
- ✓ medicines and drugs
- ✓ in tinctures
- ✓ as a disinfectant
- ✓ as a gasoline and fuel additive

However, ethanol is of our interest due to its temperature-sensitive nature. The refractive index of ethanol is a real number, which is a function of temperature. Ethanol can be used to measure temperature because of its temperature-sensitive property. When ethanol is used as the analyte of an SPR-based PCF sensor, the sensor can be utilized as a temperature sensor. Therefore, we need to know the temperature-dependent RI of ethanol, which can be expressed as [25]:

$$n_1 = n_0 + \frac{dn}{dT}(T_1 - T_0) \tag{5.7}$$

where n_1 and n_0 are the RI at temperatures T_1 and T_0, respectively. At $T_0 = 20^{\circ}C$, the RI of ethanol is $n_0 = 1.361$. Here dn/dT denotes the thermo-optical co-efficient and has a value of $-3.117\times10^{-4}\ ^{\circ}C^{-1}$ [93]. The RI of ethanol as a function of temperature is displayed in figure 5.9. It is evident from figure 5.9 that the RI of ethanol decreases as the temperature is increased.

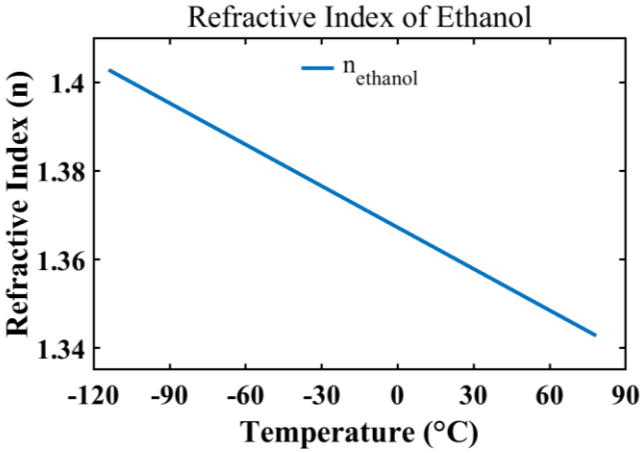

Figure 5.9: Ethanol RI as a function of temperature

5.3 Performance Parameters

In this section, different performance parameters have been discussed that are used to estimate the sensor performance. These parameters include confinement loss (CL), amplitude sensitivity (AS), wavelength sensitivity (WS), resolution, birefringence, figure of merit (FOM), and so on.

5.3.1 Confinement Loss (CL)

Among all performance parameters, confinement loss (CL) is the most critical parameter for measuring sensor performance since it is required to measure all other parameters. The CL indicates the energy that is redirected to SPP mode from core mode. Confinement losses are the losses arising from the modes' leaky nature and the PCF fiber's non-perfect structure. When light is dispatched through the core of the PCF sensor, a portion of the light energy leaks from the core and reaches the metal layer region. The amount of this leaked energy is termed as the 'confinement loss' (CL). The CL can be quantified by the following equation [85], [94]:

$$\alpha = 8.686 \times k_0 \times \mathrm{Im}(n_{eff}) \times 10^4 (dB/cm) \tag{5.8}$$

In the preceding equation, λ symbolizes the wavelength, and Im (n_{eff}) stands for the imaginary part of the effective RI n_{eff}. Furthermore, k_0 represents the wavenumber and can be verbalized as $k_0 = 2\pi/\lambda$. The maximum CL occurs at the resonance condition, at which the transmitted light frequency and the frequency of the plasmonic material electrons are even. The resonance engendering wavelength is acknowledged as the 'resonance wavelength.' At resonance wavelength, the effective RI's real portion of the core mode and the SPP mode becomes equal, and this state is also termed as the phase-matching condition.

5.3.2 Amplitude Sensitivity (AS)

The sensor potential can be measured using two methods, known as the amplitude interrogation method (AI) and the wavelength interrogation (WI) method. The variance of loss depth due to analyte RI change can be utilized to detect different unknown analytes. This method of identifying unknown analytes is known as the amplitude interrogation (intensity-based measurement) method.

When $\alpha(\lambda, n_a)$ is the confinement loss at a particular RI of the analyte and $\partial\alpha(\lambda, n_a)$ is the confinement loss difference due to two adjacent analyte RIs the amplitude sensitivity (AS) of a sensor can be determined by using the formula [85], [95]:

$$S_A = -\frac{1}{\alpha(\lambda, n_a)} \frac{\partial \alpha(\lambda, n_a)}{\partial n_a} (RIU^{-1}) \tag{5.9}$$

The AI method measures AS at a constant wavelength, and thus this method is straightforward in terms of practical implementation. It is because it does not require spectral manipulation [96]. That is why this is the most popular method to determine the

sensitivity of a sensor. However, this method has a trade-off of being very prone to external noise. A significant amount of external noise may hamper the sensor performance and result in erroneous detection of the analyte. Therefore, additional arrangements are needed to block the external noise, making the implementation of this method expensive.

5.3.3 Wavelength Sensitivity (WS)

Another technique to measure the sensor's performance is the wavelength interrogation (spectral-based measurement) method, where the shift of resonance wavelength is taken into account. The following formula is applied to calculate the sensitivity of a sensor in the WI method [85]:

$$S_{\lambda} = \Delta\lambda_{peak} / \Delta n_a (nm / RIU) \tag{5.10}$$

where Δn_a and $\Delta\lambda_{peak}$ represent the difference between two neighboring analytes RI and the contrast in their corresponding resonant wavelengths. Usually, this method exhibits high sensitivity response compared to the AI method [76]. The phase-detection method (WI method) has the advantage of being cost-effective. However, it comes with a tradeoff, which is the complexity of measuring sensitivity [97].

5.3.4 Resolution

Resolution is a parameter that assists in realizing the detection capability of the sensor. The resolution gives an idea about the degree of the slightest modification in RI that can be identified. Assuming the minimum spectral resolution to be $\partial\lambda_{min}$, and $\partial\lambda_{peak}$ being the RW shift, the following formula enumerates the resolution [84], [85]:

$$R = \frac{\partial n_a \times \partial\lambda_{\min}}{\partial\lambda_{peak}} (RIU) \tag{5.11}$$

5.3.5 Birefringence

The distinction between the real parts of the effective RI of x- and y- polarization modes, represented by n_x and n_y, is termed birefringence. Birefringence is a vital characteristic of a sensor, and it can be determined using the following formula [61], [98]:

$$B = \left| n_x - n_y \right| \tag{5.12}$$

The birefringence of a sensor should be as high as possible as it helps to maintain the polarization state of the input signal [85]. Moreover, it creates a difference in sensitivity between x- and y-polarized signals. Sustainment of the input signal's polarization state leads to the expulsion of the polarization mode dispersion (PMD) and the stability enhancement of optical device operation, which are beneficial for sensing applications [61].

5.3.6 Full Width at Half Maximum (FWHM)

FWHM is the width of the confinement loss curve at the half value of the peak loss. It determines the sharpness of the loss peak. The sharper the loss peak, the better the sensing performance of a sensor. Moreover, FWHM is needed to evaluate the FOM of the sensor. Therefore, FWHM is an important parameter to determine sensor performance. Figure 5.10 gives an idea about how to determine the FWHM. Usually, FWHM is measured on a nanometer scale.

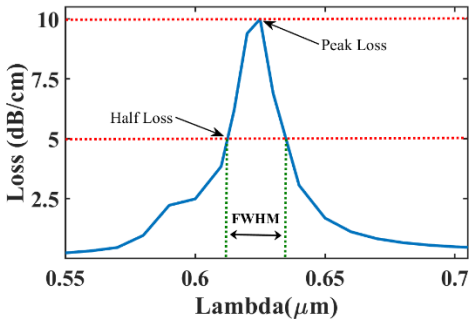

Figure 5.10: Representation of Full Width at Half Maximum

5.3.7 Figure of Merit (FOM)

Besides AS and WS, the sensor efficiency can also be indicated through another parameter known as the figure of merit (FOM). It is simply the ratio of the WS and the FWHM. When S_λ is the WS, and the FWHM indicates the full width at half-maximum, the FOM can be measured by the following equation [83]:

$$FOM = \frac{S_\lambda (nm / RIU)}{FWHM\,(nm)} \tag{5.13}$$

The FOM of a highly performable sensor should be of high value, obtained when the sensor's sensitivity increases with the decrease of FWHM [85]. The increased value of WS indicates a higher shift of resonance wavelength. On the other hand, reduced FWHM

indicates a sharper resonance peak. Therefore, FOM gives an idea about the overall sensor performance.

5.3.8 Sensor Length

When $\alpha(\lambda, n_a)$ is the peak confinement loss of a specific analyte RI n_a, the length of the sensor for that RI can be defined by [83]:

$$L = [\alpha(\lambda, n_a)]^{-1}(cm) \tag{5.14}$$

5.3.9 Temperature Sensitivity

The sensitivity of a sensor in terms of temperature can be computed by the given formula [88]:

$$S_T = \frac{\partial \lambda_{peak}(T)}{\partial T}(nm/^{\circ}C) \tag{5.15}$$

where ∂T is the change of temperature in degree Celsius and $\partial\lambda_{peak}$ represent the shift of resonance wavelength due to the temperature change.

5.3.10 Resolution (Temperature)

The resolution (temperature) of a sensor is defined by the following equation [25]:

$$R_T = \partial T \times \frac{\partial \lambda_{\min}}{\partial \lambda_{peak}}(^{\circ}C) \tag{5.16}$$

Here, $\partial\lambda_{min}$ is the spectral resolution (minimum), whereas ∂T and $\partial\lambda_{peak}$ represent the difference between two different temperatures and the contrast in their corresponding resonant wavelengths. This resolution indicates the infinitesimal alteration of temperature that the sensor is capable of identifying.

5.3.11 Strain Sensitivity

A sensor's strain sensitivity can be estimated by the given formula [88]:

$$S_{\varepsilon_z} = \frac{\partial \lambda_{peak}(\varepsilon_z)}{\partial \varepsilon_z}(nm/\mu\varepsilon) \tag{5.17}$$

where $\partial\varepsilon_z$ and $\partial\lambda_{peak}$ represent the difference between two different strain values and the contrast in their corresponding resonant wavelengths.

5.4 Conclusion

By now, we have become familiar with all the materials required to construct an SPR based PCF sensor. We have also become familiar with the parameters that are needed to estimate the sensor performance. These materials' characterization equations and performance parameters are used in the following chapters, where we have discussed our proposed sensor structure and their performance.

Chapter 6

Proposed Design-1: Highly Sensitive and Birefringent Biosensor with Low Loss

6.1 Introduction

This chapter has discussed a novel, perfectly hexagonal lattice PCF biosensor based on SPR. To design and investigate the influence of several initial geometric parameters on the sensor's sensing properties, the FEM based commercially available COMSOL Multiphysics version 5.3a is used. A 20 nm layer of chemically stable plasmonic material gold (Au) is used to make the excitation possible between the core and plasmonic modes. A thin film of TiO_2 is placed on the glass surface, which allures the field from the core guided mode and assists in the fiber's adhesion of gold (Au). By exploiting the geometric parameters, simulation results show a maximum WS of 16000 nm/RIU and 17000 nm/RIU for x-polarization and y-polarization, respectively, due to the dielectric refractive index (RI) variation from 1.33 to 1.41. It is shown that the highest obtained AS of the proposed sensor reaches 4596 RIU^{-1} and 4557 RIU^{-1}, respectively, for x-polarization and y-polarization with the maximum CL of 3.73 dB/cm and 4.48 dB/cm. Additionally, the maximum sensor resolution (amplitude) of 2.18×10^{-6} and 2.19×10^{-6}, the maximum sensor resolution (wavelength) of 6.25×10^{-6} and 5.88×10^{-6} for x- and y-polarization modes, respectively and maximum birefringence of 8.8984×10^{-4} is attained. The sensing range of our proposed sensor is determined to be 1.33-1.41, which includes various chemical solutions and biochemical agents, for instance, blood plasma (1.35), RBC (1.40), WBC (1.36), hemoglobin (1.38), intestinal mucosa of human (1.329-1.338), 10% glucose solution (1.3477), acetone (1.36), human liver (1.369), and so on [85], [99]. So it is needless to mention that our proposed sensor will play a vital role in the chemical and medical industry by properly detecting these essential biochemicals.

6.2 Structural Design and Theoretical Modelling

Figure 6.1 (a) depicts the 2D cross-sectional view of our introduced design, having several clusters of circular-shaped air holes in the cladding region and a single rectangular air hole in the core. The cladding region consists of six such clusters of air holes arranged in a hexagonal manner. The clusters are 60 degrees apart and have a radius of 1.5×p from the center of the core, where p is equal to 1.55 μm. Each cluster consists of five small circular-shaped air holes, each having a diameter of d. The air holes are placed 72 degrees apart from each other. Moreover, the center of any air hole has a distance of 'a' from the cluster's center. A rectangular air hole that has a height (h) of 0.4 μm and a width (w) of 0.22 μm is placed at the exact center of the fiber, which helps to create an asymmetry in the formation and guide the waves towards the surface, thus improving the sensing capabilities [100]. Also, this air hole provides the core power with the opportunity to couple with the surface that creates a birefringence effect on the sensor. Due to the smaller air holes with diameter d, light confined in the core mode interacts with the plasmonic mode and links the core and plasmonic mode.

Fused silica is chosen as the background material of this sensor, which can be characterized by equation 5.1. A perfectly matched layer (PML) expressed as t_{PML} is the outermost layer of the biosensor, which can absorb the radiated energy. Just beneath that, there is an analyte layer whose thickness is depicted as t_a has a remarkable impact on sensing performances, and during simulation, we have assumed it to have a constant thickness of 1.5 μm. The thickness of a thin layer of gold (Au) is denoted as t_g, and this layer is used to reduce the loss of light propagation through the sensor. On top of that, the deposition of a TiO_2 film proliferates the surface plasmonic excitation by assisting the adhesion of Au. After multiple observations by varying the parameters, we found optimum values of t_{PML} = 1.50 μm, t_g = 20 nm, t_t =10 nm, t_a = 1.50 μm, r_c = 2.2×p, h = 0.4 μm, w = 0.22 μm, p = 1.55 μm, p_1 =1.5×p, a = 0.65 μm and d = 0.45×p. The optimization of these parameters is elaborately discussed later in this chapter.

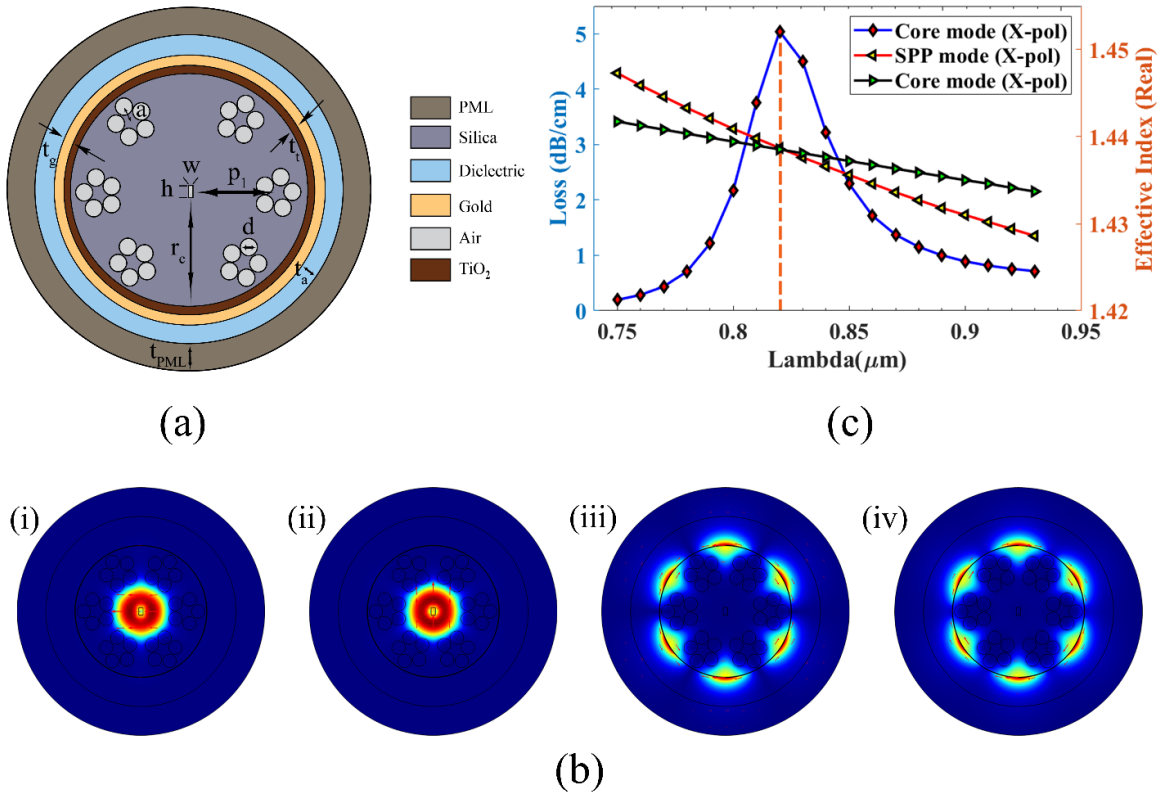

Figure 6.1: (a) Cross-sectional view of the proposed PCF sensor; (b) Optical field distribution of i. x-polarized core mode, ii. y-polarized core mode, iii. x-polarized SPP mode, iv. y-polarized SPP mode; (c) Dispersion relation between SPP mode and core-guided mode at analyte RI = 1.40

6.3 Sensor Performance Investigation and Optimization of Different Geometrical Parameters

6.3.1 Guiding Properties and Dispersion Characteristics

The optical field distribution of the proposed sensor for core mode and SPP mode is shown in figure 6.1 (b). The insets (i) and (ii) of figure 6.1 (b) show the field distribution of the core-guided mode at analyte RI 1.40 for x- and y-pol, respectively. Field distribution of the SPP mode at analyte RI 1.40 for x- and y-polarization modes are shown in the insets (iii) and (iv) of figure 6.1 (b), respectively. Figure 6.1 (b) portrays strong coupling for both the polarization modes. Thus, both polarizations are taken into account while investigating the sensing performance since the proposed sensor experiences birefringence due to its structure's asymmetry. The presence of the rectangular air hole at the center of the fiber causes this asymmetry.

Resonance occurs if the evanescent field frequency harmonizes with the frequency of the electrons of the plasmonic material. The effective index of core-guided mode and SPP mode becomes the same at this matching frequency, and a notable confinement loss peak occurs. This event is known as the phase-matching phenomena, where maximum energy is transferred from core-guided mode to SPP mode [76]. The confinement loss (CL) can be calculated using equation 5.8. The dispersion relation of the proposed sensor at analyte RI 1.40 is illustrated in figure 6.1 (c). It is visible from figure 6.1 (c) that phase matching phenomena occur at the wavelength of 0.82 µm, which is also termed as resonance wavelength. This resonance wavelength changes with the small variation of analyte RI. Due to the increase in analyte RI, the resonance wavelength shifts to the right, whereas it shifts to the left when the analyte RI is decreased. These shifts are often cited as red-shift and blue- shift, respectively [76]. The shift of resonance wavelength due to analyte RI variation from 1.33 to 1.41 for x- and y-polarization modes is manifested in figure 6.2 (a) and (b), respectively.

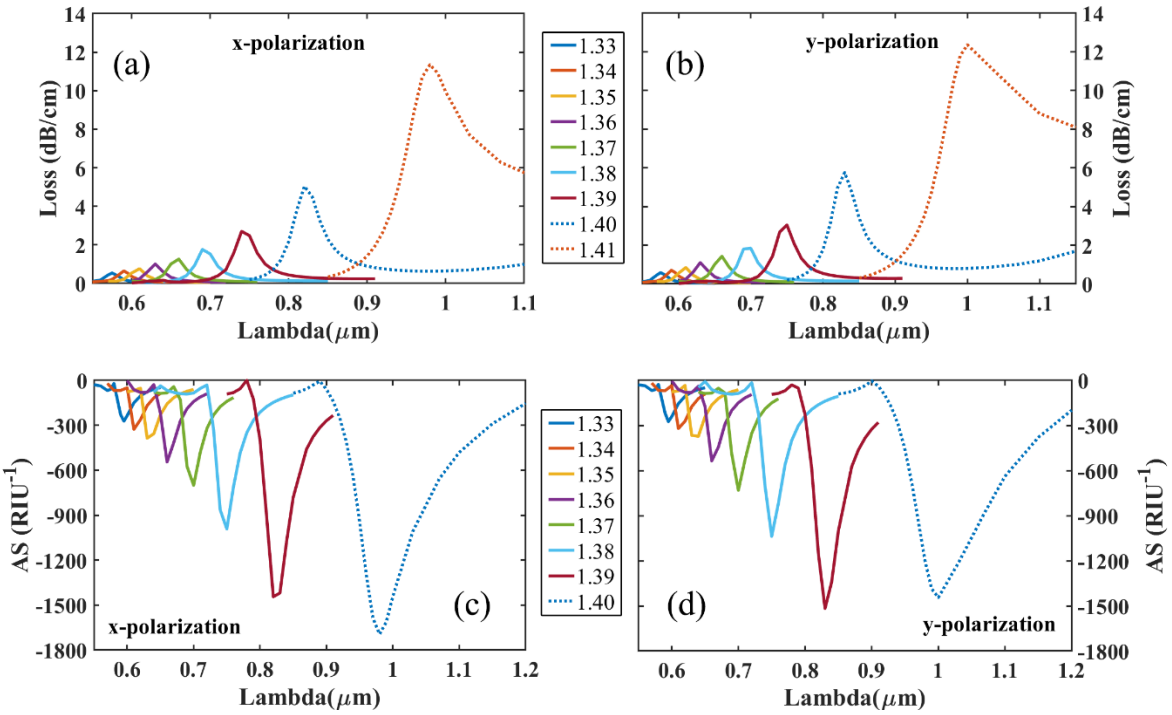

Figure 6.2: Loss spectrum for analyte RI from 1.33 to 1.41 for (a) x-pol, (b) y-pol; and Amplitude sensitivity for analyte RI from 1.33 to 1.40 for (c) x-pol, (d) y-pol

It can be noticed in figure 6.2 (a) and (b) that the loss depth rises as the analyte RI is increased. The lowest CL is 0.538 dB/cm, and the highest CL is 11.35 dB/cm at analyte RI of 1.33 and 1.41, respectively, for x-polarization mode. For y-pol, the lowest CL is 0.583

dB/cm, and the highest CL is 12.36 dB/cm at analyte RI of 1.33 and 1.41, respectively. In this work, we limit our investigation up to analyte RI of 1.41 as analyte RIs' higher than 1.41 show very high loss, and, sometimes, the loss peak cannot be detected accurately. It is to be mentioned that throughout this book, the term 'sensitivity' refers to 'surface sensitivity' as we intend our sensors to be a biosensor [101].

Figure 6.2 (c) and (d) depict the stated sensor's amplitude sensitivity at analyte RIs from 1.33 to 1.40 for x- and y-polarization modes, respectively. The maximum AS (1694 RIU^{-1}) for x-pol is obtained at analyte RI 1.40. Maximum WS of 16000 nm/RIU is also obtained at this analyte RI for x-pol. So the optimum RI is taken as 1.40 for x-pol. For y-polarization mode, the maximum AS (1517 RIU^{-1}) is found at analyte RI 1.39, and the maximum WS (17000 nm/RIU) is obtained at analyte RI 1.40. The AS of RI 1.39 (1517 RIU^{-1}) is slightly higher than that of 1.40 (1444 RIU^{-1}), but the WS for 1.39 (8000 nm/RIU) is much lower than the WS of 1.40 (17000 nm/RIU). So, considering the WS, we choose RI 1.40 as the optimum for y-pol. Here, the AS and the WS are calculated using equations 5.9 and 5.10, respectively.

The maximum resolution of the proposed sensor is calculated using equation 5.11, and the values are found to be 6.25×10^{-6} and 5.88×10^{-6} for x- and y-pol, respectively, at analyte RI 1.40. It is mention-worthy that the influences of external noise have not been considered while calculating the resolution. Hence, the resolution stated in this book is the maximum expected resolution in the absence of external noise and, according to ref. [101], this resolution can be termed as 'maximum theoretical resolution.' Moreover, in practical applications, the sensor's resolution may differ from the stated value depending on the signal to noise ratio.

The proposed sensor showed a maximum birefringence of 8.8984×10^{-4} at analyte RI 1.40, calculated by equation 5.12. Figure 6.3 (a) exhibits the proposed sensor's birefringence as a function of wavelength at analyte RI 1.40. It is to be mentioned that the high birefringence of a sensor introduces the necessity of extreme caution while placing the sensor for practical applications to avoid curvatures or twist in it. It is because any amount of twist changes the sensitivity of the sensors that are polarization-dependent [102].

The regression line of an excellent sensor should have a high linearity response. Figure 6.3 (b) shows the linear fitting and quadratic polynomial fitting of the resonant wavelengths as a function of analyte RI from 1.33 to 1.41. It is visible from figure 6.3 (b) that the proposed sensor shows the fitting response $R^2 = 0.8427$ and $R^2 = 0.9908$ at linear fit and second-order polynomial fit, respectively, which indicates better linearity.

The performance of a sensor severely depends on various geometrical parameters such as gold layer thickness, TiO_2 layer thickness, analyte layer thickness, air hole diameter, etc. These parameters must be optimized to obtain the maximum sensitivity of the sensor. While optimizing one parameter, other parameters must be kept constant. The initial values of different geometrical parameters of the proposed sensor was set as TiO_2 layer thickness (t_t) = 5 nm, gold layer thickness (t_g) = 30 nm, analyte layer thickness (t_a) = 1.50 µm, PML layer thickness (t_{PML}) = 1.50 µm, height of rectangular air hole (h) = 0.4 µm, width of rectangular air hole (w) = 0.18 µm, p = 1.65 µm, air hole distance from the center of any cluster (a) = 0.65 µm, air hole diameter (d) = 0.40×p, distance of each cluster from the center of the fiber (p_1) = 1.50×p, and fiber radius (r_c) = 2.20×p. Then these parameters were optimized, starting with the gold layer thickness. Though the optimization of different geometrical parameters was done for both x- and y-pol, the results and curves of only x-pol have been shown in this literature while discussing the optimization process.

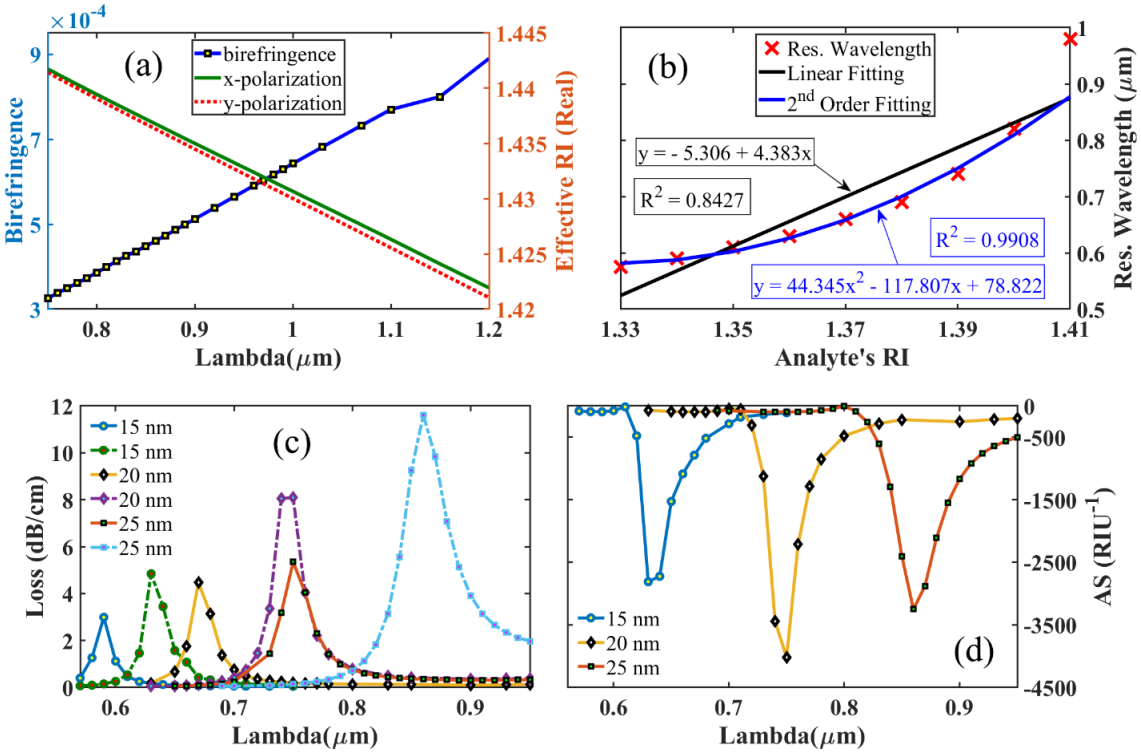

Figure 6.3: (a) Birefringence and effective RI as a function of wavelength at analyte RI of 1.40; (b) Regression lines of the resonance wavelength as a function of analyte RI; (c) Loss spectra for t_g = 15 nm, 20 nm, and 25 nm at analyte RI of 1.40 (solid lines) and 1.41 (dashed lines); and (d) Amplitude Sensitivity for t_g = 15 nm, 20 nm, and 25 nm at analyte RI of 1.40

6.3.2 Optimization of Gold Layer Thickness.

The gold layer generates the SPW. Thus the thickness of this layer has a considerable impact on the performance of the sensor [103]. Moreover, the gold layer thickness influences the resonance wavelength. Figure 6.3 (c) displays the shift of resonance wavelength due to the change in gold layer thickness. A red-shift in the loss peak can be noticed when the thickness is increased. The loss peak also increases with an increase in thickness due to the high damping loss of gold. A thicker gold layer generates more surface electrons, which helps in increasing the sensitivity. However, a very thick layer of gold (e.g., 25 nm) obstructs the EM waves from interacting with the analyte layer, reducing the sensitivity. The maximum AS (4021 RIU^{-1}) is obtained for the thickness of 20 nm, which can be seen in figure 6.3 (d). So we select 20 nm as the optimized thickness of the gold layer.

6.3.3 Optimization of TiO_2 Layer Thickness

In this design, a thin TiO_2 layer is used between the fiber and the gold layer to improve the adhesion of gold. Note that oxide of other metal could have been used instead of TiO_2. The reason behind using the oxide of titanium is the low loss and corrosion resistive nature of titanium. Using nitride of titanium instead of oxide results in very high CL and very low AS [104]. Hence, we preferred using TiO_2 over any other metal oxide or nitride. The thickness of the TiO_2 layer also alters the loss depth and the sensing performance of the sensor. Figure 6.4 (a) shows the change in loss depth due to the variation of TiO_2 layer thickness. The loss depth increases, and a red-shift of resonance wavelength occurs when t_t is raised. Nevertheless, a thicker TiO_2 layer (15 nm) broadens the loss peak, as shown in figure 6.4 (a), which results in a lower AS. AS for different values of t_t are depicted in figure 6.4 (b). The maximum AS (4197 RIU^{-1}) is obtained for t_t = 10 nm. Considering the AS, the optimized value of TiO_2 layer thickness is selected as 10 nm.

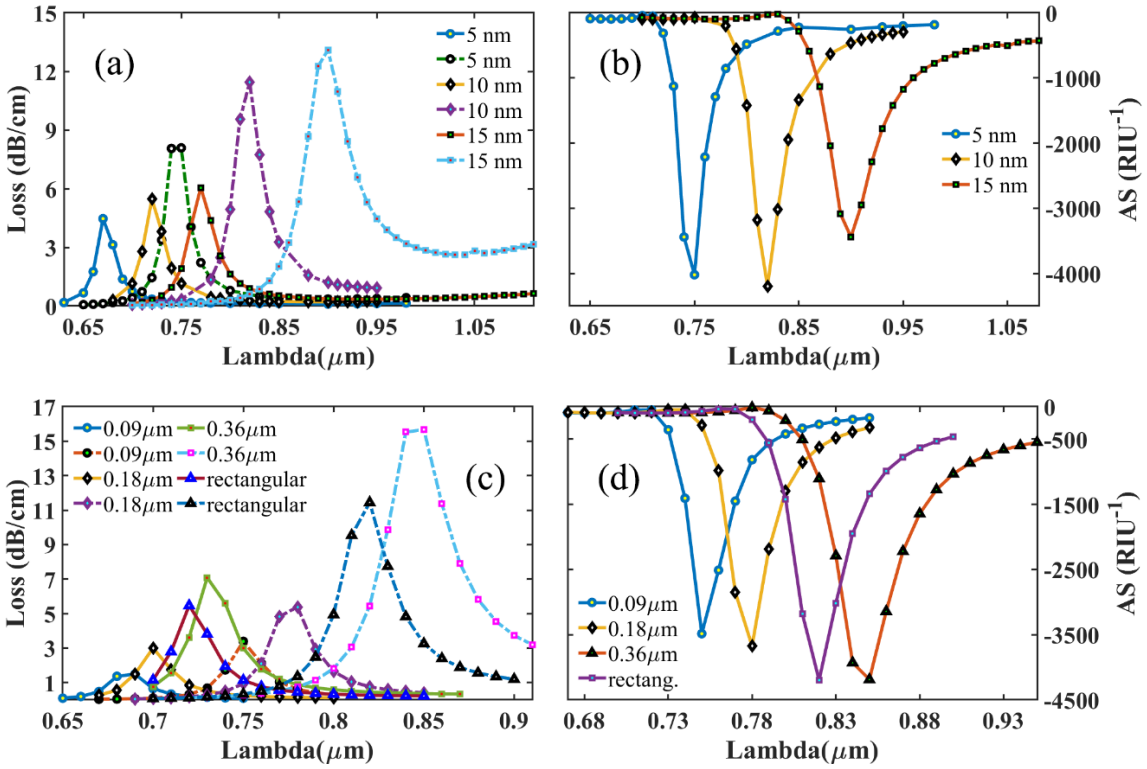

Figure 6.4: (a) Loss spectra for t_t = 5 nm, 10 nm, and 15 nm at analyte RI of 1.40 (solid lines) and 1.41 (dashed lines); (b) Amplitude Sensitivity for t_t = 5 nm, 10 nm, and 15 nm at analyte RI of 1.40; (c) Loss spectra for rectangular air hole and circular air hole with d_2 = 0.09 µm, 0.18 µm, and 0.36 µm at analyte RI of 1.40 (solid lines) and 1.41 (dashed lines); (d) Amplitude Sensitivity for rectangular air hole and circular air hole with d_2 = 0.09 µm, 0.18 µm, and 0.36 µm at analyte RI of 1.40

6.3.4 Effect of Different Core Structure

The rectangular air hole has an immense influence on the sensing performance of the sensor since it is responsible for generating the birefringence. Moreover, it helps in pushing the EM waves towards the analyte layer. Hence the height and width of the rectangular air hole must be selected prudently to achieve better sensitivity. Before optimizing these parameters, we will check the effect of replacing this rectangular air hole with a circular air hole having a diameter d_2. For different values of d_2, the loss depths are shown in figure 6.4 (c), whereas figure 6.4 (d) exhibits the AS. It can be observed that the AS improves with the increase of d_2, and for d_2 = 0.36 µm, AS (4188.2 RIU^{-1}) is almost equivalent to the AS (4196.7 RIU^{-1}) for a rectangular air hole. However, the circular air

hole gives zero birefringence. Thus we decide to retain the rectangular air hole. It is to be mentioned that we did not raise d_2 above 0.36 µm as that resulted in a very high loss.

6.3.5 Optimization of Height and Width of the Rectangular Air Hole in the Core

Now we will optimize the height and width of the rectangular air hole. After careful investigation, the maximum AS (4197 RIU^{-1}) is found at h = 0.4 µm. Thus, we select 0.4 µm as the optimum height and seek to optimize the width. After simulating for various values of widths, the optimized width is affirmed to be 0.22 µm. At w = 0.22 µm, the maximum AS is obtained to be 4238 RIU^{-1}. Loss depths and AS for different values of height and width are shown in figure 6.5. From this figure, it can be seen that CL increases with the increase of height and width. As increasing height or width increases the area of the air hole, the air hole is able to push more EM waves towards the cladding. As a result, an increase in CL is observed.

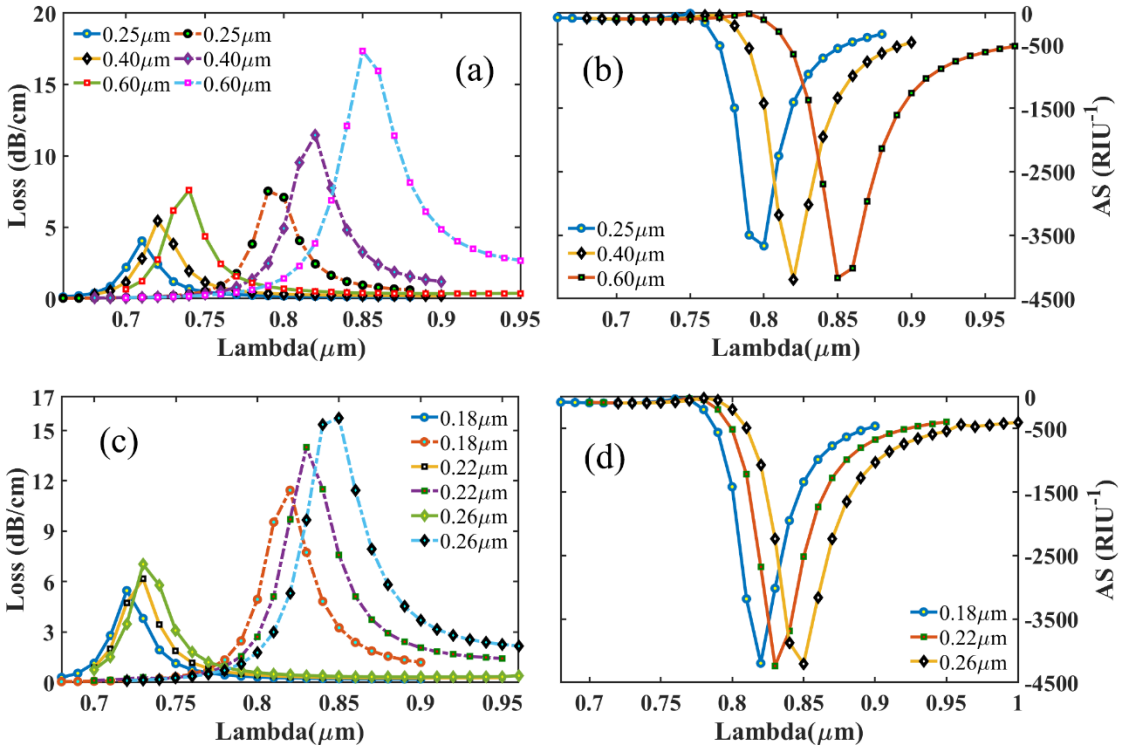

Figure 6.5: (a) Loss spectra for h = 0.25 µm, 0.40 µm, and 0.60 µm at analyte RI of 1.40 (solid lines) and 1.41 (dashed lines); (b) Amplitude Sensitivity for h = 0.25 µm, 0.40 µm, and 0.60 µm at analyte RI of 1.40; (c) Loss spectra for w = 0.18 µm, 0.22 µm, and 0.26 µm at analyte RI of 1.40 (solid lines) and 1.41 (dashed lines); (d) Amplitude Sensitivity for w = 0.18 µm, 0.22 µm, and 0.26 µm at analyte RI of 1.40

6.3.6 *Optimization of 'p'*

The value of *p* also has a significant impact on the sensing performance as various parameters are dependent on this. The initial value of the *p* was selected as 1.65 µm. First, we increase it to 1.75 µm and see that the AS gets reduced. So we decrease the value of *p* and calculate AS at *p* = 1.55 µm and 1.45 µm. The AS values for *p* = 1.65 µm, 1.55 µm and 1.45 µm are 4238 RIU^{-1}, 4572 RIU^{-1}, and 3778 RIU^{-1} respectively. The loss depths for different values of the *p* are shown in figure 6.6 (a). It is clear from figure 6.6 (a) that CL decreases due to the decrement of *p*. It is because the reduction of *p* brings the clusters closer to each other, which helps in better confinement of EM wave. Thus CL decreases, and AS increases (for changing *p* from 1.65 µm to 1.55 µm). However, for *p* = 1.45 µm, the sensitivity reduces since the clusters become so stuffed that the EM waves do not get enough channel width to interact with the analyte layer. Figure 6.6 (b) shows the AS for different values of *p*. As maximum AS is obtained for *p* = 1.55 µm, we choose this as the optimum value of *p*.

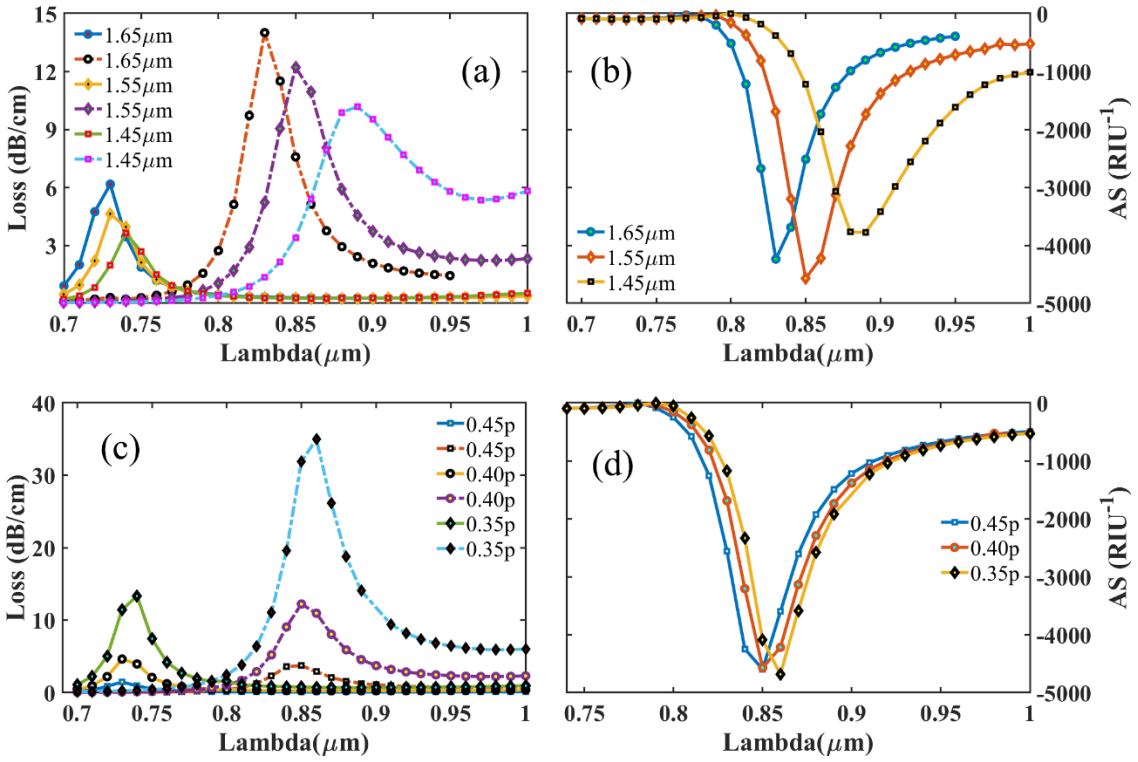

Figure 6.6: (a) Loss spectra for *p* = 1.65 µm, 1.55 µm, and 1.45 µm at analyte RI of 1.40 (solid lines) and 1.41 (dashed lines); (b) Amplitude Sensitivity for *p* = 1.65 µm, 1.55 µm, and 1.45 µm at analyte RI of 1.40; (c) Loss spectra for *d* = 0.45×*p*, 0.40×*p*, and 0.35×*p* at analyte RI of 1.40 (solid lines) and 1.41 (dashed lines); (d) Amplitude Sensitivity for *d* = 0.45×*p*, 0.40×*p*, and 0.35×*p* at analyte RI of 1.40

6.3.7 *Optimization of Air Hole Diameter 'd'*

At the fixed value of p and other parameters, we adjust the diameter of the air holes and observe the effect on AS. The diameter was set to $d = 0.40\times p$ initially, which showed AS of 4572 RIU^{-1}. Now we reduce the diameter to $0.35\times p$ and see that the AS becomes 4685 RIU^{-1}. Nevertheless, this improvement in AS comes with a tradeoff, which is the radical increment of loss peak. The loss increases as the smaller air holes cannot confine the EM waves properly. The loss becomes almost 2.9 times the initial loss, whereas the AS becomes 1.02 times the initial AS. The loss depths are shown in figure 6.6 (c), and the AS curves are shown in figure 6.6 (d). Due to the massive increase in loss depth, $0.35\times p$ cannot be taken as the optimal diameter. Hence we increase the diameter and set it to $0.45\times p$. At this diameter, AS increases slightly, whereas the loss decreases to a great extent due to the better confinement of EM waves by the larger air holes. Since an improved AS with lower CL is obtained for an increase in diameter, the diameter should be increased further. However, a further increment of d results in the overlapping of air holes. Thus we select $0.45\times p$ as the optimized diameter at which AS is found to be 4596 RIU^{-1}.

Till now, we have optimized all the essential geometrical parameters of the proposed sensor. It is to be mentioned that we have also investigated the effect of varying a, p_1, and r_c and discovered that the sensor gives the best performance at the initial values of these parameters. Hence the optimization of these parameters is not presented. Moreover, we did not address the optimization of geometrical parameters for y-polarization mode. Nevertheless, we have performed the optimization for y-pol simultaneously with x-pol and ascertained that the optimized values of these parameters are the same for both polarization modes.

6.3.8 *Sensor Performance at Optimized Parameters*

After optimization, the proposed sensor exhibited a maximum AS of 4596 RIU^{-1} for x-pol and 4557 RIU^{-1} for y-pol. Table 6.1 presents a performance comparison of the proposed sensor with the existing sensors. It is indisputable from Table 6.1 that our proposed sensor exhibits low loss and improved performance in terms of AS, WS, resolution, and birefringence.

Table 6.1 Performance comparison of the proposed sensor-1 with prior sensors

Ref.	Loss (dB/cm)		AS (RIU^{-1})	Resolution (Amplitude) (RIU)	WS (nm/RIU)	Resolution (Wavelength) (RIU)	Biref.
[105]	19.9		118	8.47×10^{-5}	1000	1.00×10^{-4}	-
[106]	60		72.47	1.38×10^{-4}	2520	3.97×10^{-5}	-
[107]	449.91		442.11	2.26×10^{-5}	6000	1.66×10^{-5}	-
[97]	700.05		318	3.14×10^{-5}	9000	1.11×10^{-5}	-
[108]	-		-	-	1131	8.84×10^{-5}	7.5×10^{-4}
[83]	-		1415	7.07×10^{-6}	62000	1.61×10^{-6}	1.2×10^{-3}
[85]	-		1411	7.09×10^{-6}	25000	4.00×10^{-6}	1.6×10^{-3}
[22]	-		1420	7.00×10^{-6}	11000	9.10×10^{-6}	-
[76]	-		1506	6.64×10^{-6}	30000	3.33×10^{-6}	-
[109]	-		1739.26	5.75×10^{-6}	9600	1.04×10^{-5}	-
[110]	-		2044	4.89×10^{-6}	12000	8.33×10^{-6}	-
[90]	-		2050	4.88×10^{-6}	111000	9.00×10^{-7}	-
This Work	x-pol	3.73	4596	2.18×10^{-6}	16000	6.25×10^{-6}	8.898×10^{-4}
	y-pol	4.48	4557	2.19×10^{-6}	17000	5.88×10^{-6}	

The simplistic formation of the stated PCF sensor makes its fabrication process straightforward. The standard Stack-and-Draw method can be employed to fabricate the circular-shaped air holes [83]. Fabrication of the rectangular-shaped air hole can be achieved using an extrusion technique and 3D printing technology [83]. The thin gold and TiO_2 coating can be implemented using chemical vapor deposition (CVD), high-pressure microfluidic chemical deposition, and wheel polishing methods [85]. Besides, the thin layer of gold can be coated on the curved surface using the atomic layer deposition (ALD) method [76] as well.

6.4 Conclusion

To summarize, we can say that we have a unique, highly birefringent, efficient PCF-SPR biosensor in this proposal. The arrangement of the clusters of circular air holes in the cladding region helps in maintaining a very high sensitivity. The FEM of COMSOL Multiphysics was used to simulate and optimize the structural parameters, and that is how we obtained the best output. As a result, we managed to achieve a very high amplitude sensitivity

(AS) of 4596 RIU^{-1} and 4557 RIU^{-1} for x- and y-polarization, respectively, using the amplitude interrogation method and a remarkable wavelength sensitivity (WS) of 16000 nm/RIU and 17000 nm/RIU for x- and y-polarization respectively applying the wavelength interrogation method. Moreover, the numerical value of the birefringence is found 8.8984×10^{-4} at refractive index 1.40, where the overall sensing range is from 1.33 to 1.41. The ultra-high sensitivity of this SPR biosensor is thought to contribute extensively to the detection of unknown biochemical analytes. In the next chapter, we will discuss another highly sensitive sensor having a rectangular air hole at the center.

Chapter 7

Proposed Design-2: Highly Birefringent Gold Coated Sensor Having Six Air Holes

7.1 Introduction

This chapter presents a unique and simply designed Surface Plasmon Resonance-based PCF biosensor that shows high sensing performance. Like the design discussed in the preceding chapter, this design also has a thin layer of gold (Au) surrounding the fiber. The strategic arrangement of the circular shaped air holes inside the fiber enhances the overall performance of the sensor. After precisely investigating the various fiber parameters, the maximum amplitude sensitivity was found to be 3.35×10^{3} RIU^{-1} for x-polarization and 5.00×10^{3} RIU^{-1} for y-polarization in a sensing range of refractive index 1.33-1.41. The sensor exhibited a maximum birefringence of 2.23×10^{-3} and a maximum wavelength sensitivity of 3.00×10^{4} nm/RIU and 3.25×10^{4} nm/RIU for x- and y-polarization, respectively. The sensor resolution (amplitude) is found to be 2.98×10^{-6} for x-polarization and 2.00×10^{-6} for y-polarization, whereas the sensor resolution (wavelength) is 3.33×10^{-6} and 3.08×10^{-6} for x-polarization and y-polarization, respectively. Moreover, we obtained a high figure of merit of 4.48×10^{2} RIU^{-1} for x-polarization and 4.44×10^{2} RIU^{-1} for y-polarization. The sensor proposed in this chapter shows much higher sensitivity and birefringence than the sensor discussed in the previous chapter. Moreover, it has the advantage of being simple structured. This sensor has six air holes in the core, whereas the previous one had thirty air holes. For simplicity in design and high performance, the biosensor discussed in this chapter also has a wide range of applications in the field of sensing unknown biomolecules and organic substances.

7.2 Structural Design and Theoretical Modelling

As we can see in figure 7.1 (a), we present a circular shaped lattice structure, which is simple in terms of geometric arrangement. The whole design and performance investigation has been done using the software COMSOL Multiphysics 5.3a. The outer structure of the fiber has several layers, starting with a 1.50 μm thick artificial absorbing

layer called Perfectly Matched Layer (PML), denoted as t_{PML} in the figure, which is used to avoid reflection of electromagnetic waves at the interface. Under the PML layer is the layer through which we will pass the biochemical analyte for detection, termed as t_a. The thickness of this layer is selected as 1.50 µm. We have two thin consecutive layers of gold (Au) and TiO_2 being termed as t_g and t_t in the figure, respectively. Here, the metallic layer of gold has been chosen to be the plasmonic material because it is chemically stable and gives broader shifts in resonance wavelength, and the TiO_2 layer has the function of improving the attachment of the gold layer with the fiber [85].

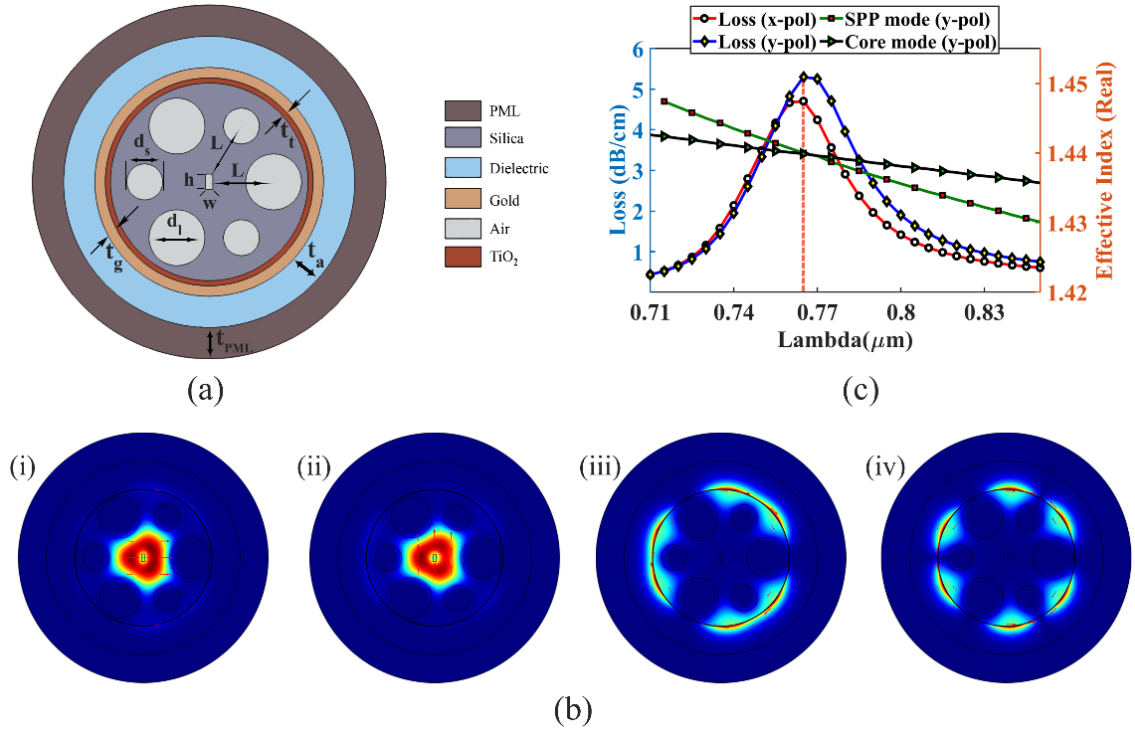

Figure 7.1: (a) Proposed biosensor model in 2D view; (b) Light energy distribution of i. core mode (x-polarization), ii. core mode (y-polarization), iii. SPP mode (x-polarization), iv. SPP mode (y-polarization); (c) SPP-core-guided mode dispersion relation at analyte RI = 1.39

In the cladding region, we have six circular-shaped air holes having two different diameters. The three larger air holes' diameter is denoted as d_l, and its numerical value is 2.145 µm. The three smaller air holes' diameter is designated as d_s, and its value is 1.375 µm. The gap between the subsequent air holes is given to maintain electromagnetic field flow towards the metal. All the air holes' centers are at a distance of 1.50×p from the fiber's geometric center, and L denotes this distance. Right at the fiber's geometric center, we have a rectangular air hole with a width (w) and height (h) of 0.18 µm and 0.4 µm, respectively.

We chose a rectangular-shaped air hole instead of a circular-shaped air hole at the center, intending to create a birefringence.

7.3 Analysis of Sensor Performance and Optimization Geometrical Parameters

7.3.1 Guiding Properties and Dispersion Characteristics

Figure 7.1 (b) portrays the proffered sensor's light energy allotment for core mode and SPP mode. At analyte RI 1.39, energy allotment of the core mode for x- and y-polarization are displayed in figure 7.1 (b) (insets i-ii). The insets (iii) and (iv) are the SPP mode's energy disposition for x- and y-polarization, respectively. It is noticeable from figure 7.1 (b) that tight confinement of light takes place in the core for both x- and y-polarization modes. A robust core mode-SPP mode coupling is formed for both polarization modes because of the reciprocal evanescent field-plasmonic metal interaction. However, the coupling for y-polarization is stronger in contrast with the coupling for x-polarization. It is to be mentioned that stronger coupling results in higher accuracy of unknown analytes detection. Figure 7.1 (c) illustrated the core-SPP dispersion correspondence when analyte RI was set to 1.39. The CL, along with the real values of the effective RI for both SPP mode and core mode, were plotted. The red and blue lines correspondingly represent the CL for x- and y-polarization modes. The black and green lines delineate the real values of effective RI for core mode and SPP mode. It is clear from the figure that 0.765 μm is the resonance wavelength at which phase-matching eventuates, and the utmost energy is resettled to SPP mode from the core mode [76]. Hence the CL is also maximum at this point.

7.3.2 RI Optimization

Different geometrical parameters of the PCF, for instance, gold film width (t_g), TiO_2 film width (t_t), height (h) and width (w) of the rectangular air hole, diameters (d_s, d_l) of the small and large air holes, pitch (p), etc. directly controls the performance of the sensor. Thus the values of these parameters must be selected prudently to procure an elite sensing performance. Initially, these parameters were set as t_g = 30 nm, t_t = 5 nm, h = 0.4 μm, w = 0.18 μm, d_s = 1.375 μm, d_l = 2.145 μm and p = 1.65 μm. However, the sensor may not exhibit the utmost performance at these magnitudes of the geometrical parameters. Hence

adjustment of these parameter magnitudes must be made. The optimization process should be carried out at a fixed RI of the analyte at which the highest sensitivity is obtained for the initial values of the parameters. When the parameters are set to their initial values, the effect of adjusting analyte RI from 1.33 to 1.41 is illustrated in figure 7.2.

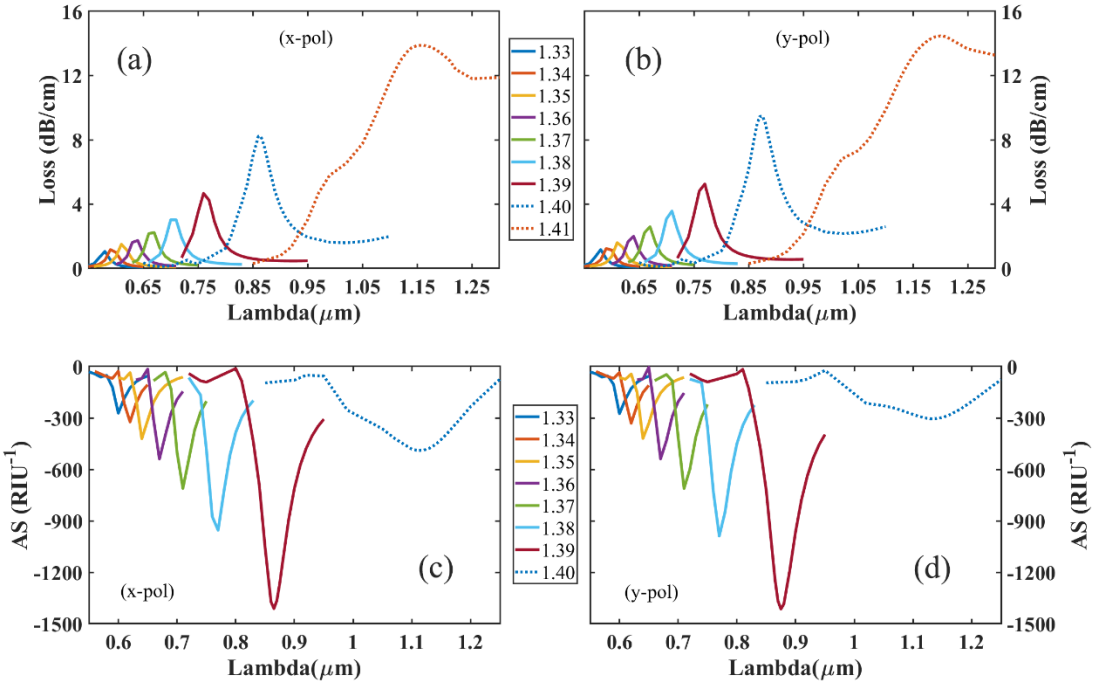

Figure 7.2: CL for different dielectric refractive indices (1.33-1.41) for x- and y-polarization (a-b); AS for different dielectric refractive indices (1.33-1.40) for x- and y-polarization (c-d)

Figure 7.2 (a-b) illustrates the change in CL due to RI variation for x- and y-polarization, respectively. It is glanceable that the RW resettles to the right as the analyte RI is increased. Any amendment to analyte RI effectuates a change in the n_{eff} (real) of SPP mode, which in terms results in either red-shift or blue-shift of the RW [76]. Considering the shift of RW, the maximum WS of the proffered sensor is found to be 3.00×10^4 nm/RIU for x-polarization and 3.25×10^4 nm/RIU for y-polarization. Figure 7.2 (c-d) demonstrates the effect of RI variation on the AS for x- and y-polarization. It is evident from figure 7.2 (c) and (d) that the highest sensitivity is obtained at RI = 1.39 for both polarization modes when the parameters were set to their initial values. Hence the optimization of the geometric parameters will be done at RI = 1.39. As mentioned earlier, the coupling for y-polarization is stronger than the coupling for x-polarization. Thus, we will focus on y-polarization mode while optimizing the geometrical parameters.

Our sensor's maximum resolution is obtained at analyte RI 1.40, and the corresponding values for x- and y-polarization are found to be 3.33×10^{-6} and 3.08×10^{-6}, assuming $\partial\lambda_{min}$ = 0.1 nm in equation 5.11. Note that while estimating the resolution, the external noise effects were not appraised. Therefore, the resolution mentioned above is the maximum expected resolution, which can also be termed 'maximum theoretical resolution' [101]. Moreover, depending on the amount of external noise, the sensor's resolution will fluctuate during practical applications.

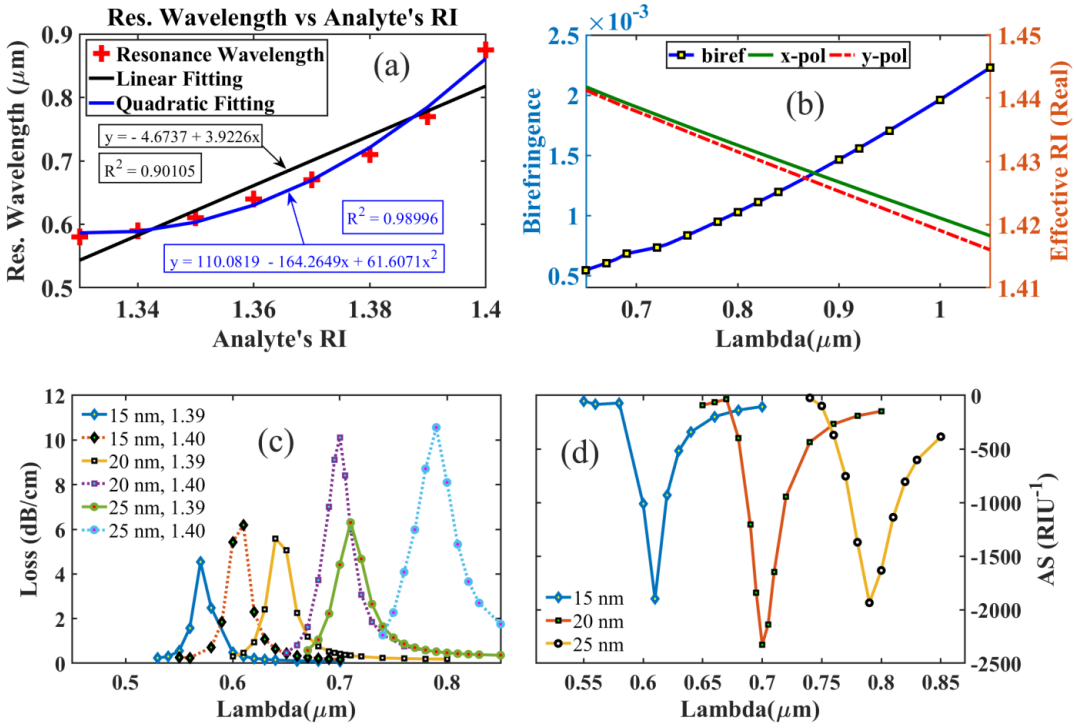

Figure 7.3: (a) Regression lines of the RW; (b) Birefringence and effective RI at dielectric RI of 1.39 for optimized parameters; (c) CL for dissimilar thicknesses (t_g) of gold film at dielectric refractive indices of 1.39 and 1.40; and (d) AS for dissimilar thicknesses (t_g) of gold film at a dielectric refractive index of 1.39

The linearity response of the regression line also indicates the sensor performance. An excellent sensor shows a high linearity response of the regression line. The linear (black line) and the 2nd order fitting (blue line) of the RW are shown in figure 7.3 (a). R^2 values of 0.90105 and 0.98996 are obtained for the linear fitting and the quadratic polynomial fitting, respectively, indicating better linearity.

The figure of merit (FOM) of this sensor was measured by equation 5.13. For analyte RI 1.33-1.40, the obtained FWHMs are 22.88, 25.56, 25.41, 29.17, 32.16, 36.79, 43.87, 66.90 nm for x-polarization and 22.66, 26.58, 26.35, 28.24, 30.98, 35.43, 45.38,

73.14 nm for y-polarization. The obtained FWHMs are very low, and as a result, our sensor shows high FOM. The maximum FOM is obtained at analyte RI 1.40, and the corresponding values for x- and y-polarization are 4.48×10^{2} RIU^{-1} and 4.44×10^{2} RIU^{-1}.

7.3.3 Gold Layer Thickness Optimization

The fundamental operation of a biosensor depends on the plasmonic material gold. The evanescent field interacts with the gold layer's electrons and generates a surface plasmon wave (SPW), which helps in the identification of an unidentified dielectric. Hence this layer's thickness (t_g) has a significant impression on the sensor performance. The results of varying the gold layer thickness (t_g) on CL and AS is demonstrated in figure 7.3 (c) and (d), respectively. The CL decreases with the reduction of t_g as gold has high damping loss property. Since a thinner gold layer enhances the analyte-evanescent field interaction, the sensor sensitivity rises with the reduction of t_g. Nevertheless, the skin depth limitation of the surface plasmon causes a decrement of AS when an extremely thin (t_g = 15 nm) gold layer is applied [83]. The highest AS is obtained for t_g = 20 nm. Hence, the optimum gold layer thickness is elected to be 20 nm.

7.3.4 TiO_2 Layer Thickness Optimization

In between the fiber and the gold layer, a thin film of TiO_2 is smeared to enhance the adhesion of gold. The TiO_2 layer improves the sensing capability of the sensor by providing additional electrons to the surface [85]. Hence, without this layer, the sensor exhibits low AS. However, if a thick layer of TiO_2 is applied, the AS decreases as the evanescent field cannot appropriately interact with the analyte layer. The CL and the AS for different thicknesses of the TiO_2 layer are manifested in figure 7.4 (a-b). As more energy is required to excite the additional electrons provided by the TiO_2 layer, the CL increases with the increase of t_t. The maximum AS is obtained for t_t = 5 nm, and thus 5 nm is selected as the optimum TiO_2 film thickness.

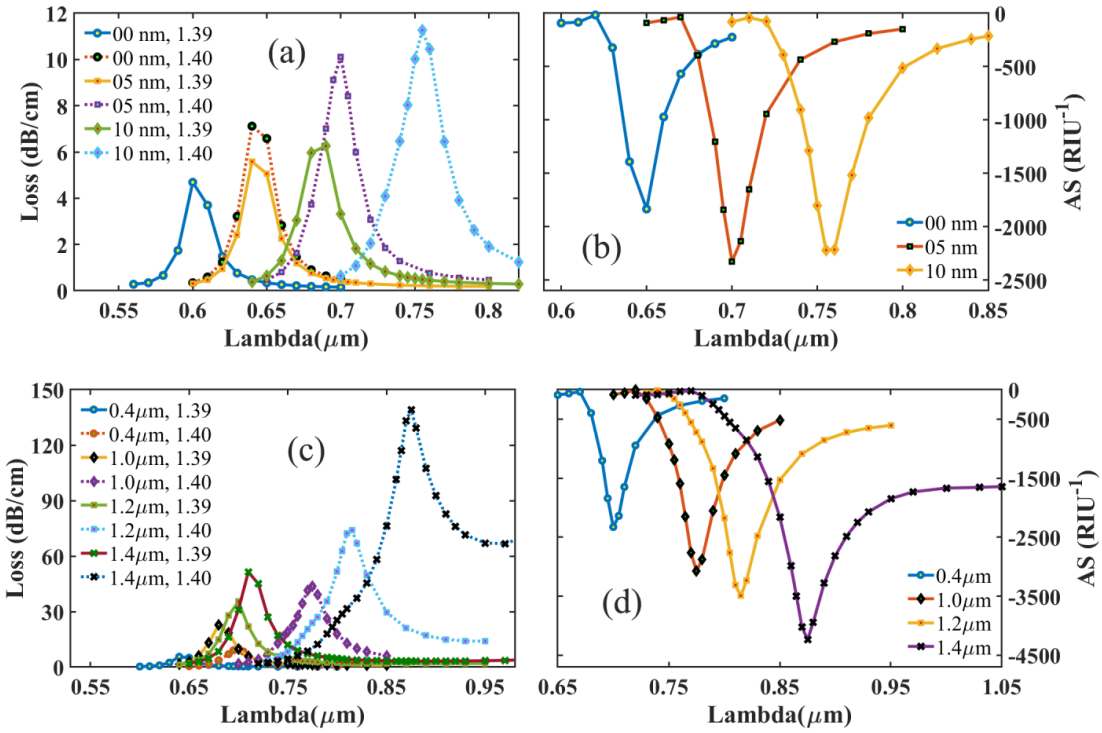

Figure 7.4: (a) CL for dissimilar thicknesses (t_t) of TiO_2 film at dielectric refractive indices of 1.39 and 1.40; and (b) AS for dissimilar thicknesses (t_t) of TiO_2 film at dielectric refractive index of 1.39; (c) CL for dissimilar heights (h) of rectangular air hole at a dielectric refractive indices of 1.39 and 1.40; and (d) AS for dissimilar heights (h) of rectangular air hole at a dielectric refractive index of 1.39

7.3.5 Rectangular Air hole Dimensions Optimization

The rectangular air cavity plays a vital role in the identification of incognito dielectrics as it pushes the evanescent field from the core to the outer analyte layer. This air hole also generates birefringence by introducing asymmetry in the design. When the height (*h)* of this air hole increases, it can deflect more evanescent field towards the sensing layer. As a result, the CL increases along with the AS. Figure 7.4 (c) and (d) show the effect of varying *h* on CL and AS, respectively. It can be seen that when the height is increased to 1.4 µm from 1.2 µm, the AS improves insignificantly, whereas the CL rises to a drastic extent. Considering the tradeoff between CL and AS, we decided to select 1.2 µm as the optimum height. The width (*w*) of this air hole has a similar effect on the CL and the AS. These effects are demonstrated in figure 7.5 (a-b). The CL and AS also increase when *w* is increased from its initial value. However, for *w* = 0.30 µm, the sensor shows a poor guiding

property. Hence the loss peak broadens, which in terms results in diminished AS. Thus, *w* = 0.24 µm is selected as the optimized width.

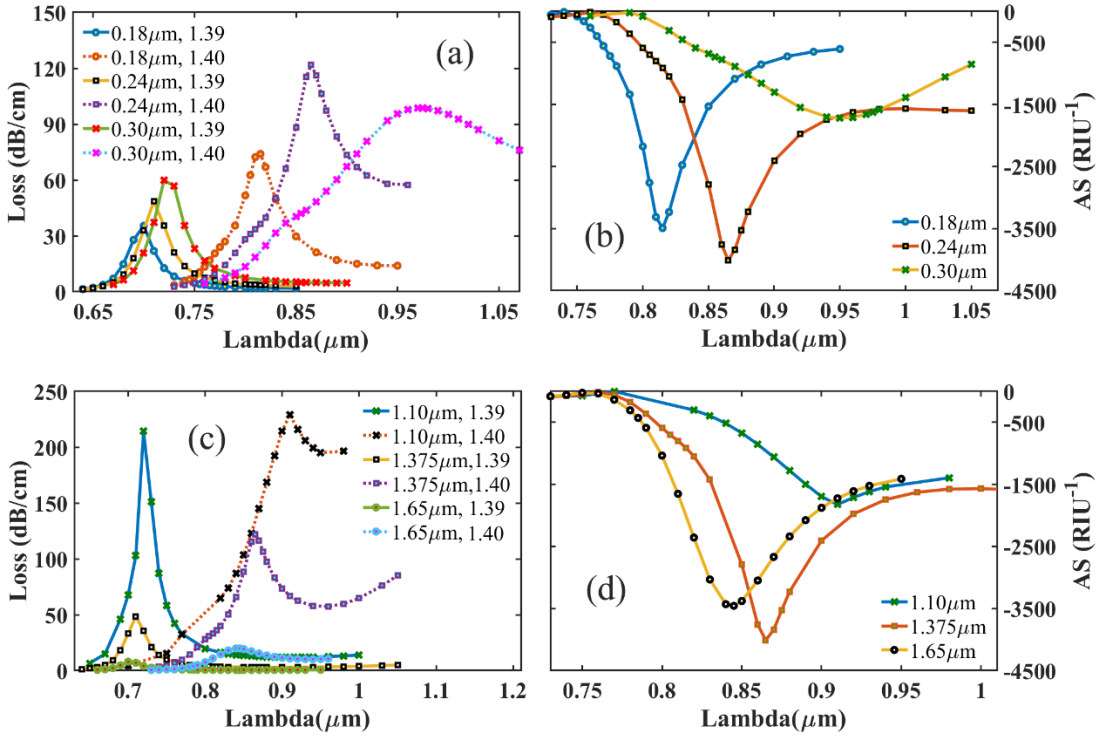

Figure 7.5: (a) CL for dissimilar widths (*w*) of rectangular air hole at dielectric refractive indices of 1.39 and 1.40; and (b) AS for dissimilar widths (*w*) of rectangular air hole at a dielectric refractive index of 1.39; (c) CL for dissimilar diameters (d_s) of small air hole at dielectric refractive indices of 1.39 and 1.40; and (d) AS for dissimilar diameters (d_s) of small air hole at a dielectric refractive index of 1.39

7.3.6 Circular Air Hole Diameters Optimization

The air hole diameters d_s and d_l have an immense impact on the sensing performance since these air holes create channels to guide the evanescent field towards the analyte layer. Larger air cavities are capable of confining the light better in the core, which results in lower CL. The larger the air holes, the narrower the channels between the core and the cladding. On the other hand, smaller air holes provide broader channels and higher CL. However, a suitable width of the channels must be allowed to facilitate proper dielectric-evanescent field interaction. It is to be stated that extensive channels lead to poor guiding property due to the scattering of light, and the sensitivity drops to a great extent. Hence, the diameters of the air holes should be selected accordingly to obtain a suitable

channel width. After careful investigation, it is affirmed that the sensor exhibits the best sensitivity when d_s is chosen as 1.375 µm, and d_l is selected as 1.98 µm. The effect of varying the d_s and d_l are displayed in figure 7.5 (c-d) and figure 7.6 (a-b), respectively.

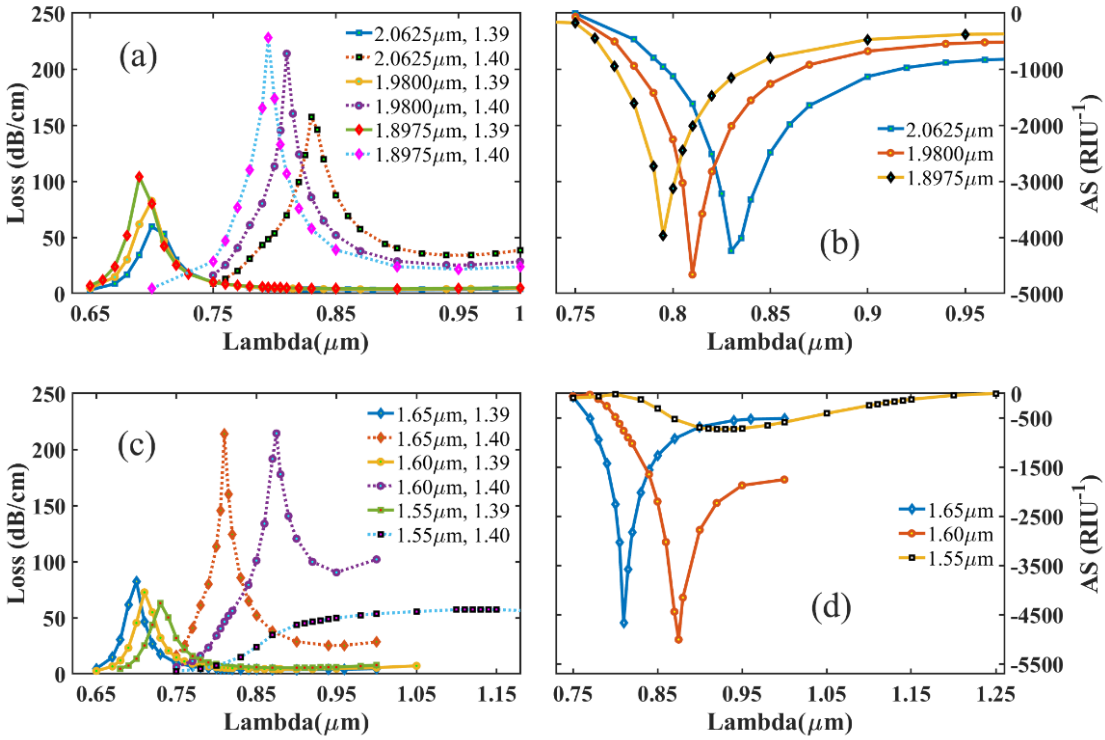

Figure 7.6: (a) CL for dissimilar diameters (d_l) of large air hole at dielectric refractive indices of 1.39 and 1.40; and (b) AS for dissimilar diameters (d_l) of large air hole at a dielectric refractive index of 1.39; (c) CL for dissimilar values of pitch (p) at dielectric refractive indices of 1.39 and 1.40; and (d) AS for dissimilar values of pitch (p) at a dielectric refractive index of 1.39

7.3.7 Pitch Optimization

Since the parameter *'p'* controls the distance between the air holes, it has an impression on the sensor performance. The originating magnitude of p was picked to be 1.65 µm. As p is reduced from its initial value, the air holes come closer to each other. As a result, the CL deteriorates due to the better confinement of light. However, for p = 1.55 µm, the air cavities become abutting to each other, which results in very narrow channels, and the light cannot interact with the analyte layer properly. Since the loss peak broadens for p = 1.55 µm, the AS drops drastically. Suitable channel width is achieved when p is

fixed to 1.60 µm. Thus, the optimum magnitude of *p* is elected to be 1.60 µm. The CL and AS for non-identical magnitudes of *p* are manifested in figure 7.6 (c-d).

7.3.8 Sensor performance at Optimized Parameters

At the optimized values of the geometrical parameters, the proposed sensor exhibited an extremely high AS of 5.00×10^{3} RIU^{-1} for y-polarization. The AS for x-polarization was also measured using the same parameter values, and the AS was ascertained to be 3.35×10^{3} RIU^{-1}. There exists a considerable difference in sensitivity between x- and y-polarization modes. This difference in sensitivity occurs due to the sensor's high birefringence property, which can be estimated by equation 5.12. A very high birefringence of 2.23×10^{-3} was achieved from our proposed sensor. At analyte RI 1.39, the proposed sensor's birefringence is displayed in figure 7.3 (b). Note that any amount of twist in a highly birefringent sensor alters the sensitivity [102]. Hence to avoid any curvatures or twist, a highly birefringent sensor should be handled with extreme caution during practical applications.

Table 7.1 Performance comparison of the proffered sensor-2 with the prevailing sensors

Ref.		AS (RIU^{-1})	Resolution (amp.) (RIU)	WS (nm/RIU)	Resolution (wave.) (RIU)	FOM (RIU^{-1})	Biref.
[108]		-	-	1.13×10^{3}	8.84×10^{-5}	-	7.5×10^{-4}
[83]		1.42×10^{3}	7.07×10^{-6}	6.20×10^{4}	1.61×10^{-6}	9.58×10^{2}	1.2×10^{-3}
[85]		1.41×10^{3}	7.09×10^{-6}	2.50×10^{4}	4.00×10^{-6}	5.02×10^{2}	1.6×10^{-3}
[76]		1.51×10^{3}	6.64×10^{-6}	3.00×10^{4}	3.33×10^{-6}	5.08×10^{2}	-
[109]		1.74×10^{3}	5.75×10^{-6}	9.60×10^{3}	1.04×10^{-5}	-	-
[110]		2.04×10^{3}	4.89×10^{-6}	1.20×10^{4}	8.33×10^{-6}	-	-
[90]		2.05×10^{3}	4.88×10^{-6}	1.11×10^{5}	9.00×10^{-7}	-	-
[84]		4.59×10^{3}	2.18×10^{-6}	1.70×10^{4}	5.88×10^{-6}	-	8.898×10^{-4}
[111]		5.65×10^{3}	1.77×10^{-6}	8.50×10^{3}	1.18×10^{-5}	-	-
This work	x	3.35×10^{3}	2.98×10^{-6}	3.00×10^{4}	3.33×10^{-6}	4.48×10^{2}	
	y	5.00×10^{3}	2.00×10^{-6}	3.25×10^{4}	3.08×10^{-6}	4.44×10^{2}	2.23×10^{-3}

Our proposed sensor showed an outstanding overall performance in contrast with the existing sensors. A performance contrast between our sensor and the existing sensors is presented in table 7.1. To the best of our knowledge, the birefringence of our sensor is higher than all other sensors. Note that our sensor has a lower WS than some of the existing sensors [83], [90]. Nevertheless, our proposed sensor has much higher AS and birefringence than those sensors. The sensor proposed in ref. [111] has an AS higher than our sensor. However, it is inferior to our sensor in terms of WS and birefringence. Considering AS, WS, resolution, FOM, and birefringence, it is indisputable that our proposed sensor exhibits improved performance than the existing sensors.

7.4 Conclusion

In this chapter, we have investigated a simple circular lattice design with a delicate layer of gold as the plasmonic material, maintaining the external sensing in a preferred way so that the evanescent waves can remarkably intensify the resonance effect. An appended layer of TiO_2 is exploited to benefit the adherence of gold on fiber. The exploited and optimized structural parameters exhibit improved numerical values of amplitude sensitivity of 3.35×10^{3} RIU^{-1} and 5.00×10^{3} RIU^{-1} respectively for x- and y-polarization as well as wavelength sensitivity of 3.00×10^{4} nm/RIU and 3.25×10^{4} nm/RIU respectively for x- and y-polarization modes in the sensing range from RI 1.33-1.41. Also, using amplitude and wavelength interrogation methods, the numerical values of the sensor resolution (amplitude) is found to be 2.98×10^{-6} for x-polarization, and 2.00×10^{-6} for y-polarization and sensor resolution (wavelength) is 3.33×10^{-6} for x-polarization and 3.08×10^{-6} for y-polarization. Moreover, a maximum birefringence of 2.23×10^{-3} is obtained that indicates the higher sensing characteristics. Furthermore, this design has the required feasibility to fabricate because of having only circular shaped air holes. Due to having the desired capability like high sensitivity and easy operation, we firmly believe that our recommended PCF based sensor will sense any unknown biomolecules with accuracy. The following chapter will discuss another highly sensitive birefringent sensor that does not require any rectangular air hole in the core.

Chapter 8

Proposed Design-3: Ultra-Sensitive & Highly Birefringent Biosensor without Rectangular Air Holes

8.1 Introduction

We proffer in this chapter a distinctive, facile to fabricate, and highly sensitive photonic crystal fiber biosensor based on the phenomenon of surface plasmon resonance. Our prototype has a strategic pattern of circular air holes inside the fiber, which leads to a superior sensing performance. The evaluation of all the sensor characteristics has been discharged by employing the finite element method (FEM) of COMSOL Multiphysics. The gold (Au) layer just around the fiber acts as the plasmonic material, and the TiO_2 increases the adhesivity of the gold layer and the fiber. After optimizing all the fiber parameters, we derived a maximum amplitude sensitivity and wavelength sensitivity of 5060 RIU^{-1} and 41500 nm/RIU, respectively, with a maximum sensor resolution of 2.41×10^{-6} for wavelength and 1.98×10^{-6} for amplitude. Moreover, the maximum figure of merit procured was 1068.7, and the maximum birefringence was found to be 1.568×10^{-3}. The overall analyte sensing range is from refractive indices 1.32 to 1.43, and the sensor has a fabrication tolerance limit of ±10%. Additionally, our sensor's temperature and strain sensitivities are estimated to be 0.75 nm/˚C and 3 pm/με, respectively along with a resolution (temperature) of 1.33×10^{-1} ˚C. In the previous two chapters, we have analyzed two sensors having birefringence. Both of them required a rectangular air hole at the core to create birefringence, and rectangular air holes are difficult to fabricate. The sensor discussed in this chapter exhibits considerable birefringence without any rectangular air hole, which makes the fabrication easier. With its enhanced performance in terms of sensitivity, we believe that this SPR based PCF biosensor can potentially contribute to the detection of unknown analytes and medical diagnostics applications.

8.2 Structural Modelling

The performance of a sensor highly depends on its structure. The structural design, i.e., the air holes' placement inside the core, determines the sensor's guiding characteristics,

regulating the sensor performance. For the sensor discussed in this chapter, a hexagonal lattice-based PCF structure with circular air holes and a gold coating is adopted for the external sensing-based SPR sensor. Figure 8.1 delineates the 2D cross-section of our proffered sensor. The interspace between the centers of two vicinal air cavities is defined as pitch and is symbolized by '*p.*' Two different diameters (d_1, d_c) of air holes are utilized for their advantageous behavior. In the cladding region, two hexagonal-shaped clusters, consisting of ten circular-shaped air holes with a bore of d_1, are put down opposite each other along the horizontal axis. Besides, six air holes with the same diameter d_1 create two v-shaped arrangements deposited along the vertical axis as mirror reflections. The prudent disposition of the air holes, having d_1 diameter, assists in forming four channels for the propagation of light from core to plasmonic mode. With the help of the concept perceived from the literature [83], [85], [90], the scaled-down corner air holes with a diameter of d_c are employed to limit the confinement loss since these air holes avert light scattering from the focal point of the sensor. The numerical value of these air holes diameter (d_c = 0.15 µm) has also been selected in accordance with the previously mentioned works. The constituent of the fiber is determined to be fused silica (SiO_2), which can be characterized by equation 5.1. There are several metals, such as copper (Cu), gold (Au), silver (Ag) that are utilized as the plasmonic material. Among them, gold shows chemically stable behavior in an aqueous environment and responds with a higher resonance peak. A thin gold layer is employed to encompass the cladding section, and the film thickness is denoted as t_g. A thin layer of TiO_2, having a thickness of t_t, is laminated in the midst of the fiber and the gold layer to reinforce their traction. Besides having nontoxic and compatible characteristics, this TiO_2 layer also improves the interaction between the analyte layer and the plasmons at the surface. Since the analyte layer thickness (t_a) is less significant in terms of sensing performance [32], an arbitrary thickness of 1.2 µm is decided for this layer. Here, an artificial perfectly matched layer with a thickness of t_{PML} = 1.5 µm is utilized at the outer portion of the computational area to absorb the scattered evanescent field. In a practical sensor, the PML layer is absent as it is employed only for better simulation purposes. After optimization, regular air hole diameter, pitch, gold and TiO_2 layer thicknesses were found to be d_1 = 0.95 µm, p = 1.00 µm, t_g = 20 nm, t_t = 10 nm respectively.

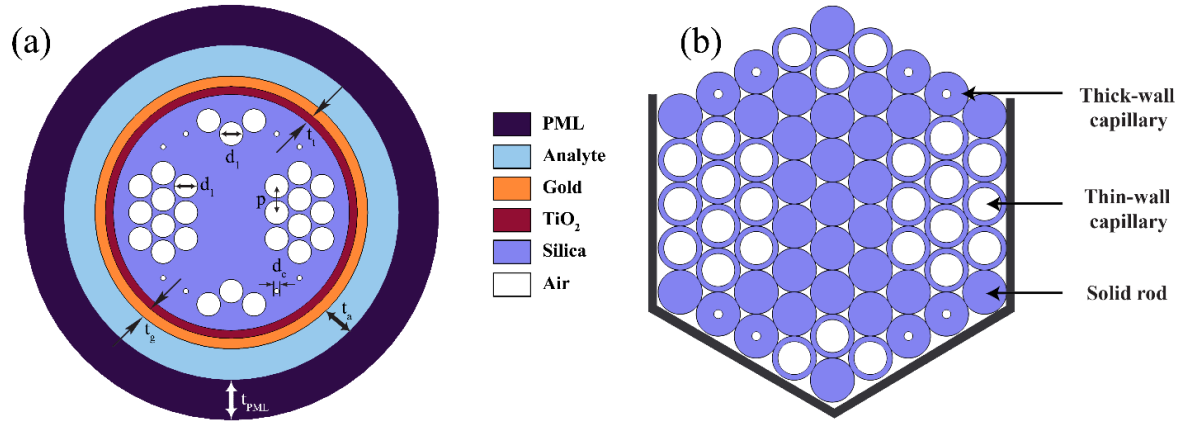

Figure 8.1: (a) Proposed sensor 2D cross-sectional view, (b) Proposed PCF stacked preform structure

8.3 Experimental Setup of the Proposed Sensor

Figure 8.2 depicts the experimental setup for this sensor. Initially, the incident light is launched from a supercontinuum light source having a spectrum range of 450 nm to 1600 nm. For this purpose, SuperK compact, NKTPhotonics™ can be used [112]. Later the light is transported through the polarizer that is accompanied by a polarizer-controller. With the help of a single-mode fiber (SMF-28), the polarized light then passes through the sensor. After passing through the sensor, the light then goes to an Optical Spectrum Analyzer (AQ6370C, Yokokawa™) via single-mode fiber [112].

A method called splicing has made it possible to couple the sensor with SMF-28 in a proper manner. The splicing can be done using the Vytran FFS-2000 splicer employing the filament fusion method, and the SMF and the PCF can be aligned using manual-mode translational and rotational alignment [113]. Another splicing method can be employed that connects the SMF and the PCF by inserting an etched SMF tip into the PCF, and this method has reported a coupling efficiency of 84.5% [114]. Moreover, researchers have reported many high-efficiency SMF-PCF couplers that can be used for our purpose as well [115], [116]. Therefore, our proposed sensor can be connected to an SMF with a coupling efficiency range of 80-90%.

As shown in figure 8.2, an analyte channel is implanted at a suitable position to facilitate the liquid analyte inlet and outlet. The analyte is injected inside the channel through a programmable micro injection pumper (LSP01-1A, LongerPump™) [112]. The channel's outlet is connected with a waste reservoir, where the used analyte will be stored. The existence

of several unknown analytes causes the resonance wavelength to shift towards higher or lower wavelengths. Through the optical spectrum analyzer, these spectrums can be detected. Lastly, the wavelength peak shifts are inspected via a computer where the final achieved SPR output spectrums are exhibited.

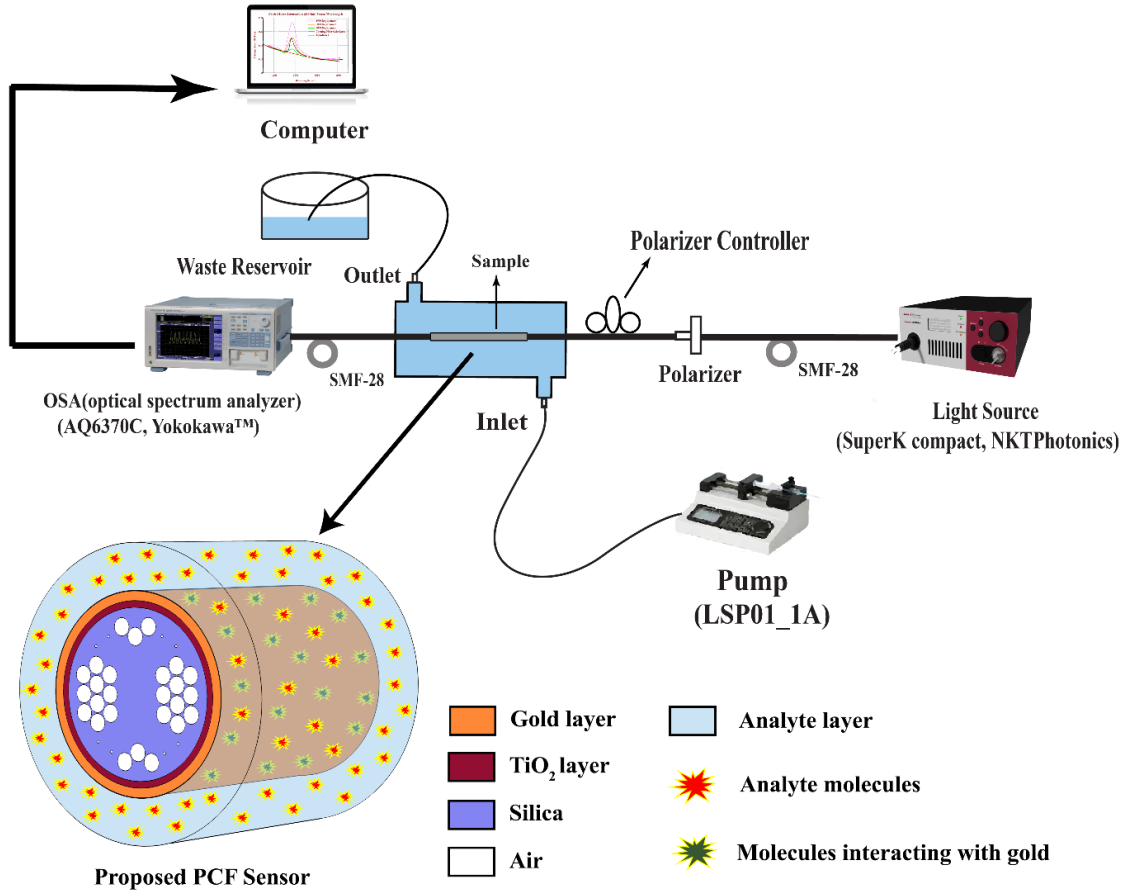

Figure 8.2: Experimental setup schematic of the proffered sensor for practical sensing applications

8.4 Performance Analysis of the Proposed Sensor

An accepted approach for analyzing the sensor performance is to optimize various geometrical parameters of the sensor and then evaluate the sensor behavior by varying the analyte RI. The optimization process incorporates keeping all parameters unaltered and varying one particular parameter in succession. This approach has been followed in many works [32], [85], [90], [117] reported to date. Therefore, we also followed this approach for the performance analysis of our propounded sensor. The geometrical parameters of our work include pitch magnitude (p), Au (t_g) and TiO_2 (t_t) layer widths, and diameters d_1 and d_c of the

air chambers, which were tuned to t_g = 25 nm, t_t = 10 nm, p = 1.00 µm, d_1 = 0.90 µm and d_c = 0.15 µm at the initial stage of optimization.

8.4.1 Guiding Properties and Dispersion Characteristics

A PCF can function as an SPR sensor when the light disseminated through its core interacts with the externally laminated metal layer and spawns the surface plasmon wave. In order to procure an enhanced sensing performance, the evanescent field should be maneuvered appropriately towards the metal layer so that it can easily interface with the metal layer electrons. The EM field dispersal of our lodged sensor for both x- and y-polarization modes are illustrated in figure 8.3. Tight confinement of light, which indicates low CL, can be realized from figure 8.3 (a) and (b). It is evident from figure 8.3 (c) and (d) that our suggested sensor manifests excellent guiding property due to the judicious placement of air holes. Appropriate evanescent field-metal layer interaction forms a robust core mode-SPP mode linkage. Note that, here, x-polarization (x-pol) and y-polarization (y-pol) mode refers to the response of the sensor due to the incidence of x-polarized light and y-polarized light, respectively.

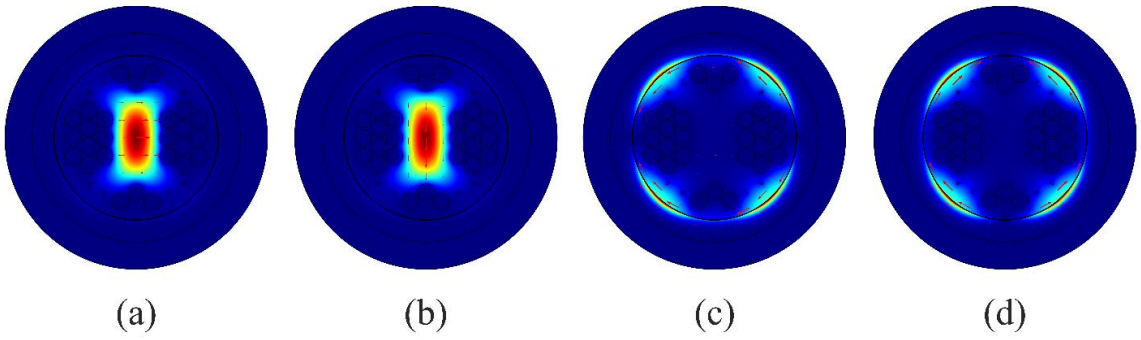

Figure 8.3: EM field dispersal of (a) core mode (x-pol), (b) core mode (y-pol), (c) SPP mode (x-pol), (d) SPP mode (y-pol)

The core mode-SPP mode dispersion relevance at analyte RI of 1.37 is elucidated in figure 8.4. The real portion of effective RI (n_{eff}) of both core mode and SPP mode decreases as the wavelength of the incident light increases. It can be realized from figure 8.4 that the n_{eff} (real) of SPP mode has a higher decrement rate by contrast. Hence, the lines indicating the n_{eff} (real) intersect at a specific wavelength, termed as resonance wavelength. This condition is referred to as the phase-matching condition, and at this condition, the frequencies of the evanescent field and the metal electrons become identical. As a result,

resonance occurs, and energy transplant from core mode to SPP mode reaches the maximum, which gives a sharp peak in the CL curve. It can be observed from figure 8.4 (a) and (b) that, in our case, 0.665 µm is the RW, and the CL is maximum at this point for both x- and y-polarization. However, x-pol shows higher CL compared to y-pol, which implies stronger coupling for x-pol. Therefore, the optimization of the parameters will be carried out, focusing on the x-polarization mode.

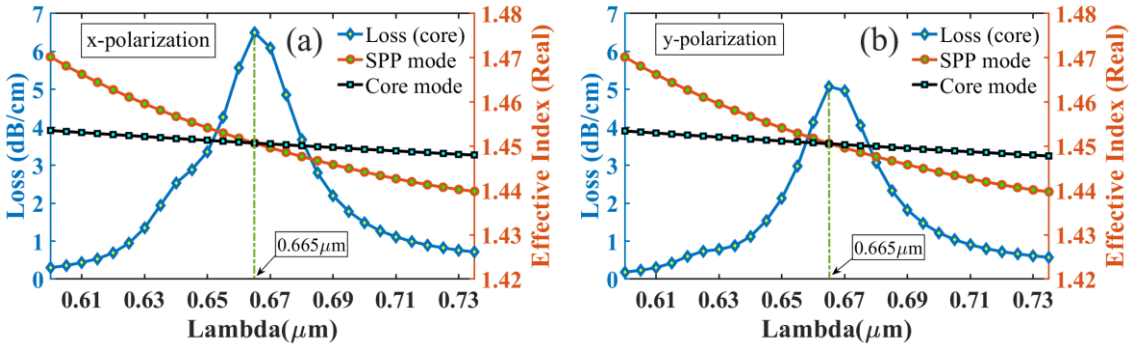

Figure 8.4: SPP-Core mode dispersion relation at analyte RI of 1.37 for (a) x-polarization; (b) y-polarization

8.4.2 Analysis of Gold (t_g) and TiO_2 (t_t) film thicknesses

By generating the SPW, the gold film triggers the sensing ability in a PCF, and the TiO_2 film reinforces it by engendering ample electrons at the surface [90] and by enhancing the adhesion of gold with the fiber. Therefore, these layers have a consequential impact on sensor performance. The thicknesses of these films unequivocally govern the RW shift and the CL peak. It is glanceable from figure 8.5 (a) and (b) that contraction of either the gold layer or the TiO_2 layer effectuates a scaling down of the n_{eff} (real) of SPP mode, which catalyzes a blue-shift of RW.

The reduction of t_g from its inceptive value (25 nm) enhances the sensitivity since a thinner gold film facilitates a smooth analyte-evanescent field interaction. However, for a skinny gold layer (t_g = 15 nm), the sensitivity drops owing to the CL peak broadening and the skin depth limitation of the surface plasmons [83]. Therefore, 20 nm is determined to be the optimum thickness of the gold film since the highest AS is attained at this thickness.

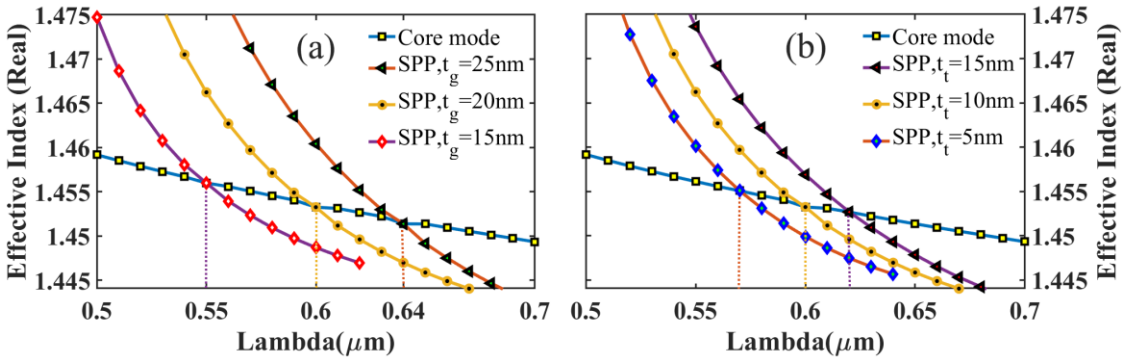

Figure 8.5: Core-SPP mode dispersion relation for different thicknesses of (a) gold layer, (b) TiO_2 layer

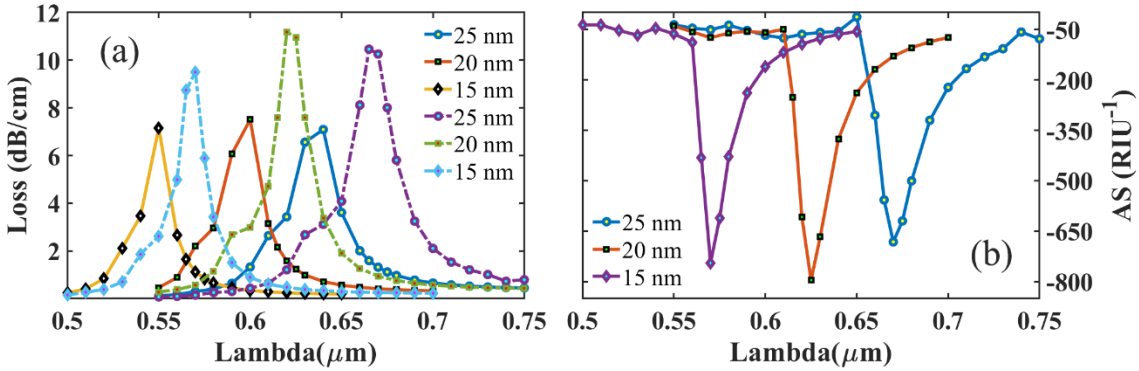

Figure 8.6: (a) Confinement loss curves at analyte RI of 1.37 (solid lines) and 1.38 (dashed lines) for t_g = 15 nm, 20 nm, 25 nm; (b) Amplitude Sensitivity curves for t_g = 15 nm, 20 nm, 25 nm at analyte RI of 1.37

The TiO_2, having a high RI, plays the role of a transition metal and helps in alluring the evanescent fields from the core [90]. As a consequence, the sensitivity escalates on account of an augmented plasmonic metal-evanescent field interaction. Moreover, a thicker TiO_2 film leads to elevated CL, which can be visualized from figure 8.7 (a). However, if a very thick layer of TiO_2 is smeared, the sensitivity diminishes as the evanescent field cannot interact properly with the analyte. In the case of our design, a TiO_2 film of 10 nm thickness facilitates the metal-evanescent field interaction and exhibits an excellent sensitivity. Thus, 10 nm is chosen as the optimum thickness for TiO_2 film. The effect of altering t_g and t_t on CL (inset 'a') and AS (inset 'b') can be realized in figure 8.6 and figure 8.7, respectively.

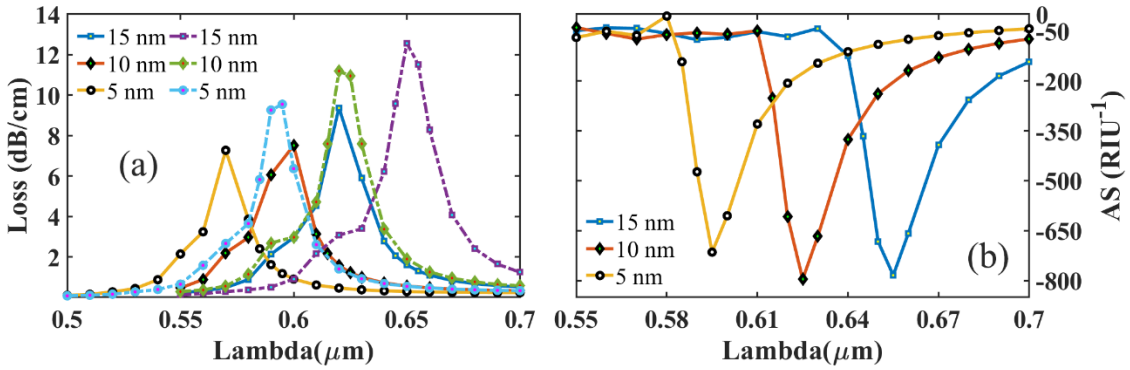

Figure 8.7: (a) Confinement loss curves at analyte RI of 1.37 (solid lines) and 1.38 (dashed lines) for t_t = 5 nm, 10 nm, 15 nm; (b) Amplitude Sensitivity curves for t_t = 5 nm, 10 nm, 15 nm at analyte RI of 1.37

8.4.3 Analysis of pitch (p) and air hole diameter (d_1)

Air cavities are stationed inside the PCF to incarcerate the light in the core region. These air holes also aid in ushering the light towards the plasmonic layer via specific channels. Hence the diameter (d_1) of these air holes and the interspace between two vicinal air holes, termed as pitch (p), bridles the CL. Note that the RW is immune to the changes in these two parameters, and this fact can be perceived from figure 8.8 (a) and 8.9 (a). Widening the air holes comes with the advantage of upgraded confinement and guiding of light, which in terms minimizes the CL and ameliorates the sensitivity. On the other hand, shrinking the air holes gives rise to CL and deteriorates the AS due to the impaired guiding property. Therefore, the diameter (d_1) of the air cavities are upraised to a value of 0.95 µm from the preliminary value of 0.90 µm. Further expansion of air cavities is halted to avert their overlapping and to mitigate the fabrication complexity. Figure 8.8 (a-b) delineates the phenomena mentioned above.

In our design, the disposition of air holes is executed in such a way so that enlarging the pitch prompts the clusters to occupy more area, which in terms lowers the CL by improving the light confinement. Nevertheless, the AS gets truncated as a tradeoff. The downgrading of AS can be explicated by the fact that the light cannot interact appropriately with the plasmonic layer due to the shrinkage of the channels towards the metal layer. Moreover, reduction of pitch is not feasible since that results in the imbrication of air holes. The pitch value for our design is preferred as 1.00 µm considering all aspects. Figure 8.9 (a-b) manifests the consequences of pitch alteration on the CL and AS, respectively.

Information regarding the optimization of various parameters at analyte RI of 1.37 is given in Table 8.1.

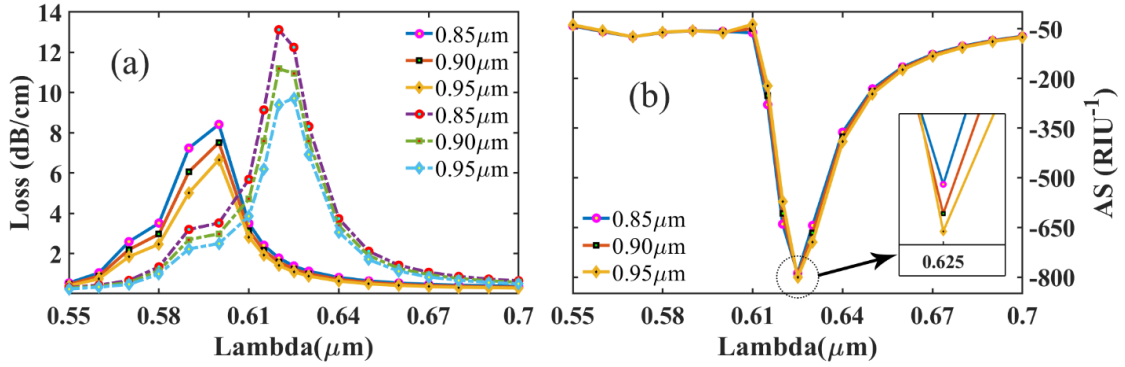

Figure 8.8: (a) Confinement loss curves at analyte RI of 1.37 (solid lines) and 1.38 (dashed lines) for d_1 = 0.85 µm, 0.90 µm, 0.95 µm; (b) Amplitude Sensitivity curves for d_1 = 0.85 µm, 0.90 µm, 0.95 µm at analyte RI of 1.37

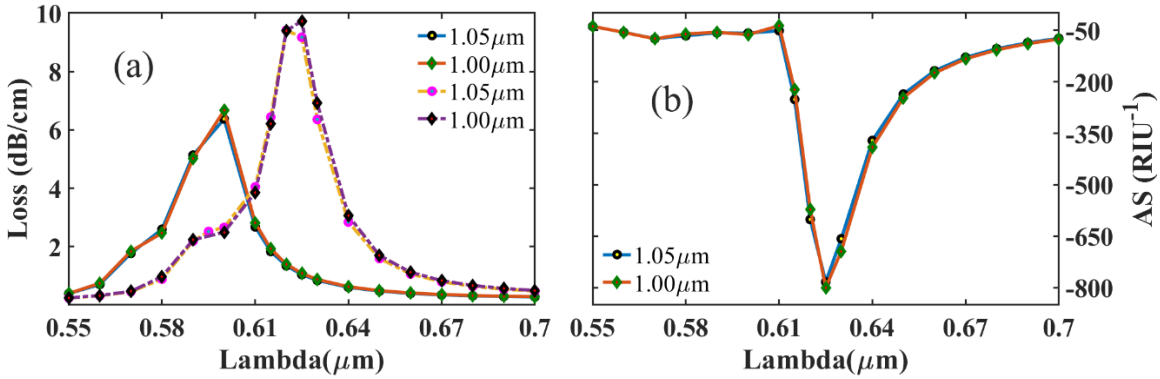

Figure 8.9: (a) Confinement loss curves at analyte RI of 1.37 (solid lines) and 1.38 (dashed lines) for p = 1.00 µm, 1.05 µm; (b) Amplitude Sensitivity curves for p = 1.00 µm, 1.05 µm at analyte RI of 1.37

Table 8.1 Optimization of different parameters of proffered sensor-3 at analyte RI 1.37

Parameter	Dimension	Peak CL (dB/cm)	AS (RIU^{-1})
t_g	15 nm, 20 nm, 25 nm	7.15, 7.51, 7.09	744.4, 795.6, 681.8
t_t	5 nm, 10 nm, 15 nm	7.27, 7.51, 9.37	714.4, 795.6, 783.8
d_1	0.85 µm, 0.90 µm, 0.95 µm	8.41, 7.51, 6.66	788.4, 795.6, 800
p	1.00 µm, 1.05 µm,	6.66, 6.37	800, 783

8.4.4 Sensor Performance at Optimized Parameters

Incognito analyte detection methodology of a sensor incorporates monitoring the CL and the shift of RW. The more alteration in the CL and RW, the better the sensor performance. Figure 8.10 (a-b) depicts the variation in CL and RW due to the change in analyte RI for x- and y-polarization modes. The CL proliferates, and the RW relocates to the right when analyte RI is raised and vice-versa. We conducted the sensor performance analysis in the RI range of 1.32-1.43 with an interval of 0.01, and the RW shifts were noticed to be 10 nm, 10 nm, 15 nm, 20 nm, 20 nm, 25 nm, 35 nm, 50 nm, 75 nm, 145 nm, 305 nm for x-pol and 10 nm, 10 nm, 15 nm, 20 nm, 20 nm, 25 nm, 35 nm, 50 nm, 80 nm, 170 nm, 415 nm for y-pol. The sensor exhibited an average WS of 6454.55 nm/RIU and 7727.27 nm/RIU for x- and y-pol, respectively, which are comparatively high compared to the most other existing SPR based sensors. The maximum shift in RW (305 nm for x-pol and 415 nm for y-pol) is achieved when analyte RI is adjusted from 1.42 to 1.43. A distinctly steep WS of 30500 nm/RIU (x-pol) and 41500 nm/RIU (y-pol) results from this massive RW shift. The exorbitant value of WS is a manifestation of higher detection accuracy, which connotes excellent sensor resolution. The max resolution (wavelength) of our sensor is found to be 3.28×10^{-6} for x-pol and 2.41×10^{-6} for y-pol. Amendment of analyte RI deliberately influences the CL characteristics, which thereby revamps the AS to a substantial extent. Figure 8.10 (c-d) render information regarding the adaptation of AS to the modification of RI for x- and y-pol. It is indisputable that the AS is proportionate to RI, and with the increase of RI, AS also improves. However, at analyte RI of 1.43, the CL peak curtails along with a broadening of the peak, which effectuates a drastic truncation in AS. Regardless of that, a max AS of 5060 RIU^{-1} (x-pol) and 4735 RIU^{-1} (y-pol) is achieved at an analyte RI of 1.41, whereas the corresponding average AS is 1327 RIU^{-1} and 1266.5 RIU^{-1}. Additionally, the max resolution of our sensor in terms of AS is noted to be 1.98×10^{-6} for x-pol and 2.11×10^{-6} for y-pol. The average AS, the maximum AS, the resolution (wavelength), and the resolution (amplitude) of our proposed sensor surpasses almost all other existing sensors.

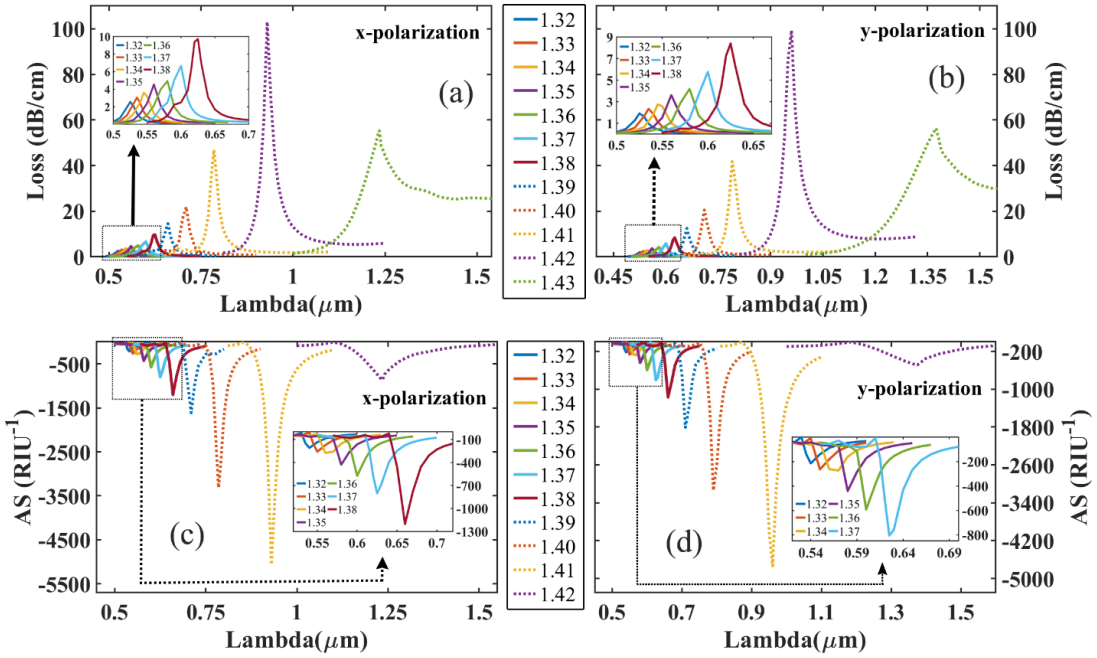

Figure 8.10: Confinement loss curves for analyte RI from 1.33 to 1.43 for (a) x-pol, (b) y-pol; and Amplitude sensitivity curves for analyte RI from 1.33 to 1.42 for (c) x-pol, (d) y-pol

Table 8.2 Performance of proposed sensor-3 for analyte RI 1.32-1.43

RI	CL (dB/cm)		RW (nm)		WS (nm/RIU) (×10^3)		Resolution (WS) (×10^{-6})		AS (RIU^{-1})		FWHM		FOM		Biref. (×10^{-4})
	x	y	x	y	x	y	x	y	x	y	x	y	x	y	
1.32	2.6	1.9	525	525	1.0	1.0	100	100	210	214	20	18	51	55	1.297
1.33	3.1	2.3	535	535	1.0	1.0	100	100	260	263	20	18	50	56	1.297
1.34	3.6	2.8	545	545	1.0	1.0	66.7	66.7	275	273	21	19	71	79	1.485
1.35	4.5	3.6	560	560	2.0	2.0	50	50	428	441	20	18	98	109	1.620
1.36	4.9	4.2	580	580	2.0	2.0	50	50	574	592	24	21	83	96	1.761
1.37	6.7	5.8	600	600	2.5	2.5	40	40	800	806	23	21	111	121	1.987
1.38	9.7	8.4	625	625	3.5	3.5	28.6	28.6	1202	1171	22	21	161	169	2.40
1.39	14.6	12.5	660	660	5.0	5.0	20	20	1614	1810	23	22	222	226	2.851
1.40	21.9	20.5	710	710	7.5	8.0	13.3	12.5	3313	3139	25	25	301	325	3.913
1.41	46.9	41.8	785	790	14.5	17.0	6.9	5.88	5060	4735	25	28	583	600	6.58
1.42	103	99.3	930	960	30.5	41.5	3.28	2.41	862	488	29	39	1068	1053	15.68
1.43	55.3	56.4	1235	1375	-	-	-	-	-	-	-	-	-	-	14.23

In addition to the upgraded AS and WS, our proposed sensor evinced magnificent results in terms of FOM. For distinct analyte RIs in the range of 1.32-1.42, the FWHM ranged from 17 nm to 40 nm, which are reasonably low. Lower FWHM implies a sharper resonance peak, which is a prerequisite for an eminent sensor. Moreover, as mentioned

earlier, our sensor presents top-notch WS. Therefore, our sensor manifests astounding FOM values, among which the maximum value is obtained to be 1068.7 (x-pol) and 1053.7 (y-pol) at analyte RI of 1.42. FWHM and FOM values for individual RI are provided in Table 8.2.

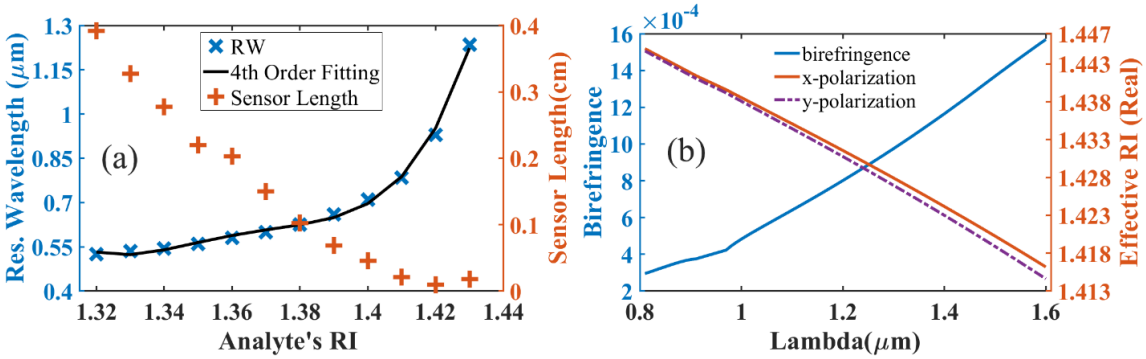

Figure 8.11: (a) Plotting of RW and sensor length with varying analyte RI; (b) Plotting of birefringence and n_{eff} (real) as a function of lambda

The RW for varying analyte RI is plotted in figure 8.11 (a), which also includes the 4th order polynomial fitting curve. The fitting curve, which has the coefficient of determination R^2 = 0.9973, can be expressed by the equation $y = A + Bx + Cx^2 + Dx^3 + Ex^4$. Here, x denotes the analyte RI, y symbolizes the RW, and A, B, C, D, and E coefficients have the corresponding values of 90145.03, - 265103.73, 292333.28, - 143257.03, and 26323.65. The prominent R^2 value embodies the enhanced performance of the sensor. Figure 8.11 (a) also displays the sensor lengths for different RI. Sensor length, being inversely proportional to the CL, contracts with the increment of RI. It is understandable from the figure that sensors having a length in the order of millimeter to centimeter can be utilized in practical sensing applications.

As a supplementary performance parameter, we study the birefringence of our sensor. In works reported early on [61], [83], [118], a rectangular air hole was implemented to instigate birefringence. The introduction of a rectangular air hole comes with the tradeoff of fabrication complexity. Having that said, our sensor shows a max birefringence of 1.568×10^{-3} at analyte RI 1.42 without the usage of a rectangular air hole. The strategic placement of circular air holes in our design assisted in attaining a noticeable birefringence without additional fabrication intricacy. The birefringence of our sensor at analyte RI 1.42 is plotted in figure 8.11 (b).

We carried out the sensor performance evaluation in the RI range of 1.32-1.43. This range of RI is of the essence because numerous essential biological agents and biochemical solutions have RI in this range. Some of the prominent analytes that can be identified by our sensor are acetone (1.36), silicone oil (1.403), ethanol (1.361), 50% sugar solution (1.42), glucose solution in water (10% solution = 1.3477, 20% solution = 1.3635), ethylene tetrafluoroethylene (1.403), White Blood Cell (1.36), human liver (1.369), blood plasma (1.35), human urine concentration (1.3415-1.3464), human intestinal mucosa (1.329-1.338), Red Blood Cell (1.40), hemoglobin (1.38), cervical cancer cell (HeLa), skin cancer cell (Basal), blood cancer cell (Jurkat), adrenal gland cancer cell (PC12), breast cancer cells (MDA-MB-231 and MCF-7) (1.36-1.40) and so on [85], [99], [117], [119]. Note that the previously reported SPR based biosensors have a sensing range indistinguishable from our sensor [32], [83], [85], [90], [117], [118]. The values of different performance parameters of the sensor at different RI is available in Table 8.2. Table 8.3 compares our proposed sensor and existing sensors in terms of AS, WS, resolution, birefringence, and FOM.

Table 8.3 Comparison between the proposed sensor-3 and the existing sensors in terms of AS, WS, resolution, FOM, birefringence and sensing range

Ref.		Amplitude Sensitivity (RIU^{-1})		Wavelength Sensitivity (nm/RIU)		Resolution (RIU)		FOM	Biref.	Sensing range
		Max.	Average	Max.	Average	Amplitude	Wavelength			
[27]		6829	2978.3	28000	6555.56	1.46×10^{-6}	3.57×10^{-6}	2800	-	1.33-1.42
[31]		1411	683.8	25000	9200	7.09×10^{-6}	4.00×10^{-6}	502	1.60×10^{-3}	1.33-1.38
[12]		1170	-	34000	-	8.55×10^{-6}	2.94×10^{-6}	310	-	1.32-1.41
[29]		2050	-	111000	-	4.88×10^{-6}	9.01×10^{-7}	-	-	1.33-1.43
[30]		1415	497.3	62000	11400	7.07×10^{-6}	1.61×10^{-6}	1140	1.20×10^{-3}	1.33-1.43
[26]		780	-	16000	6666	1.28×10^{-6}	6.25×10^{-6}	400	-	1.40-1.46
[45]		-	-	1131	-	-	8.84×10^{-5}	-	7.50×10^{-4}	-
[20]		1506	734.83	30000	9000	6.64×10^{-6}	3.33×10^{-6}	508	-	1.33-1.39
[41]		1189.5	-	13000	-	8.41×10^{-6}	7.69×10^{-6}	-	2.80×10^{-3}	1.33-1.40
[28]		4596	-	17000	-	2.18×10^{-6}	5.88×10^{-6}	-	8.90×10^{-4}	1.33-1.41
This Work	x	5060	1327	30500	6454.55	1.98×10^{-6}	3.28×10^{-6}	1068	1.57×10^{-3}	1.32-1.43
	y	4735	1266.5	41500	7727.27	2.11×10^{-6}	2.41×10^{-6}	1053		

8.4.5 Fabrication of the Proposed Sensor and Fabrication Tolerance Investigation

Fabrication is an important aspect of our proposed sensor since we have conducted a simulation-based study only. The pre-eminent performance of the proposed sensor will have no significance if the sensor is not practically accomplishable. For that reason, we suggest fabrication techniques that can be implemented to forge our sensor at this juncture. We have configured our sensor in such a way so that the stack-and-draw method can be implemented to manufacture the sensor [120]. The circular air holes can be originated by drilling the capillary rods at the preform stage with the help of an ultrasonic mill [32]. The preforms can be stacked after drilling, as shown in figure 8.1 (b), and then they can be drawn using a drawing tower [120]. Solid, thin-wall, and thick-wall rods can be used in the stack to form the different sized air cavities. After assembling the fiber framework, thin layers of TiO_2 and gold needs to be varnished on it. Atomic layer deposition (ALD), wheel polishing, high-pressure microfluidic chemical deposition, and chemical vapor deposition (CVD) methods can be adopted to overlay the fiber with thin gold and TiO_2 films [32], [76], [85], [117]. Hence, our sensor can be easily fabricated using existing fabrication technologies.

However, these fabrication techniques cannot achieve precise dimensions while manufacturing the sensor. Generally, there is always ±1% or ±2% variations from the desired structure dimensions, which introduces the necessity of fabrication tolerance (FT) analysis [117]. We have done the FT analysis for our sensor by modifying d_1 and d_c by ±5% and ±10% from their optimum value, which allows an extensive range of errors during the fabrication process. Figure 8.12 (a-b) shows that ±5% and ±10% variation of d_1 and d_c do not change the RW. Thus, the WS of our proposed sensor remains unaltered even after ±10% calibration of the design parameters. The CL is rectified marginally due to these tuning. Nevertheless, this CL alteration occurs for all RI, and hence, the relative change in AS is minimal. A maximum change of 1.26% and 1.34% in the AS is observed due to a 10% reduction of d_c and d_1. Thus, we can deduce that due to the error in fabrication, our sensor performance will not differ by more than 3% of the stated values. The changes found in CL, RW, WS, and AS during the FT analysis are displayed in Table 8.4.

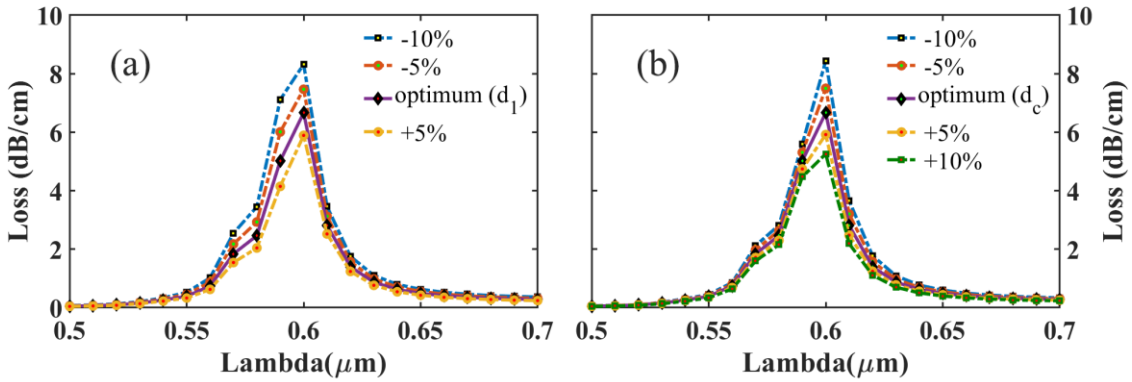

Figure 8.12: CL spectrum at analyte RI 1.37 with a variation of ±5% and ±10% in (a) parameter d_1, (b) parameter d_c

Table 8.4 Fabrication Tolerance Analysis of proposed sensor-3 at analyte RI 1.37

Change in dimension	Variation of d_1				Variation of d_c			
	CL (dB/cm)	RW (nm)	AS (RIU^{-1})	% change in AS	CL (dB/cm)	RW (nm)	AS (RIU^{-1})	% change in AS
-10%	8.322	600	789.234	1.34%	8.437	600	789.876	1.26%
-5%	7.467	600	795.877	0.51%	7.499	600	797.235	0.34%
0%	6.663	600	799.921	0%	6.663	600	799.921	0%
+5%	5.891	600	796.726	0.40%	5.918	600	798.720	0.15%
+10%	-	-	-	-	5.257	600	794.364	0.69%

8.4.6 Temperature and Strain Response Investigation

Till now, we have investigated the sensor characteristics at constant temperature and zero strain. However, it is necessary to study the sensor behavior when the temperature is not constant and when the sensor is undergoing any strain. The temperature and strain analysis will help us determine whether the sensor can be utilized at different temperatures and strains.

The temperature response is essential since the environment temperature may not be constant while the sensor is being used. So it is necessary to know the amount of deviation in the sensor performance due to the temperature variation. To investigate the temperature response, we have used ethanol as the temperature-sensitive analyte. The melting and boiling points of Ethanol are -114.1˚C and 78.37 ˚C. The environmental temperature also varies in this range. In between the melting point and boiling point, the RI of ethanol varies from 1.403 to 1.343, according to equation 5.7. This RI range is almost identical to the sensing range of our sensor. Hence, we select ethanol as the analyte. The

CL curves of the sensor for temperatures -70˚C to 70˚C are shown in figure 8.13 (a). It can be visualized from figure 8.13 (a) that the RW shifts to the left as the temperature is increased. The RW as a function of temperature is plotted in figure 8.13 (b). Figure 8.13 (b) also depicts the linear fitting curve of RW, which has an R^2 value of 0.96923 and a slope of -0.75. The fitting curve's high linearity response indicates that the RW changes almost linearly as the temperature is varied. The slope of the curve depicts that the sensitivity (temperature) of our sensor is 0.75 nm/˚C. The sensor's resolution (temperature) is found to be 1.33×10^{-1} ˚C, assuming $\partial\lambda_{min}$ = 0.1 nm in equation 5.16.

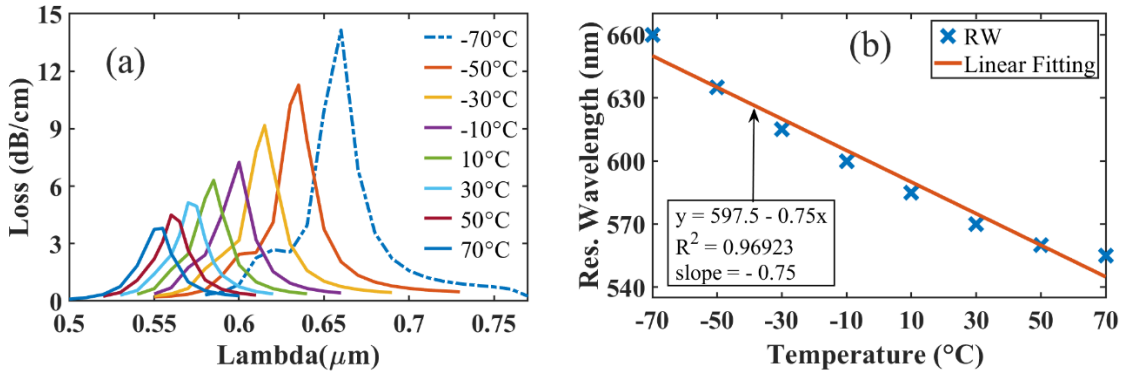

Figure 8.13: (a) CL spectrum of ethanol analyte for temperature variation from -70˚C to 70˚C, (b) plotting of RW with varying temperature

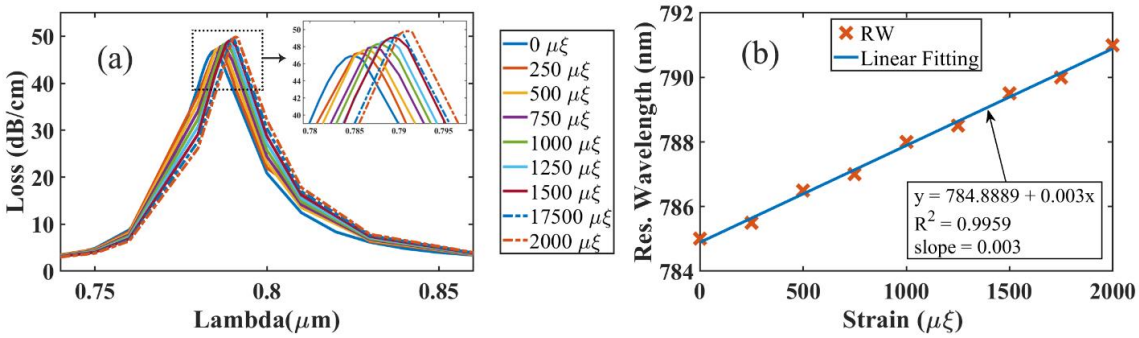

Figure 8.14: (a) CL spectrum for strain variation from 0 με to 2000 με at analyte RI 1.41, (b) plotting of RW with varying strain

Strain response analysis is needed because the flow of analyte around the sensor will generate a force on the sensor, which in terms will engender strain. Therefore, the sensor performance may deviate from the estimated performance. With an increase of strain, the RI of the silica decreases while the RI of air remains constant [121]. Moreover, the strain applied to the sensor does not affect the analyte RI. Therefore, any value of analyte RI can be chosen. We have selected the analyte RI as 1.41 for our strain analysis

since our sensor exhibited maximum AS at that analyte RI value. For constant analyte RI of 1.41, the CL of the sensor for different values of strain in the range of 0-2000 με is illustrated in figure 8.14 (a). With the increase of the strain, the RW shifts to the right. The RW for different strains and their linear fitting curve is manifested in figure 8.14 (b). It is realizable from figure 8.14 that the sensor performance deviates linearly along with the increased strain. The strain sensitivity of our sensor is found to be 0.003 nm/με or 3 pm/με. This indicates that the RW will deviate by an amount of 3 pm (0.003 nm) when the strain is increased by 1 με. The deviation of RW due to the strain alteration is negligible. Therefore, we can conclude that our sensor performance can withstand any strain generated due to the analyte flow.

Our sensor shows a splendid performance compared to other sensors even after considering the downgrading of sensitivity because of fabrication limitation. Moreover, our sensor performance deviates insignificantly due to the temperature and strain variation. The mechanism behind this outstanding performance is the prudent plasmonic material selection and the strategic positioning of air holes in the core. The light is appropriately guided towards the metal layer to create a robust plasmonic effect, and thus upgraded sensing performance is attained in terms of AS, WS, resolution, birefringence, and FOM.

8.5 Conclusion

To recapitulate, we lodge a novel SPR-PCF biosensor with high sensitivity and a fabrication-friendly model that can be contrived through the Stack-and-Draw method. The clustered arrangement of the circular-shaped air cavities in the cladding sector paves the way towards a better plasmonic effect. All the parameters of the fiber have been regulated to achieve the best sensing performance. Our proposed biosensor paraded a maximum amplitude sensitivity of 5060 RIU^{-1} and a wavelength sensitivity of 41500 nm/RIU along with a maximum sensor resolution of 2.41×10^{-6} for wavelength and 1.98×10^{-6} for amplitude. Additionally, our sensor shows a max FOM of 1068.7 and a birefringence of 1.568×10^{-3}. Moreover, a 10% change in the parameters degrades the performance by not more than 3%. The sensor can be utilized at any temperature and under any amount of strain. This sensor promises a great deal of advancement in sensing applications and medical diagnostics for its feasibility in design and high performance regarding sensitivity. In the upcoming chapter, we will discuss a highly sensitive sensor and compare its performance for two different plasmonic materials, gold and AZO.

Chapter 9

Proposed Design-4: Performance Analysis of a Biosensor Employing Gold/AZO

9.1 Introduction

We present a simple, unique, and highly sensitive surface plasmon resonance (SPR) based photonic crystal fiber (PCF) biosensor in this chapter. Besides having very high sensitivity, our proposed sensor is also fabrication friendly. The sensors of the previous chapters utilized gold as the plasmonic material. For the sensor of this chapter, gold (Au) or AZO (aluminium doped zinc oxide) can be utilized to create excitation between the two modes (core and plasmonic). We have tried to vary different parameters of the PCF, and we observed in simulation results a very high amplitude sensitivity of 4358.09 RIU^{-1}, the maximum wavelength sensitivity of 21000 nm/RIU, a high figure of merits of 729 with a sensor resolution of 4.76×10^{-6} RIU and 2.29×10^{-6} RIU for wavelength and amplitude respectively when gold was utilized as the plasmonic material. Replacing gold by AZO resulted in the corresponding values of 3908 RIU^{-1}, 1700 nm/RIU, 792, 5.88×10^{-5} RIU, and 2.56×10^{-6} RIU. Analyte refractive index ranges between 1.33-1.42 for gold and 1.31-1.39 for AZO. We believe the high performance of our proposed SPR based PCF biosensor in terms of sensitivity will bring a promising advancement in the field of unknown analytes detection and biological organic chemicals.

9.2 Structural Design and Numerical Analysis

The performance evaluation has been done using the Finite Element Method. The physics-controlled mesh having a total of 153575 degrees of freedom with fine element size has been used here in order to get the maximum precision in the simulations where the overall structure consists of 21922 numbers of elements with minimum element quality of 0.3965, average element quality of 0.8072, an element area ratio of 0.001044, and mesh area of 152.6 μm^2.

In figure 9.1, we can see that a perfectly matched layer (PML) is applied so that it soaks up outgoing waves without reflecting any wave to the bounded domain. Below the PML layer is the unknown analyte layer, which is to be detected. Just beneath the analyte layer, chemically

stable and non-reactive gold (Au) or AZO (2% wt. of Al in ZnO) can be placed as the plasmonic layer. The fiber material used in this design is chosen to be silica (SiO_2).

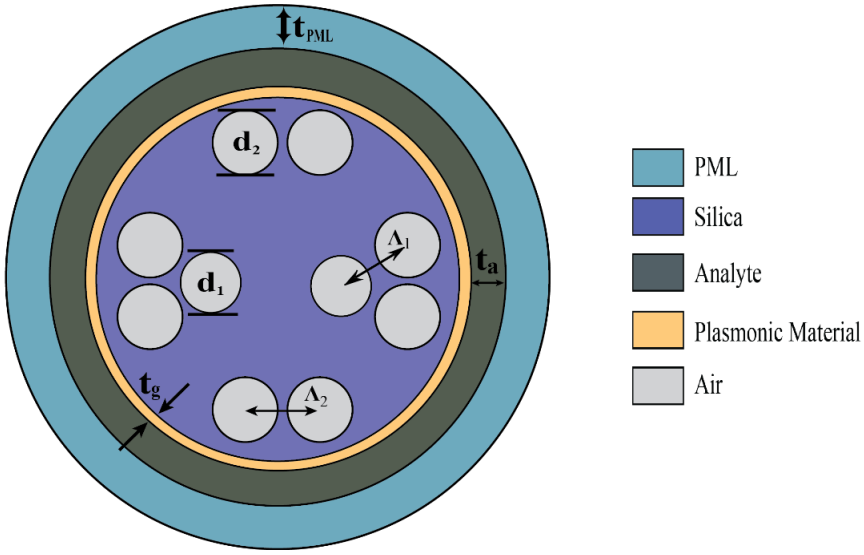

Figure 9.1: Cross-sectional view of our suggested circular-shaped PCF biosensor

As we can see in the figure, there are air holes of two different sizes in this structure. They are circular air holes with diameters d_1 and d_2, which are set to 1.60 μm and 1.66 μm, respectively. The air holes are arranged symmetrically inside the fiber to create a plasmonic effect by deflecting the EM wave from the center towards the metal. Here, the center-to-center distance between the two adjoining larger air holes is denoted by Λ_2, and that between the large and small air holes is Λ_1. Plasmonic layer thickness is represented by t_g. The numerical values of Λ_1, Λ_2, and t_g are 1.803 μm, 2 μm, and 25 nm, respectively.

9.3 Sensor Performance Analysis

9.3.1 Guiding Properties and Dispersion Characteristics.

When light travels through the core, some of it goes through the cladding region, and it is called the evanescent field. Interaction between this field and metal surface generates surface plasmon wave (SPW). Matching of the frequencies between the two modes, core mode and surface plasmon polariton (SPP) mode, will result in an explicit confinement loss peak [7]. A significant change in the loss characteristics occurs due to any small change of the liquid analyte. Detection of an unknown analyte is possible with the usage of either the shift of resonance peak or the loss variations. The propagation properties

independent of polarization are ensured by applying a gold or AZO (2% wt) coating outside the PCF. Our suggested biosensor supports fundamental mode and some higher-order modes also. Further investigation in this chapter is done considering the fundamental mode [105]. Note that we will start our investigation with gold (Au) being the plasmonic material. Later, we will analyze the sensor performance using AZO (2% wt) and compare the performances for both materials.

For our proposed PCF, the coupling between the core and SPP modes for the y-polarized mode is stronger than the coupling for the x-polarized mode. A stronger coupling means that the evanescent field can interact with the outer sensing layer with ease resulting in accurate detection of unknown analytes.

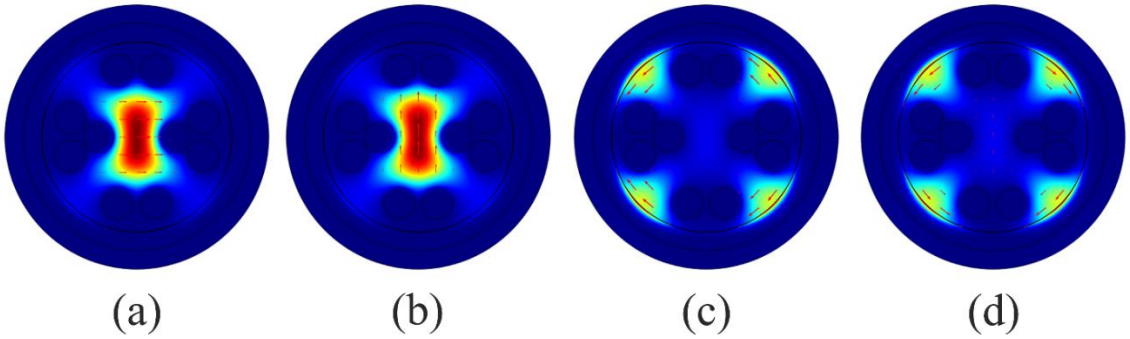

Figure 9.2: Fundamental mode field profile of (a) x-polarized fundamental core mode, (b) y-polarized fundamental core mode, (c) x-polarized SPP mode, (d) y-polarized SPP mode

The dispersion relation between SPP and core mode with analyte RI n_a = 1.36 is displayed in figure 9.3. Simulation software COMSOL 5.3a provided the effective refractive index of the two modes for various operating wavelengths. The real values of the effective refractive indices were plotted as a function of wavelength. This plotting gave the dispersion curves of the two modes (core and SPP).

The wavelength at which the n_{eff} of SPP and core mode intersects with one another is called resonance wavelength (RW), and the intersection is known as phase matching. From figure 9.3, we can see that 0.655 μm is the resonance wavelength. At this resonance wavelength, maximum energy is transferred from the core-guided mode to the SPP mode. As a result, a sharp peak occurs in the CL. We can see in figure 9.3 that higher loss occurs in the y-polarized core mode. Robust interaction between the evanescent field and the SPP mode is obtained when CL is higher. Moreover, this improves the sensing performance prominently.

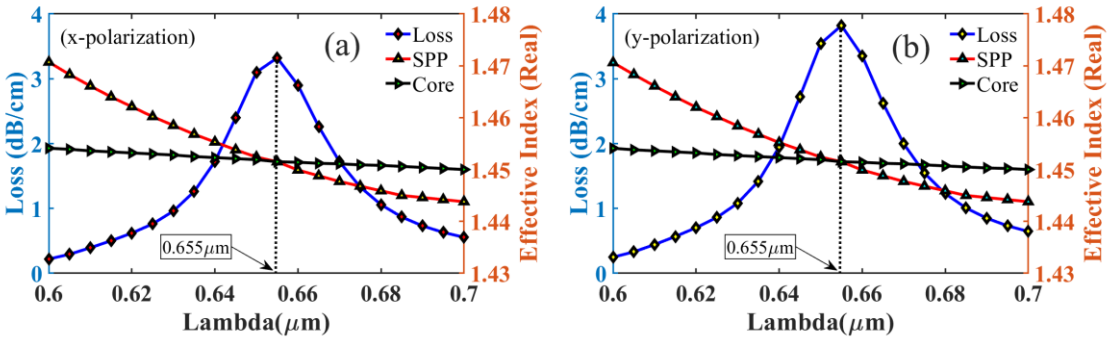

Figure 9.3: Dispersion relation between SPP and core mode at n_a = 1.36 for (a) x-pol; (b) y-pol

Sensor performance can be considered as a function of all the parameters of a PCF. Moreover, smooth interaction between the evanescent field and the plasmonic film depends on these parameters. Thus, these parameters must be selected carefully. These parameters include plasmonic film thickness (t_g), analyte layer thickness (t_a), PML layer thickness (t_{PML}), air hole diameters (d_1, d_2). While optimizing these parameters, we measured the CL, WS, and AS for different values of any particular parameter. The optimal value for any particular parameter was selected depending on CL, AS, and WS values. Initially, we used the following design parameters t_g = 40 nm, t_a = 0.97 µm, t_{PML} = 0.98 µm, d_1 = 1.60 µm, d_2 = 1.90 µm, and optimized them one by one. During the entire optimization process, we have used Au as the plasmonic material.

9.3.2 Gold Layer Thickness Optimization

The plasmonic film thickness, which is denoted by t_g, influences the sensor performance greatly. We kept other parameters constant and modified t_g. Loss depth variation with the change of t_g for n_a = 1.36 and n_a = 1.37 in x-polarization and y-polarization is plotted in figure 9.4 (a) and 9.4 (b), respectively. The AS variation with the change of t_g for n_a = 1.36 in x-polarization and y-polarization mode is plotted in figure 9.4 (c) and 9.4 (d), respectively. Figure 9.4 indicates that CL decreases, and AS increases with the decrease of t_g and shifts the resonance peak towards shorter wavelengths. Gold has high damping loss, and hence the reduction of gold layer thickness results in lower CL. Moreover, a thinner gold layer makes the interaction between the evanescent field and analyte layer easier, and as a result, higher sensitivity is achieved. However, AS gets reduced for an extremely thin gold layer (20 nm) because of the skin depth restriction of

the surface plasmons [83]. We obtained AS of 323.37 RIU^{-1}, 489.09 RIU^{-1}, and 450.71 RIU^{-1} for thickness 20 nm, 25 nm, and 30 nm, respectively, for x-polarization. For y-polarization, the AS values were 326.44 RIU^{-1}, 492.65 RIU^{-1}, and 454.35 RIU^{-1}, respectively. At 25 nm, we obtained the maximum AS, which is 489.09 RIU^{-1} for x-polarization and 492.65 RIU^{-1} for y-polarization. Thus, 25 nm was selected as the optimum value of t_g for further analysis.

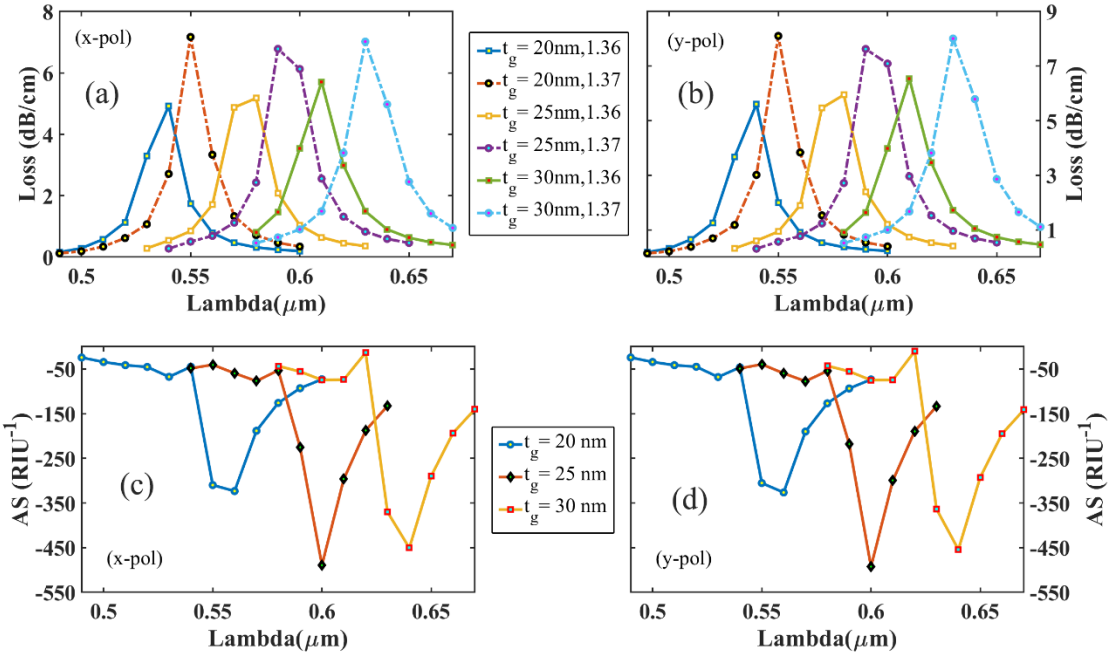

Figure 9.4: CL curves for t_g = 20 nm, 25 nm, 30 nm at RI of 1.36 and 1.37 for (a) x-polarization, (b) y-polarization and AS curves for t_g = 20 nm, 25 nm, 30 nm at RI of 1.36 for (c) x-polarization, (d) y-polarization

9.3.3 Analyte Layer Thickness Optimization

Considering the sensor at the optimum plasmonic film thickness, we then optimize the analyte thickness t_a. First, we increase t_a from 0.97 μm to 1.00 μm. As we increased t_a, the AS of the sensor decreased. So we decrease t_a to 0.94 μm. The reduction of t_a resulted in a minor improvement of the AS. As the change in AS due to the change in t_a is negligible, we decided to keep t_a unchanged. So we choose the analyte layer thickness t_a to be 0.97 μm. It is mention-worthy that if we keep decreasing t_a, AS keeps increasing, and at t_a = 0.30 μm, maximum AS can be obtained. However, this massive shrinkage of the analyte layer results in leakage of EM waves into the PML layer. Moreover, if we proceed with t_a = 0.30 μm, the CL and AS curves show double peaks, creating complexity in further analysis. Thus, we do not reduce analyte layer thickness to that extend and proceed with

0.97 µm. Loss depth variations with the change of t_a for n_a = 1.36 and n_a = 1.37 in x-polarization and y-polarization modes are plotted in figure 9.5 (a) and 9.5 (b), respectively. The amplitude sensitivity changes with the change of t_a for n_a = 1.36 in x-polarization and y-polarization modes are illustrated in figure 9.5 (c) and 9.5 (d), respectively. All the curves overlapped with each other as the CL and AS are very close to each other. Thus only one curve could be seen. Nevertheless, all the curves could be distinguished separately after zooming to a certain extent. In figure 9.5, the zoomed view of a portion of both the CL and AS curves are shown.

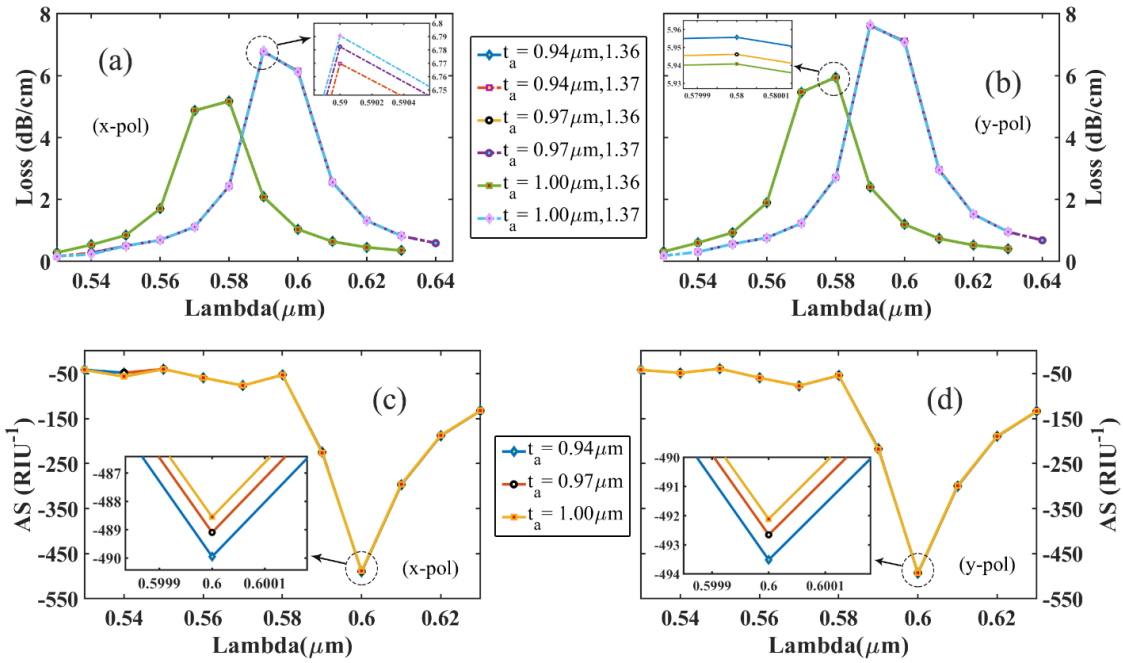

Figure 9.5: CL curves for t_a = 0.94 µm, 0.97 µm, 1.00 µm at RI of 1.36 and 1.37 for (a) x-polarization, (b) y-polarization and AS curves for t_a = 0.94 µm, 0.97 µm, 1.00 µm at RI of 1.36 for (c) x-polarization, (d) y-polarization

9.3.4 PML Layer Thickness Optimization

After finding the optimum value for t_a, now we optimize PML layer thickness, which is denoted by t_{PML}. While doing so, we keep t_a fixed at 0.97 µm. For different values of the PML layer thickness, the CL and AS of our sensor is illustrated in figure 9.6. The values of AS obtained by setting t_{PML} to 0.96 µm, 0.98 µm, and 1.00 µm, are 488.81 RIU^{-1}, 489.08 RIU^{-1}, and 489.09 RIU^{-1}, respectively for x-polarization and 492.36 RIU^{-1}, 492.62 RIU^{-1}, and 492.65 RIU^{-1}, respectively for y-polarization. We can see that AS does not

change significantly with the change of t_{PML}. So we resume our investigation with the initial value of t_{PML}, which is 0.98 µm.

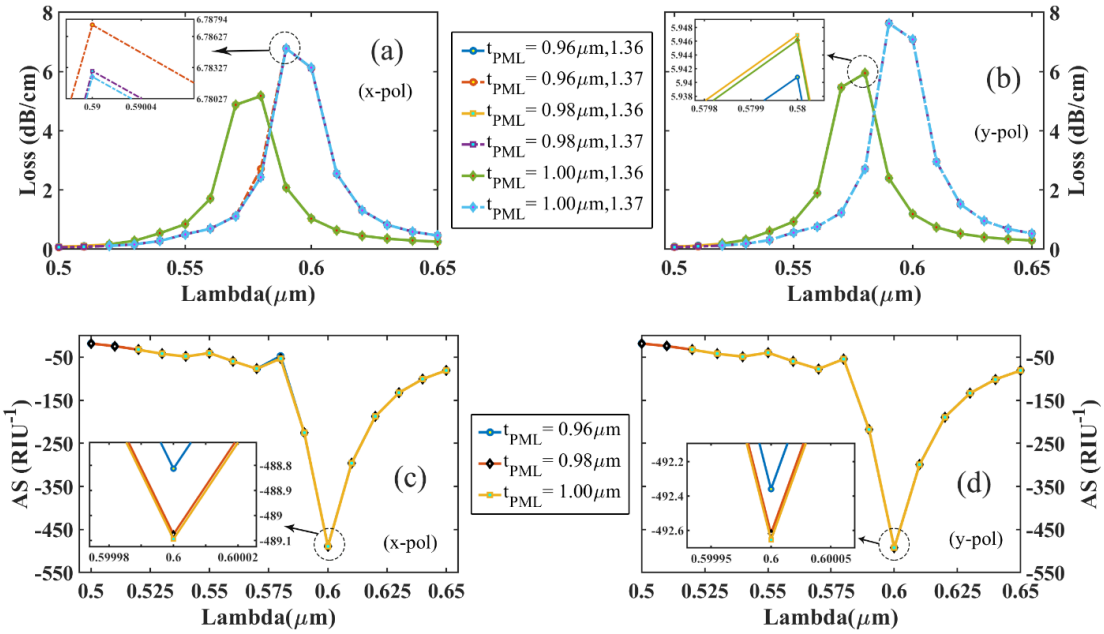

Figure 9.6: CL curves for t_{PML} = 0.96 µm, 0.98 µm, 1.00 µm at RI of 1.36 and 1.37 for (a) x-polarization, (b) y-polarization and AS curves for t_{PML} = 0.96 µm, 0.98 µm, 1.00 µm at RI of 1.36 for (c) x-polarization, (d) y-polarization

9.3.5 Air Hole Diameters Optimization

Until now, we have optimized plasmonic layer thickness, analyte layer thickness, and PML layer thickness. Now we will change the diameters of the core air holes to find out their optimum values. We begin with varying d_2 while all other parameters are kept unchanged. The CL and AS characteristics curves of the sensor for d_2 = 1.62 µm, 1.66 µm, and 1.70 µm are shown in figure 9.7. We can observe that the CL decreases as d_2 is increased. This incident occurs since larger air holes help in better confinement of the EM waves in the fiber core. However, the increment of d_2 reduces the channel width between the core and the cladding. Moreover, when d_2 is set to a value higher than 1.66 µm, the EM waves cannot interact with the analyte layer appropriately due to very narrow channels. As a result, AS gets reduced. Enough channel width should be allowed for proper interaction and to obtain better sensitivity. Figure 9.7 (c) and (d) shows that the maximum AS is obtained for d_2 = 1.66 µm. Thus, 1.66 µm is selected as the optimized value of d_2.

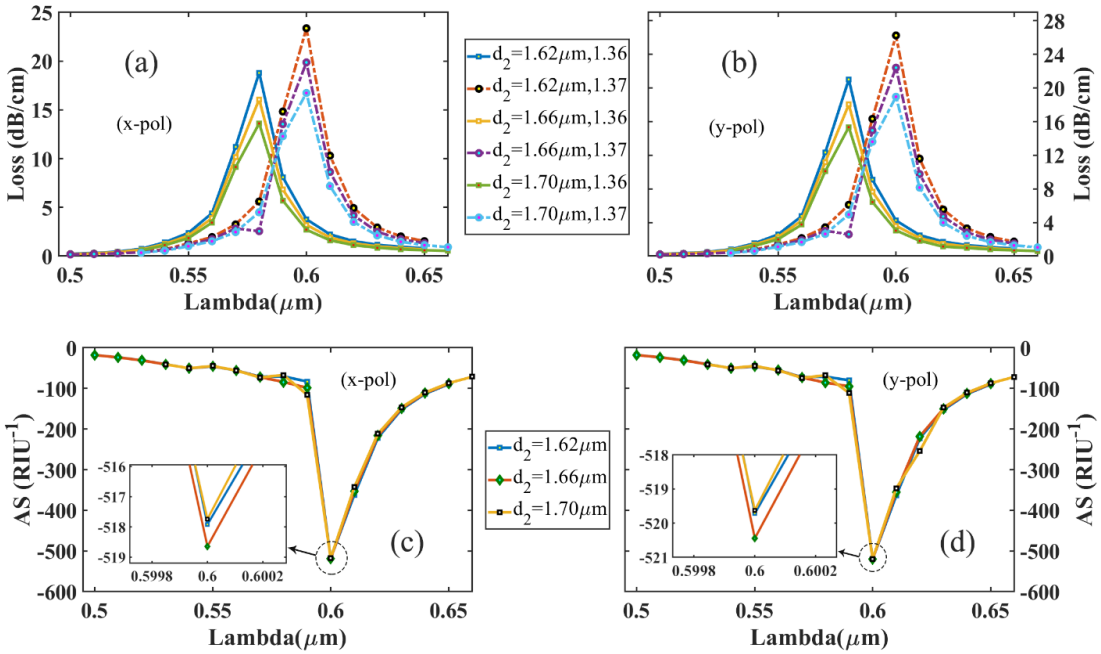

Figure 9.7: CL curves of the suggested sensor for d_2=1.62 µm, 1.66 µm, 1.70 µm at RI of 1.36 and 1.37 for (a) x-polarization, (b) y-polarization and AS for d_2=1.62 µm, 1.66 µm, 1.70 µm at RI of 1.36 for (c) x-polarization, (d) y-polarization

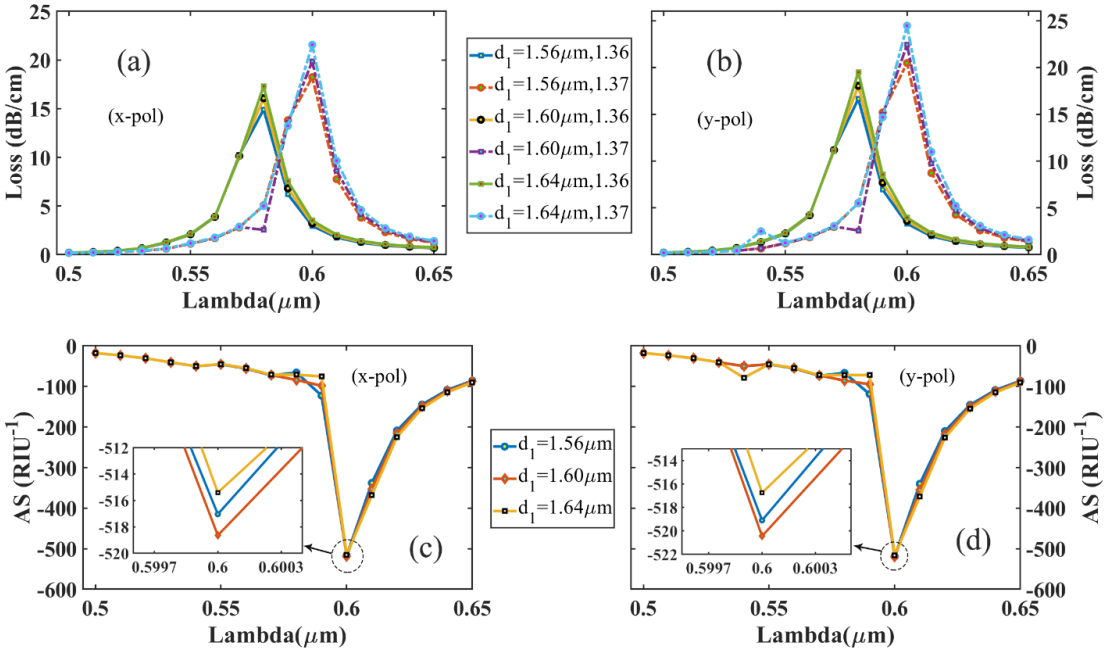

Figure 9.8: CL curves of the suggested sensor for d_1=1.56 µm, 1.60 µm, 1.64 µm at RI of 1.36 and 1.37 for (a) x-polarization, (b) y-polarization and AS curves for d_1=1.56 µm, 1.60 µm, 1.64 µm at RI of 1.36 for (c) x-polarization, (d) y-polarization

After finding the optimized value of d_2, we then optimize d_1. While optimizing d_2, the value of d_1 was kept fixed at 1.60 μm. For d_1= 1.60 μm, AS is 518.644 RIU^{-1} and 520.443 RIU^{-1} for x and y polarization, respectively. Now we increase the value of d_1 to 1.64 μm. For this value of d_1, AS decreases to 515.403 RIU^{-1} for x-polarization and 516.75 RIU^{-1} for y-polarization. So we decrease d_1 to 1.56 μm and find out AS to be 517.04 RIU^{-1} for x-polarization and 519.1 RIU^{-1} for y-polarization. The characteristic curves of CL and AS for all these values of d_1 are plotted in figure 9.8. We can see from figure 9.8 that the maximum AS is obtained at d_1= 1.60 μm for both the polarization modes. Thus we select 1.60 μm as the optimum value for d_1.

9.3.6 Sensor Performance for Gold at Optimized Parameters

As we have found the optimum values of our proposed sensor's geometrical parameters, now we will observe the effect of changing the analyte RI when Au is the plasmonic material. We focused on the RI range from 1.33 to 1.42 in this analysis. Note that previously reported SPR sensors have the same RI range [71], [83], [127], [84], [85], [94], [122]–[126].

Figure 9.9 illustrates the variation in CL and AS for different values of the analyte RI when gold is used. These values were calculated using equations 5.8 and 5.9, respectively. The values of resonance wavelengths are shifted from 0.54 μm to 0.55 μm, 0.55 μm to 0.56 μm, 0.56 μm to 0.58 μm, 0.58 μm to 0.60 μm, 0.60 μm to 0.62 μm, 0.62 μm to 0.66 μm, 0.66 μm to 0.71 μm, 0.71 μm to 0.81 μm, and 0.81 μm to 1.02 μm with the change of analyte RI from 1.33 to 1.34, 1.34 to 1.35, 1.35 to 1.36, 1.36 to 1.37, 1.37 to 1.38, 1.38 to 1.39, 1.39 to 1.40, 1.40 to 1.41, and 1.41 to 1.42 respectively with the optimum parameters.

From figure 9.9, we observed that AS changes with the change of analyte n_a. It can be seen that the amplitude sensitivities are 201.29 RIU^{-1}, 269.43 RIU^{-1}, 379.75 RIU^{-1}, 518.64 RIU^{-1}, 529.58 RIU^{-1}, 1069.26 RIU^{-1}, 1758.12 RIU^{-1}, 4358.09 RIU^{-1}, 112.06 RIU^{-1} for x-polarization and 200.74 RIU^{-1}, 270.64 RIU^{-1}, 380.25 RIU^{-1}, 520.44 RIU^{-1}, 523.14 RIU^{-1}, 1082.27 RIU^{-1}, 1805.42 RIU^{-1}, 3871.27 RIU^{-1}, 101.67 RIU^{-1} for y-polarization for n_a = 1.33, 1.34, 1.35, 1.36, 1.37, 1.38, 1.39, 1.40 and 1.41. We achieved the highest AS of 4358.09 RIU^{-1} for x-polarization and 3871.27 RIU^{-1} for y-polarization with analyte n_a = 1.40. These values are higher than the recent article values shown in Table 9.3.

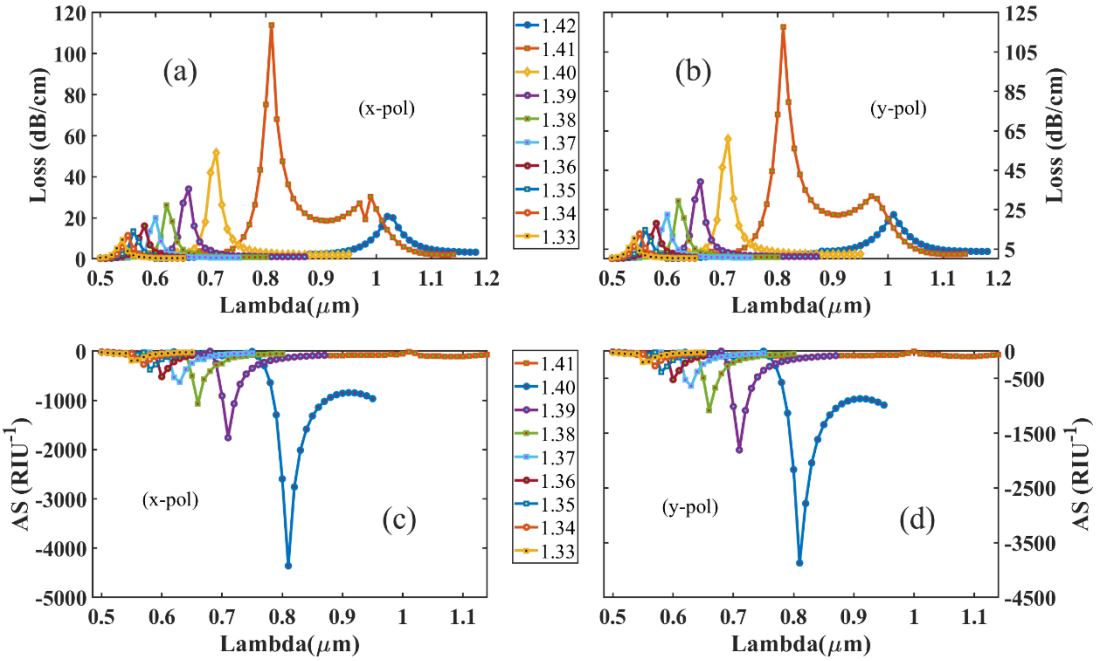

Figure 9.9: CL curves for plasmonic material Au in the RI range from 1.33–1.42 in (a) x-polarization and (b) y-polarization and AS curves in the RI range from 1.33–1.41 in (c) x-polarization and (d) y-polarization; with t_g = 25 nm, t_a = 0.97 µm, t_{PML} = 0.98 µm, d_1 = 1.60 µm, d_2 = 1.66 µm

Now using equation 5.10, we measure the wavelength sensitivities for different values of n_a. We found WS to be 1000 nm/RIU for n_a = 1.33 and 1.34; 2000 nm/RIU for n_a = 1.35, 1.36, and 1.37; 4000 nm/RIU for n_a = 1.38; 5000 nm/RIU for n_a = 1.39; 10000 nm/RIU for n_a = 1.40 for both x- and y-polarization. For n_a = 1.41, WS is 21000 nm/RIU for x-polarization and 20000 nm/RIU for y-polarization. The highest WS obtained in this work is 21000 nm/RIU for x-polarization mode for changing the analyte RI from 1.41–1.42.

The resolution of the sensor is measured using equation 5.11. We found RI resolution 1×10^{-4}, 1×10^{-4}, 5×10^{-5}, 5×10^{-5}, 5×10^{-5}, 2.5×10^{-5}, 2×10^{-5}, 1×10^{-5}, and 4.76×10^{-6}, RIU for analyte RI 1.33, 1.34, 1.35, 1.36, 1.37, 1.38, 1.39, 1.40 and 1.41 respectively assuming $\partial\lambda_{min}$ = 0.1 nm. The highest RI resolution is 4.76×10^{-6} RIU for n_a = 1.41 in x-polarization and 5×10^{-6} RIU for y-polarization.

Having a high linearity response of the regression line makes a sensor exceptional. It shows that the sensor can be implemented having a proportional relationship between resonance wavelength and analyte RI. Figure 9.10 (a) illustrates the 4th order fitting line for our proposed sensor for plasmonic material gold. The fitting curve gives an R^2 value of

0.9991, and it proves that the sensor has high linearity. In the fitting curve equation, x and y indicate the refractive index and the resonance wavelength, respectively.

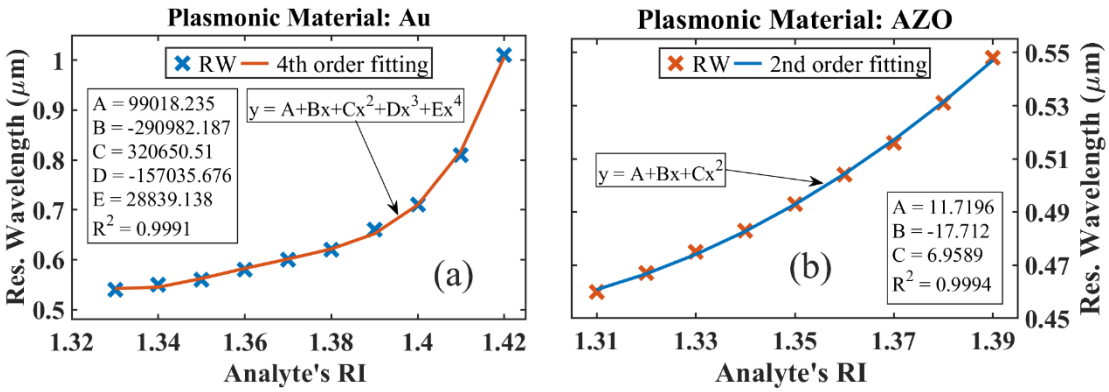

Figure 9.10: Regression lines of the resonance wavelength with the variation of analyte RI for (a) plasmonic material gold; (b) plasmonic material AZO (2% wt)

Table 9.1 Summary of the important parameter values of the proposed gold-coated sensor-4 for different values of RI

RI	Peak wavelength (μm)		Amplitude sensitivity (RIU^{-1})		Wavelength sensitivity (nm/RIU)		Resolution (Wavelength) (RIU)		Full-Width Half Maximum (FWHM)		Figure of Merit (FOM)	
	x	y	x	y	x	y	x	y	x	y	x	y
1.33	0.54	0.54	201.29	200.74	1000	1000	1×10^{-4}	1×10^{-4}	18.8	18.8	53	53
1.34	0.55	0.55	269.43	270.64	1000	1000	1×10^{-4}	1×10^{-4}	18.6	18.6	54	54
1.35	0.56	0.56	379.75	380.25	2000	2000	5×10^{-5}	5×10^{-5}	19.5	19.4	102	103
1.36	0.58	0.58	518.64	520.44	2000	2000	5×10^{-5}	5×10^{-5}	20.2	20.2	99	99
1.37	0.60	0.60	529.58	523.14	2000	2000	5×10^{-5}	5×10^{-5}	21.4	21.1	93	95
1.38	0.62	0.62	1069.26	1082.27	4000	4000	2.5×10^{-5}	2.5×10^{-5}	21.9	21.8	183	184
1.39	0.66	0.66	1758.12	1805.42	5000	5000	2×10^{-5}	2×10^{-5}	22	22.2	227	225
1.40	0.71	0.71	4358.09	3871.27	10000	10000	1×10^{-5}	1×10^{-5}	26	25	384	399
1.41	0.81	0.81	112.06	101.67	21000	20000	4.76×10^{-6}	5×10^{-6}	28.8	32.8	729	609
1.42	1.02	1.01	-	-	-	-	-	-	-	-	-	-

The FOM is a crucial parameter that indicates the overall performance of a sensor. FWHM and FOM for different analytes are shown in Table 9.1. From table 9.1, we can see that FWHM increases with the increase in analyte RI. However, FWHM for our proposed sensor is comparatively very low. Lower FWHM means a higher FOM. The highest FOM of our sensor for x and y polarization were 729 and 609, respectively. This high FOM is also an indication that the sensor performance is improved. It is to be mentioned that a higher FOM indicates a better detection limit [85].

Table 9.1 represents the performance evaluation of our biosensor (when gold is used) on the basis of WS, AS, FOM, resolution for different values of RI. From the table, we can see that maximum AS of 4358.09 RIU^{-1} and 3871.27 RIU^{-1}, maximum WS of 21000 nm/RIU and 20000 nm/RIU, a maximum FOM of 729 and 609, a maximum resolution (wavelength) of 4.76×10^{-6} RIU and 5×10^{-6} RIU, and a maximum sensor resolution (amplitude) of 2.29×10^{-6} RIU and 2.58×10^{-6} RIU are obtained for the x and y polarizations respectively.

9.3.7 Sensor Performance for AZO at Optimized Parameters

We now replace the plasmonic material gold with AZO (2% wt) and estimate the sensor performance at the optimized parameters i.e. t_g = 25 nm, t_a = 0.97 µm, t_{PML} = 0.98 µm, d_1 = 1.60 µm, d_2 = 1.66 µm. Figure 9.11 illustrates the variation in CL and AS for different values of the analyte RI when AZO is used. We can visualize from figure 9.11 that the RI range is now 1.31-1.39 instead of 1.33-1.42. So we can say that AZO based sensors enable us to detect analytes with lower RI. For AZO based sensor, the maximum AS was found to be 3908 RIU^{-1} for x-polarization and 3047 RIU^{-1} for y-polarization at analyte RI 1.37. These AS values correspond to the maximum resolution (amplitude) of 2.56×10^{-6} RIU and 3.28×10^{-6} RIU for x and y polarizations. These AS and resolution (amplitude) values are considerably high. However, they are a bit lower than the gold-based sensor. The maximum WS of the AZO based sensor is 1600 nm/RIU (x-polarization) and 1700 nm/RIU (y-polarization), which are very low compared to the gold-based sensor. The resolution (wavelength) for AZO based sensor is estimated to be 6.25×10^{-5} RIU and 5.88×10^{-5} RIU for x- and y-polarizations. It is clear that AZO does not provide much RW shift. However, it shows very sharp CL peaks, which results in very low FWHM. Hence, the FOM values of AZO based sensor is higher than that of the gold-based sensor. Our sensor exhibits maximum FOM values of 792 (x-pol) and 685 (y-pol) when gold is replaced

by AZO. Additionally, the AZO-based sensor's linearity response is much improved than that of the gold-based sensor. Figure 9.10 (b) depicts the 2nd order fitting line of RW as a function of analyte RI, and it is understandable from the figure that the fitting line of AZO coated sensor shows an improved R^2 value (0.9994) at a lower order.

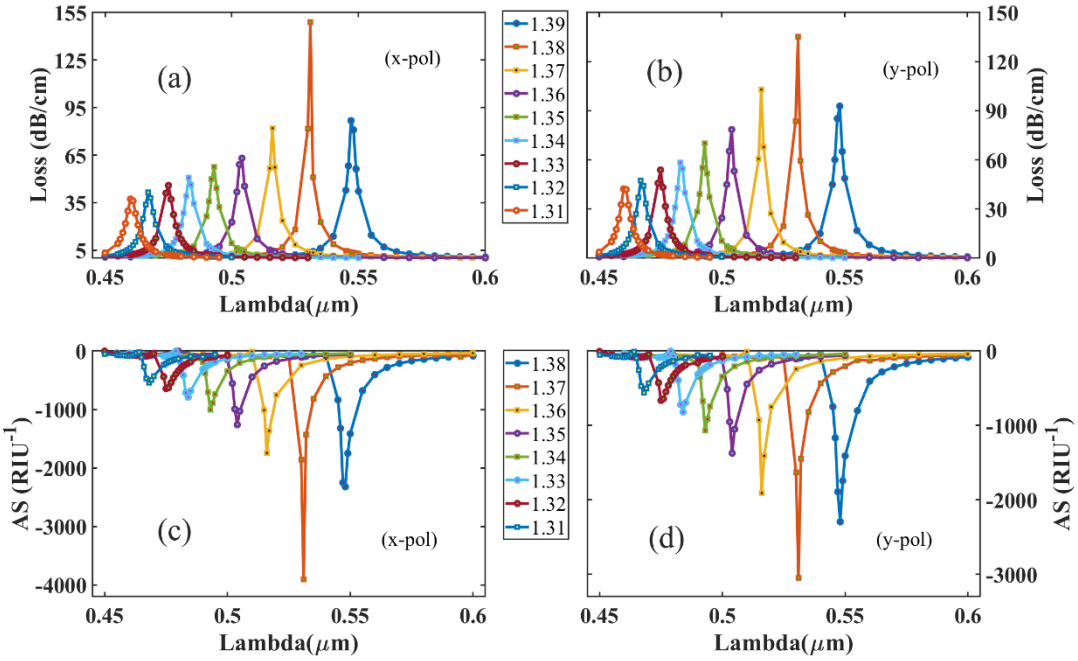

Figure 9.11: CL curves for plasmonic material AZO in the RI range from 1.31–1.39 in (a) x-polarization and (b) y-polarization and AS curves in the RI range from 1.31–1.39 in (c) x-polarization and (d) y-polarization; with t_g = 25 nm, t_a = 0.97 µm, t_{PML} = 0.98 µm, d_1 = 1.60 µm, d_2 = 1.66 µm

Table 9.2 Summary of the important parameter values of the proposed AZO coated sensor-4 for different values of RI

RI	Peak wavelength (µm)		Amplitude sensitivity (RIU^{-1})		Wavelength sensitivity (nm/RIU)		Resolution (Wavelength) (RIU)		Full-Width Half Maximum (FWHM)		Figure of Merit (FOM)	
	x	y	x	y	x	y	x	y	x	y	x	y
1.31	0.46	0.46	546	560	700	700	1.43×10^{-4}	1.43×10^{-4}	5.9	5.8	118	120
1.32	0.467	0.467	642	664	800	800	1.25×10^{-4}	1.25×10^{-4}	5.67	5.51	141	145
1.33	0.475	0.475	789	820	800	800	1.25×10^{-4}	1.25×10^{-4}	5.5	5.18	145	154
1.34	0.483	0.483	1000	1069	1000	1000	1.0×10^{-4}	1.0×10^{-4}	5.42	5.19	184	192
1.35	0.493	0.493	1259	1372	1100	1100	9.09×10^{-5}	9.09×10^{-5}	5.16	4.59	213	239
1.36	0.504	0.504	1748	1912	1200	1200	8.33×10^{-5}	8.33×10^{-5}	5.1	4.41	235	272
1.37	0.516	0.516	3908	3047	1500	1500	6.67×10^{-5}	6.67×10^{-5}	3.94	3.32	380	451
1.38	0.531	0.531	2321	2294	1600	1700	6.25×10^{-5}	5.88×10^{-5}	2.02	2.48	792	685
1.39	0.547	0.548	-	-	-	-	-	-	-	-	-	-

Table 9.3 Comparison of the performance of the proposed sensor-4 with previously published sensors

PCF-SPR Sensor			Maximum Wavelength Sensitivity (nm/RIU)	Sensor Resolution (Wavelength) (RIU)	Maximum Amplitude Sensitivity (RIU^{-1})	Sensor Resolution (Amplitude) (RIU)	FOM
Ref. [20]			5000	2.00×10^{-5}	167	5.98×10^{-5}	-
Ref. [110]			12,000	8.33×10^{-6}	2044	4.89×10^{-6}	-
Ref. [77]			4200	2.38×10^{-5}	300	3.33×10^{-5}	478.3
Ref. [84]			17000	5.88×10^{-6}	4596	2.18×10^{-6}	-
Ref. [122]			15180	5.68×10^{-6}	498	2.01×10^{-5}	-
Ref. [85]			25000	4.00×10^{-6}	1411	7.09×10^{-6}	502
Ref. [124]			4600	2.17×10^{-5}	420.4	2.38×10^{-5}	-
Ref. [128]			20000	5.00×10^{-6}	1054	9.49×10^{-6}	-
Ref. [129]			51000	1.96×10^{-6}	1872	5.34×10^{-6}	566
Ref. [22]			11000	7.00×10^{-6}	1420	7.04×10^{-6}	407
Proposed Design	Au coated	x-pol	21000	4.76×10^{-6}	4358.09	2.29×10^{-6}	729
		y-pol	20000	5.00×10^{-6}	3871	2.58×10^{-6}	609
	AZO coated	x-pol	1600	6.25×10^{-5}	3908	2.56×10^{-6}	792
		y-pol	1700	5.88×10^{-5}	3047	3.28×10^{-6}	685

Table 9.2 shows the performance evaluation of our biosensor (when AZO is used) on the basis of WS, AS, FOM, resolution for different values of RI. From the above analysis and comparison between the gold-coated sensor and AZO coated sensor, we can say that gold and AZO has their advantages and disadvantages as plasmonic material. The gold-based sensor can be used to detect analytes with higher RI, and AZO can be implemented for analytes with comparatively lower RI. Depending on the sensing requirement, plasmonic material can be chosen as either gold or AZO since both of them exhibits very high AS, resolution and FOM.

Table 9.3 shows a detailed performance comparison between our sensor and the prior sensors. We can see that in terms of WS, AS, resolution, FOM, etc., our proposed sensor is better than most of the previous gold-based and AZO based sensors.

9.4 Conclusion

A very simple circular-shaped SPR based PCF biosensor is proposed that has a high sensing capacity. We have optimized all the functional parameters to achieve maximum performance on the basis of AS, WS, resolution, etc. The finite element method (FEM) is utilized to perform all the numerical calculations. Arrangement of air holes is made in a manner so that these can guide the evanescent field to interact actively with the metal. A perfectly matched layer is formed to restrain electromagnetic waves from leaking out of the fiber. The proposed sensor offers a maximum FOM of 729, a maximum AS of 4358.09 RIU^{-1} with a sensor resolution of 2.29×10^{-6} RIU, a maximum WS of 21000 nm/RIU, and a sensor resolution of 4.76×10^{-6} RIU for the plasmonic material gold. For plasmonic material AZO (2% wt), the corresponding values are 792, 3908 RIU^{-1}, 2.56×10^{-6} RIU, 1700 nm/RIU, and 5.88×10^{-5} RIU. We have seen very few sensors having a sensitivity and FOM as high as ours, so we firmly believe our PCF will contribute a lot in sensing unknown biological and biochemical analytes. With this chapter, we conclude the discussion on our proposed SPR based PCF biosensors.

Chapter 10

Fabrication

10.1 Introduction

Our designing these SPR sensors aims to reduce the fabrication difficulties and get a high sensitivity with low peak loss. The optical fiber designs with more straightforward fabrication procedures and developed sensing activities should be given importance over the sensors having a complicated fabrication process. Designing SPR sensors have some main mottos. Ease fabrication is one of them. So, the fabrication of surface plasmon resonance sensors has to be as simple as possible and be price-friendly. Usually, the PCF having the desired core structure is fabricated using the Stack and Draw method. After that, the metal layer coating is given using various methods such as Atomic Layer Deposition method, Chemical Vapor Deposition method, etc. These methods are discussed in the next sections of this chapter.

10.2 Stack and Draw Method

This method is one of the easiest ways which has been used for the fabrication of PCFs. For stacking glass rods, tubes, capillaries (different shapes), a macroscopic element of a fiber optic element (i.e., fiber) stack and draw method has been used. This fabrication method has been discussed in detail in the literature [120]. A brief summary of the process is given in this section.

As we can see in figure 10.1, the fabrication procedure of a PCF is shown nicely. The fabrication starts with a fiber preform. Several silica capillary tubes are stacked to make PCF preforms, and the rods are utilized to form the desired air/silica structure. This placement method of preform allows a high level of design flexibility as both the core size and shape as well as the index profile throughout the cladding region can be controlled.

After constructing the desired preform, it is drawn to a fiber in a conventional high-temperature drawing tower, and hair-thin photonic crystal fibers are readily produced in kilometer lengths. Through careful process control, the air holes retain their arrangement through the drawing process, and even fibers with very complex designs and high air filling fractions can be produced.

Finally, a protective jacket is provided to the fibers as a coating which ensures robust handling of the fibers. The final fibers are comparable to standard fiber in both robustness and physical dimensions and can be both striped and cleaved using standard tools.

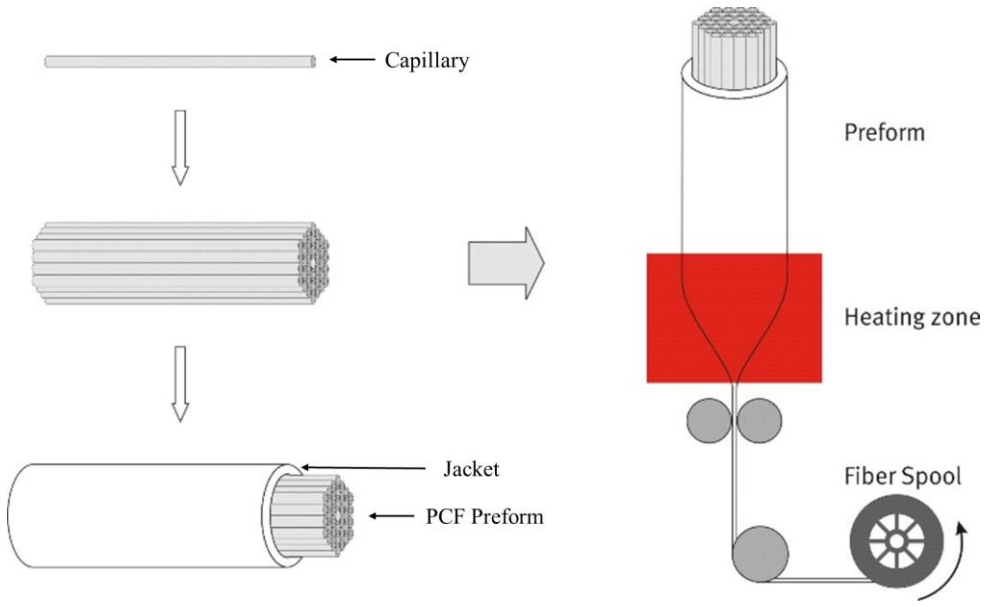

Figure 10.1: Illustration of the stack-and-draw method

10.3 Atomic Layer Deposition Method (ALD)

To achieve thin film growth, atomic layer deposition (ALD) uses a series of two or more surface reactions that are repeated cyclically [130]. This advantage over other deposition methods opens up a wide variety of possibilities. Although ALD was historically used predominantly in the electronic semiconductor industry, with advances in recipe creation, it is now considered for broader applications in energy, climate, and sustainability research. ALD is based on molecular precursors undergoing sequential surface reactions separated by an inert gas purge. The reactants are separated in this manner until the adsorbed species react at the surface in a self-limiting, gas-phase-free process. The ALD method has the ability to precisely monitor the thickness of deposited films at an atomic level by varying the number of deposition cycles. Another important feature of ALD is the self-limiting nature of the surface reactions that occur during deposition, which prevents multilayer growth (i.e. allows control of film thickness) and makes studying surface grafting and/or film growth mechanisms easier [131]. A diagram of the ALD growth cycle is depicted in the figure 10.2.

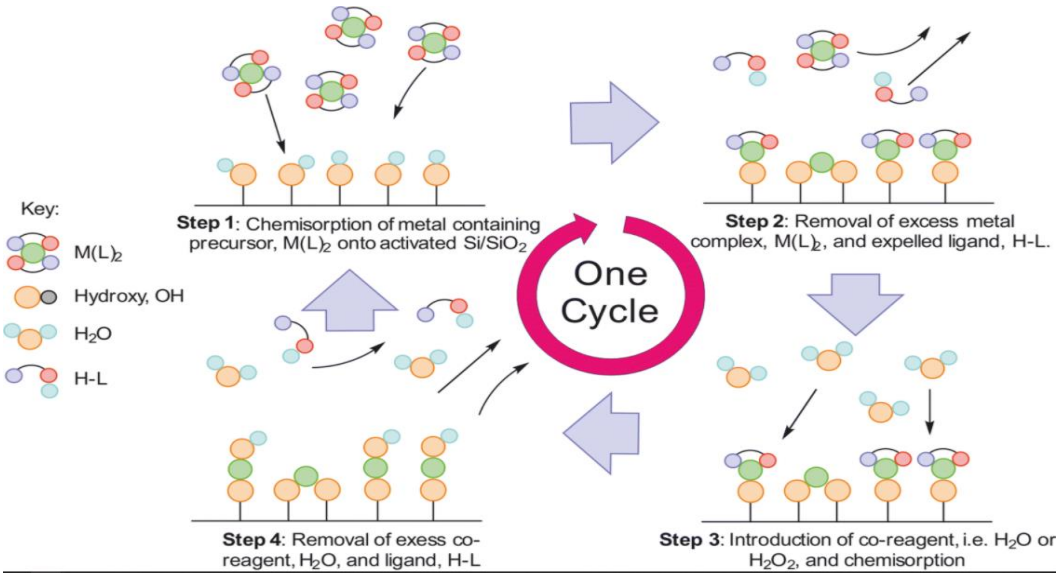

Figure 10.2: A schematic ALD cycle showing the growth cycle of a generic metal oxide

10.4 Chemical Vapor Deposition Technique (CVD)

In the SPR sensor, some roughness will be found on the metal surface. For minimizing roughness, this technique has been employed. Chemical vapor deposition (CVD) is such kind of a method of vacuum deposition that is used to create high-quality, high-efficiency solid materials. In the semiconductor industry, the process is also used to make thin films. CVD is also classified into different operating conditions, physical characteristics of vapor, substrate heating, etc. In this method, a coating is provided on the heated substrate with the help of thermally induced reactions at the substrate surface. During these reactions, reagents are supplied in gaseous form. Such technique is useful in ALD at depositing highly thin layers of material. CVD technique is also used for membrane coating, which is important for water treatment, and as these coatings are quite uniform and thin that they do not need sabot membrane pores.

Chapter 11

Future Work and Conclusion

11.1 Socio-Economic Impact of PCF based SPR Sensors

The PCF-SPR biosensors we have proposed have a significant impact on medical science and research. We can have a look at some of the mentionable uses as follows:

- ✓ We can use them to perform DNA and RNA assays
- ✓ The presence of deadly viruses like dengue can be detected rapidly in blood samples.
- ✓ We can use them for assaying antibody-antigen, bacteria, virus, mRNA, hemoglobin, hormone, protein, etc.
- ✓ To determine the presence of harmful gases such as H_2S from a complex mixture.
- ✓ Different types of tests can be completed within two to ten minutes, so the duration of testing is greatly reduced.
- ✓ Samples of only a few nanograms of molecules are needed, so the overall cost is reduced.

The only alternatives are the commercial instruments that cost tens of thousands of dollars; thus, we can save a lot of money by using them to our advantage.

11.2 Future Work Scope

In almost all of our designs, we have used gold as the plasmonic material and generally used circular air holes. We also used TiO_2 for better adhesion of gold. We generally used silica as the background material. However, in the future, the following advancement in this sector can be done:

- Use of different plasmonic materials such as graphene, AZO, TiN, etc., to search for better sensitivity and better results.
- Although only circular and rectangular air holes were used in the designs of this book, there can be other types of air holes that may give better results, and these can be tested in the future.
- The same designs can be implemented on a D-shaped PCF to investigate the sensor performance.

- Magnetic field strength sensors and strain sensors can be approached.
- Multi-analyte channel-based sensors can be implemented.
- Metal grating-based sensors can be implemented.

11.3 Conclusion

To recapitulate, it can be easily said that biosensors are very important to detect biological and biochemical analytes. Here, we have used the surface plasmon resonance phenomenon to determine the unknown analyte. PCF-based SPR sensors are small in structure, and by altering certain parameters of the PCF, we can control the evanescent field. The cladding region in PCFs has periodic air holes which guide the electromagnetic field, and thus the propagation of light can be controlled by modifying the air hole geometries. Different plasmonic materials are used to enhance the sensitivity of the sensors. The main parameters that determine the effectiveness of a sensor are the maximum amplitude sensitivity and maximum wavelength sensitivity. In this thesis, we have done an elaborate discussion on all the designs we have created, and all of them contribute to the field of biosensing in different ways. We have mentioned in detail four particularly unique SPR biosensor designs, all of them showing excellent sensing performance. All the sensors have a perfectly matched layer (PML) encompassing the fiber, which ensures the absorbance of the scattered evanescent field. We used the full vectorial finite element method (FEM) method of COMSOL Multiphysics simulation software to perform the numerical investigations. All the parameters of the fiber have been regulated to achieve the best sensing performance. These sensors can be utilized at any temperature and under any amount of strain. As the designs are simple and done strategically, it will be easier to practically fabricate them with the existing methods. After optimization of all the performance determining parameters of the fibers, we have found excellent values of amplitude and wavelength sensitivities (AS and WS), confinement loss, birefringence, FOM, etc., as we have seen in the earlier discussions. Lastly, we can say that our designed sensors promise a great deal of advancement in sensing applications and medical diagnostics for their feasibility in design and high-performance regarding sensitivity.

References

[1] D. R. Thevenot, K. Tóth, R. A. Durst, and G. S. Wilson, "Electrochemical Biosensors: Recommended Definitions and Classification," *Pure Appl. Chem.*, vol. 71, no. 12, pp. 2333–2348, Jan. 1999, doi: 10.1351/pac199971122333.

[2] B. K. Paul, K. Ahmed, S. Asaduzzaman, and M. S. Islam, "Folded cladding porous shaped photonic crystal fiber with high sensitivity in optical sensing applications: Design and analysis," *Sens. Bio-Sensing Res.*, vol. 12, pp. 36–42, Feb. 2017, doi: 10.1016/j.sbsr.2016.11.005.

[3] S. Chowdhury *et al.*, "Porous shaped photonic crystal fiber with strong confinement field in sensing applications: Design and analysis," *Sens. Bio-Sensing Res.*, vol. 13, pp. 63–69, 2017, doi: 10.1016/j.sbsr.2017.03.002.

[4] S. Sen, S. Chowdhury, K. Ahmed, and S. Asaduzzaman, "Design of a porous cored hexagonal photonic crystal fiber based optical sensor with high relative sensitivity for lower operating wavelength," *Photonic Sensors*, vol. 7, no. 1, pp. 55–65, 2017, doi: 10.1007/s13320-016-0384-y.

[5] I. Islam *et al.*, "Highly birefringent single mode spiral shape photonic crystal fiber based sensor for gas sensing applications," *Sens. Bio-Sensing Res.*, vol. 14, no. April, pp. 30–38, Jun. 2017, doi: 10.1016/j.sbsr.2017.04.001.

[6] J. Homola, "Present and future of surface plasmon resonance biosensors," *Anal. Bioanal. Chem.*, vol. 377, no. 3, pp. 528–539, Oct. 2003, doi: 10.1007/s00216-003-2101-0.

[7] R. Otupiri, E. K. Akowuah, S. Haxha, H. Ademgil, F. AbdelMalek, and A. Aggoun, "A Novel Birefrigent Photonic Crystal Fiber Surface Plasmon Resonance Biosensor," *IEEE Photonics J.*, vol. 6, no. 4, pp. 1–11, Aug. 2014, doi: 10.1109/JPHOT.2014.2335716.

[8] J. Ortega-Mendoza, A. Padilla-Vivanco, C. Toxqui-Quitl, P. Zaca-Morán, D. Villegas-Hernández, and F. Chávez, "Optical Fiber Sensor Based on Localized Surface Plasmon Resonance Using Silver Nanoparticles Photodeposited on the Optical Fiber End," *Sensors*, vol. 14, no. 10, pp. 18701–18710, Oct. 2014, doi: 10.3390/s141018701.

[9] E. K. Akowuah, T. Gorman, H. Ademgil, S. Haxha, G. K. Robinson, and J. V. Oliver, "Numerical analysis of a photonic crystal fiber for biosensing applications," *IEEE J. Quantum Electron.*, vol. 48, no. 11, pp. 1403–1410, 2012, doi: 10.1109/JQE.2012.2213803.

[10] A. A. Rifat *et al.*, "Photonic crystal fiber based plasmonic sensors," *Sensors Actuators B Chem.*, vol. 243, pp. 311–325, May 2017, doi: 10.1016/j.snb.2016.11.113.

[11] J. Piehler, A. Brecht, and G. Gauglitz, "Affinity Detection of Low Molecular Weight Analytes," *Anal. Chem.*, vol. 68, no. 1, pp. 139–143, Jan. 1996, doi: 10.1021/ac9504878.

[12] R. G. Heideman, R. P. H. Kooyman, and J. Greve, "Performance of a highly sensitive optical waveguide Mach-Zehnder interferometer immunosensor," *Sensors Actuators B Chem.*, vol. 10, no. 3, pp. 209–217, Feb. 1993, doi: 10.1016/0925-4005(93)87008-D.

[13] C. A. Rowe-Taitt, J. W. Hazzard, K. E. Hoffman, J. J. Cras, J. P. Golden, and F. S. Ligler, "Simultaneous detection of six biohazardous agents using a planar waveguide array biosensor," *Biosens. Bioelectron.*, vol. 15, no. 11–12, pp. 579–589, Dec. 2000, doi: 10.1016/S0956-5663(00)00122-6.

[14] D. Clerc and W. Lukosz, "Integrated optical output grating coupler as biochemical sensor," *Sensors Actuators B Chem.*, vol. 19, no. 1–3, pp. 581–586, Apr. 1994, doi: 10.1016/0925-4005(93)01090-Q.

[15] R. Cush, J. M. Cronin, W. J. Stewart, C. H. Maule, J. Molloy, and N. J. Goddard, "The resonant mirror: a novel optical biosensor for direct sensing of biomolecular interactions Part I: Principle of operation and associated instrumentation," *Biosens. Bioelectron.*, vol. 8, no. 7–8, pp. 347–354, Jan. 1993, doi: 10.1016/0956-5663(93)80073-X.

[16] "Optical Biosensors: Present & Future - Google Books." https://books.google.com.bd/books?hl=en&lr=&id=HLGw94bcNBYC&oi=fnd&pg=PA207&dq=Homola+J,+Yee+S,+Myszka+D+(2002)+Surface+plasmon+biosensors.+In:+Ligler+FS,+Taitt+CR+(eds)+Optical+biosensors:+present+and+future.+Elsevier.&ots=vmH128o0cE&sig=gU6k1xGIE5rn4GRxlOBe9t67wRE&redir_esc=y#v=onepage&q&f=false (accessed Mar. 06, 2021).

[17] R. Stoltenburg, C. Reinemann, and B. Strehlitz, "SELEX—A (r)evolutionary method to generate high-affinity nucleic acid ligands," *Biomol. Eng.*, vol. 24, no. 4, pp. 381–403, Oct. 2007, doi: 10.1016/j.bioeng.2007.06.001.

[18] S. Ray, G. Mehta, and S. Srivastava, "Label-free detection techniques for protein microarrays: Prospects, merits and challenges," *Proteomics*, vol. 10, no. 4, pp. 731–748, Feb. 2010, doi: 10.1002/pmic.200900458.

[19] E. Kretschmann and H. Raether, "Notizen: Radiative Decay of Non Radiative Surface Plasmons Excited by Light," *Zeitschrift für Naturforsch. A*, vol. 23, no. 12, pp. 2135–2136, Dec. 1968, doi: 10.1515/zna-1968-1247.

[20] J. N. Dash, R. Das, and R. Jha, "AZO coated microchannel incorporated PCF-based SPR

sensor: A numerical analysis," *IEEE Photonics Technol. Lett.*, vol. 30, no. 11, pp. 1032–1035, 2018, doi: 10.1109/LPT.2018.2829920.

[21] S. I. Azzam, M. F. O. Hameed, R. E. A. Shehata, A. M. Heikal, and S. S. A. Obayya, "Multichannel photonic crystal fiber surface plasmon resonance based sensor," *Opt. Quantum Electron.*, vol. 48, no. 2, p. 142, Feb. 2016, doi: 10.1007/s11082-016-0414-4.

[22] A. A. Rifat, F. haider, R. Ahmed, G. A. Mahdiraji, F. R. Mahamd Adikan, and A. E. Miroshnichenko, "Highly sensitive selectively coated photonic crystal fiber-based plasmonic sensor," *Opt. Lett.*, vol. 43, no. 4, p. 891, Feb. 2018, doi: 10.1364/OL.43.000891.

[23] B. Liedberg, C. Nylander, and I. Lunström, "Surface plasmon resonance for gas detection and biosensing," *Sensors and Actuators*, vol. 4, pp. 299–304, Jan. 1983, doi: 10.1016/0250-6874(83)85036-7.

[24] S. Weng, L. Pei, J. Wang, T. Ning, and J. Li, "High sensitivity D-shaped hole fiber temperature sensor based on surface plasmon resonance with liquid filling," *Photonics Res.*, vol. 5, no. 2, p. 103, Apr. 2017, doi: 10.1364/PRJ.5.000103.

[25] M. A. Mollah, S. M. R. Islam, M. Yousufali, L. F. Abdulrazak, M. B. Hossain, and I. S. Amiri, "Plasmonic temperature sensor using D-shaped photonic crystal fiber," *Results Phys.*, vol. 16, p. 102966, Mar. 2020, doi: 10.1016/j.rinp.2020.102966.

[26] Y. Ying, J.-K. Wang, K. Xu, and G.-Y. Si, "High sensitivity D-shaped optical fiber strain sensor based on surface plasmon resonance," *Opt. Commun.*, vol. 460, p. 125147, Apr. 2020, doi: 10.1016/j.optcom.2019.125147.

[27] B. Han *et al.*, "Simultaneous measurement of temperature and strain based on dual SPR effect in PCF," *Opt. Laser Technol.*, vol. 113, pp. 46–51, May 2019, doi: 10.1016/j.optlastec.2018.12.010.

[28] S. A. Maier, "Plasmonics: The Promise of Highly Integrated Optical Devices," *IEEE J. Sel. Top. Quantum Electron.*, vol. 12, no. 6, pp. 1671–1677, Nov. 2006, doi: 10.1109/JSTQE.2006.884086.

[29] S. P. Burgos, H. W. Lee, E. Feigenbaum, R. M. Briggs, and H. A. Atwater, "Synthesis and Characterization of Plasmonic Resonant Guided Wave Networks," *Nano Lett.*, vol. 14, no. 6, pp. 3284–3292, Jun. 2014, doi: 10.1021/nl500694c.

[30] A. Khaleque and H. T. Hattori, "Ultra-broadband and compact polarization splitter based on gold filled dual-core photonic crystal fiber," *J. Appl. Phys.*, vol. 118, no. 14, p. 143101, Oct. 2015, doi: 10.1063/1.4932659.

[31] W. Qin, S. Li, Y. Yao, X. Xin, and J. Xue, "Analyte-filled core self-calibration

microstructured optical fiber based plasmonic sensor for detecting high refractive index aqueous analyte," *Opt. Lasers Eng.*, vol. 58, pp. 1–8, Jul. 2014, doi: 10.1016/j.optlaseng.2014.01.003.

[32] M. S. Islam, M. R. Islam, J. Sultana, A. Dinovitser, B. W.-H. Ng, and D. Abbott, "Exposed-core localized surface plasmon resonance biosensor," *J. Opt. Soc. Am. B*, vol. 36, no. 8, p. 2306, Aug. 2019, doi: 10.1364/josab.36.002306.

[33] M. M. Rahman, F. A. Mou, M. I. H. Bhuiyan, and M. R. Islam, "Photonic crystal fiber based terahertz sensor for cholesterol detection in human blood and liquid foodstuffs," *Sens. Bio-Sensing Res.*, vol. 29, p. 100356, Aug. 2020, doi: 10.1016/j.sbsr.2020.100356.

[34] F. A. Mou, M. M. Rahman, M. R. Islam, and M. I. H. Bhuiyan, "Development of a photonic crystal fiber for THz wave guidance and environmental pollutants detection," *Sens. Bio-Sensing Res.*, vol. 29, p. 100346, Aug. 2020, doi: 10.1016/j.sbsr.2020.100346.

[35] M. R. Islam, M. F. Kabir, K. M. A. Talha, and M. S. Islam, "A novel hollow core terahertz refractometric sensor," *Sens. Bio-Sensing Res.*, vol. 25, p. 100295, Sep. 2019, doi: 10.1016/j.sbsr.2019.100295.

[36] J. Sultana, M. S. Islam, K. Ahmed, A. Dinovitser, B. W.-H. Ng, and D. Abbott, "Terahertz detection of alcohol using a photonic crystal fiber sensor," *Appl. Opt.*, vol. 57, no. 10, p. 2426, Apr. 2018, doi: 10.1364/ao.57.002426.

[37] M. S. Islam *et al.*, "A novel Zeonex based photonic sensor for alcohol detection in beverages," in *2017 IEEE International Conference on Telecommunications and Photonics (ICTP)*, Dec. 2017, pp. 114–118, doi: 10.1109/ICTP.2017.8285905.

[38] J. N. Dash and R. Jha, "SPR Biosensor Based on Polymer PCF Coated With Conducting Metal Oxide," *IEEE Photonics Technol. Lett.*, vol. 26, no. 6, pp. 595–598, Mar. 2014, doi: 10.1109/LPT.2014.2301153.

[39] A. A. Rifat, R. Ahmed, G. A. Mahdiraji, and F. R. M. Adikan, "Highly Sensitive D-Shaped Photonic Crystal Fiber-Based Plasmonic Biosensor in Visible to Near-IR," *IEEE Sens. J.*, vol. 17, no. 9, pp. 2776–2783, May 2017, doi: 10.1109/JSEN.2017.2677473.

[40] S. Sharmin, A. Bosu, and S. Akter, "A Simple Gold-Coated Photonic Crystal Fiber Based Plasmonic Biosensor," in *2018 International Conference on Advancement in Electrical and Electronic Engineering (ICAEEE)*, Nov. 2018, pp. 1–4, doi: 10.1109/ICAEEE.2018.8643003.

[41] M. R. Islam, M. Arif Hossain, S. I. Ali, J. Sultana, and M. Saiful Islam, "Design and Characterization of an Ultra Low Loss, Dispersion-Flattened Slotted Photonic Crystal Fiber for Terahertz Application," *J. Opt. Commun.*, Nov. 2018, doi: 10.1515/joc-2018-

0152.

[42] W. Gao *et al.*, “Experimental investigation on supercontinuum generation by single, dual, and triple wavelength pumping in a silica photonic crystal fiber,” *Appl. Opt.*, vol. 55, no. 33, p. 9514, Nov. 2016, doi: 10.1364/AO.55.009514.

[43] A. Aming, M. Uthman, R. Chitaree, W. Mohammed, and B. M. A. Rahman, “Design and Characterization of Porous Core Polarization Maintaining Photonic Crystal Fiber for THz Guidance,” *J. Light. Technol.*, vol. 34, no. 23, pp. 5583–5590, 2016, doi: 10.1109/JLT.2016.2623657.

[44] N. Muduli and H. K. Padhy, “An optimized configuration of large mode field area PMMA photonic crystal fiber with low bending loss: a new approach,” *J. Mater. Sci. Mater. Electron.*, vol. 27, no. 2, pp. 1906–1912, Feb. 2016, doi: 10.1007/s10854-015-3972-5.

[45] K. Nielsen, H. K. Rasmussen, A. J. Adam, P. C. Planken, O. Bang, and P. U. Jepsen, “Bendable, low-loss Topas fibers for the terahertz frequency range,” *Opt. Express*, vol. 17, no. 10, p. 8592, May 2009, doi: 10.1364/OE.17.008592.

[46] H. Bao, K. Nielsen, H. K. Rasmussen, P. U. Jepsen, and O. Bang, “Fabrication and characterization of porous-core honeycomb bandgap THz fibers,” *Opt. Express*, vol. 20, no. 28, p. 29507, Dec. 2012, doi: 10.1364/OE.20.029507.

[47] H. Han, H. Park, M. Cho, and J. Kim, “Terahertz pulse propagation in a plastic photonic crystal fiber,” *Appl. Phys. Lett.*, vol. 80, no. 15, pp. 2634–2636, Apr. 2002, doi: 10.1063/1.1468897.

[48] M. Rabiul Hasan, M. Ariful Islam, M. S. Anower, and S. M. A. Razzak, “Low-loss and bend-insensitive terahertz fiber using a rhombic-shaped core,” *Appl. Opt.*, vol. 55, no. 30, p. 8441, 2016, doi: 10.1364/ao.55.008441.

[49] J. Noda, K. Okamoto, and Y. Sasaki, “Polarization-maintaining fibers and their applications,” *J. Light. Technol.*, vol. 4, no. 8, pp. 1071–1089, 1986, doi: 10.1109/JLT.1986.1074847.

[50] J. Lægsgaard, N. A. Mortensen, and A. Bjarklev, “Mode areas and field-energy distribution in honeycomb photonic bandgap fibers,” *J. Opt. Soc. Am. B*, vol. 20, no. 10, p. 2037, Oct. 2003, doi: 10.1364/JOSAB.20.002037.

[51] P. S. Maji and P. R. Chaudhuri, “Geometrical parameters dependence towards ultra-flat dispersion square-lattice PCF using tunable liquid infiltration,” in *Workshop on Recent Advances in Photonics (WRAP)*, Dec. 2013, pp. 1–2, doi: 10.1109/WRAP.2013.6917653.

[52] R. Islam, M. S. Habib, G. K. M. Hasanuzzaman, S. Rana, M. A. Sadath, and C. Markos, "A Novel Low-Loss Diamond-Core Porous Fiber for Polarization Maintaining Terahertz Transmission," *IEEE Photonics Technol. Lett.*, vol. 28, no. 14, pp. 1537–1540, 2016, doi: 10.1109/LPT.2016.2550205.

[53] K. Ahmed and M. Morshed, "Design and numerical analysis of microstructured-core octagonal photonic crystal fiber for sensing applications," *Sens. Bio-Sensing Res.*, vol. 7, pp. 1–6, Mar. 2016, doi: 10.1016/j.sbsr.2015.10.005.

[54] S. Li, "Equiangular spiral photonic crystal fiber for code synchronization in all-optical analog-to-digital conversion based on lumped time delay compensation scheme," *Optik (Stuttg).*, vol. 127, no. 11, pp. 4693–4697, Jun. 2016, doi: 10.1016/j.ijleo.2016.02.017.

[55] S. Luke, S. K. Sudheer, and V. P. M. Pillai, "Tellurite based circular photonic crystal fiber with high nonlinearity and low confinement loss," *Optik (Stuttg).*, vol. 127, no. 23, pp. 11138–11142, Dec. 2016, doi: 10.1016/j.ijleo.2016.09.024.

[56] A. Cerqueira S., Jr., C. M. B. Cordeiro, F. Biancalana, P. J. Roberts, H. E. Hernandez-Figueroa, and C. H. B. Cruz, "Nonlinear interaction between two different photonic bandgaps of a hybrid photonic crystal fiber," *Opt. Lett.*, vol. 33, no. 18, p. 2080, Sep. 2008, doi: 10.1364/OL.33.002080.

[57] L.-J. Chen, H.-W. Chen, T.-F. Kao, J.-Y. Lu, and C.-K. Sun, "Low-loss subwavelength plastic fiber for terahertz waveguiding," *Opt. Lett.*, vol. 31, no. 3, p. 308, 2006, doi: 10.1364/OL.31.000308.

[58] J. A. Buck and J. A., "Fundamentals of Optical Fibers, 2nd Edition," *fof*, p. 352, 2004, Accessed: Mar. 07, 2021. [Online]. Available: https://ui.adsabs.harvard.edu/abs/2004fof..book.....B/abstract.

[59] K. KANESHIMA, "Numerical Investigation of Octagonal Photonic Crystal Fibers with Strong Confinement Field," *IEICE Trans. Electron.*, vol. E89-C, no. 6, pp. 830–837, Jun. 2006, doi: 10.1093/ietele/e89-c.6.830.

[60] L. G. Carrascosa *et al.*, "Molecular inversion probe-based SPR biosensing for specific, label-free and real-time detection of regional DNA methylation," *Chem. Commun.*, vol. 50, no. 27, pp. 3585–3588, 2014, doi: 10.1039/C3CC49607D.

[61] M. S. Islam *et al.*, "A novel approach for spectroscopic chemical identification using photonic crystal fiber in the terahertz regime," *IEEE Sens. J.*, vol. 18, no. 2, pp. 575–582, Jan. 2018, doi: 10.1109/JSEN.2017.2775642.

[62] M. S. Islam, J. Sultana, A. A. Rifat, A. Dinovitser, B. Wai-Him Ng, and D. Abbott, "Terahertz Sensing in a Hollow Core Photonic Crystal Fiber," *IEEE Sens. J.*, vol. 18,

no. 10, pp. 4073–4080, May 2018, doi: 10.1109/JSEN.2018.2819165.

[63] J. N. Dash and R. Jha, “Highly Sensitive Side-Polished Birefringent PCF-Based SPR Sensor in near IR,” *Plasmonics*, vol. 11, no. 6, pp. 1505–1509, Dec. 2016, doi: 10.1007/s11468-016-0203-8.

[64] J. N. Dash and R. Das, “SPR based magnetic-field sensing in microchannelled PCF: a numerical approach,” *J. Opt.*, vol. 20, no. 11, p. 115001, Nov. 2018, doi: 10.1088/2040-8986/aae119.

[65] J. N. Dash and R. Jha, “On the Performance of Graphene-Based D-Shaped Photonic Crystal Fibre Biosensor Using Surface Plasmon Resonance,” *Plasmonics*, vol. 10, no. 5, pp. 1123–1131, Oct. 2015, doi: 10.1007/s11468-015-9912-7.

[66] G. P. Anderson and C. R. Taitt, “EVANESCENT WAVE FIBER OPTIC BIOSENSORS,” in *Optical Biosensors*, Elsevier, 2008, pp. 83–138.

[67] M. Hautakorpi, M. Mattinen, and H. Ludvigsen, “Surface-plasmon-resonance sensor based on three-hole microstructured optical fiber,” *Opt. Express*, vol. 16, no. 12, p. 8427, Jun. 2008, doi: 10.1364/OE.16.008427.

[68] A. Hassani and M. Skorobogatiy, “Design criteria for microstructured-optical-fiber-based surface-plasmon-resonance sensors,” *J. Opt. Soc. Am. B*, vol. 24, no. 6, p. 1423, Jun. 2007, doi: 10.1364/JOSAB.24.001423.

[69] X. Yu *et al.*, “A selectively coated photonic crystal fiber based surface plasmon resonance sensor,” *J. Opt.*, vol. 12, no. 1, p. 015005, Jan. 2010, doi: 10.1088/2040-8978/12/1/015005.

[70] B. Shuai, L. Xia, Y. Zhang, and D. Liu, “A multi-core holey fiber based plasmonic sensor with large detection range and high linearity,” *Opt. Express*, vol. 20, no. 6, p. 5974, Mar. 2012, doi: 10.1364/OE.20.005974.

[71] N. Luan, R. Wang, W. Lv, and J. Yao, “Surface plasmon resonance sensor based on D-shaped microstructured optical fiber with hollow core,” *Opt. Express*, vol. 23, no. 7, p. 8576, Apr. 2015, doi: 10.1364/OE.23.008576.

[72] M. E. Rahaman, R. Saha, M. S. Ahsan, and I. B. Sohn, “Design and performance analysis of a D-shaped PCF and surface plasmon resonance based glucose sensor,” *4th Int. Conf. Electr. Eng. Inf. Commun. Technol. iCEEiCT 2018*, pp. 325–329, 2019, doi: 10.1109/CEEICT.2018.8628080.

[73] N. Luan and J. Yao, “Refractive Index and Temperature Sensing Based on Surface Plasmon Resonance and Directional Resonance Coupling in a PCF,” *IEEE Photonics J.*, vol. 9, no. 2, pp. 1–5, 2017, doi: 10.1109/JPHOT.2017.2667878.

[74] G. An, X. Hao, S. Li, X. Yan, and X. Zhang, “D-shaped photonic crystal fiber refractive index sensor based on surface plasmon resonance,” *Appl. Opt.*, vol. 56, no. 24, p. 6988, 2017, doi: 10.1364/ao.56.006988.

[75] T. Ahmed, A. K. Paul, M. S. Anower, and S. M. A. Razzak, “Surface plasmon resonance biosensor based on hexagonal lattice dual-core photonic crystal fiber,” *Appl. Opt.*, vol. 58, no. 31, p. 8416, Nov. 2019, doi: 10.1364/AO.58.008416.

[76] F. Haider, R. A. Aoni, R. Ahmed, M. S. Islam, and A. E. Miroshnichenko, “Propagation Controlled Photonic Crystal Fiber-Based Plasmonic Sensor via Scaled-Down Approach,” *IEEE Sens. J.*, vol. 19, no. 3, pp. 962–969, Feb. 2019, doi: 10.1109/JSEN.2018.2880161.

[77] M. R. Momota and M. R. Hasan, “Hollow-core silver coated photonic crystal fiber plasmonic sensor,” *Opt. Mater. (Amst).*, vol. 76, pp. 287–294, Feb. 2018, doi: 10.1016/j.optmat.2017.12.049.

[78] C. Caucheteur, T. Guo, and J. Albert, “Review of plasmonic fiber optic biochemical sensors: improving the limit of detection,” *Anal. Bioanal. Chem.*, vol. 407, no. 14, pp. 3883–3897, May 2015, doi: 10.1007/s00216-014-8411-6.

[79] A. Rifat, G. Mahdiraji, D. Chow, Y. Shee, R. Ahmed, and F. Adikan, “Photonic Crystal Fiber-Based Surface Plasmon Resonance Sensor with Selective Analyte Channels and Graphene-Silver Deposited Core,” *Sensors*, vol. 15, no. 5, pp. 11499–11510, May 2015, doi: 10.3390/s150511499.

[80] E. K. Akowuah, T. Gorman, H. Ademgil, and S. Haxha, “A highly sensitive photonic crystal fibre (PCF) surface plasmon resonance (SPR) sensor based on a bimetallic structure of gold and silver,” in *Proceedings of the 2012 IEEE 4th International Conference on Adaptive Science and Technology, ICAST 2012*, 2012, pp. 121–125, doi: 10.1109/ICASTech.2012.6381078.

[81] A. H. El-Saeed, A. E. Khalil, M. F. O. Hameed, M. Y. Azab, and S. S. A. Obayya, “Highly sensitive SPR PCF biosensors based on Ag/TiN and Ag/ZrN configurations,” *Opt. Quantum Electron.*, vol. 51, no. 2, pp. 1–18, 2019, doi: 10.1007/s11082-019-1764-5.

[82] Q. Liu, S. Li, H. Chen, J. Li, and Z. Fan, “High-sensitivity plasmonic temperature sensor based on photonic crystal fiber coated with nanoscale gold film,” *Appl. Phys. Express*, vol. 8, no. 4, p. 046701, Apr. 2015, doi: 10.7567/APEX.8.046701.

[83] M. S. Islam *et al.*, “Dual-polarized highly sensitive plasmonic sensor in the visible to near-IR spectrum,” *Opt. Express*, vol. 26, no. 23, p. 30347, Nov. 2018, doi:

10.1364/oe.26.030347.

[84] M. R. Islam *et al.*, “Design and analysis of birefringent SPR based PCF biosensor with ultra-high sensitivity and low loss,” *Optik (Stuttg).*, vol. 221, p. 165311, Nov. 2020, doi: 10.1016/j.ijleo.2020.165311.

[85] M. S. Islam *et al.*, “A Hi-Bi Ultra-Sensitive Surface Plasmon Resonance Fiber Sensor,” *IEEE Access*, vol. 7, pp. 79085–79094, 2019, doi: 10.1109/ACCESS.2019.2922663.

[86] “RP Photonics Encyclopedia - silica fibers, optical fiber, glass, fiber optics.” https://www.rp-photonics.com/silica_fibers.html (accessed Feb. 19, 2021).

[87] B. K. Paul *et al.*, “The design and analysis of a dual-diamond-ring PCF-based sensor,” *J. Comput. Electron.*, vol. 19, no. 3, pp. 1288–1294, Sep. 2020, doi: 10.1007/s10825-020-01509-2.

[88] T. Han, Y. G. Liu, Z. Wang, J. Guo, and J. Yu, “A High Sensitivity Strain Sensor Based on the Zero-Group-Birefringence Effect in a Selective-Filling High Birefringent Photonic Crystal Fiber,” *IEEE Photonics J.*, vol. 10, no. 1, pp. 1–9, Feb. 2018, doi: 10.1109/JPHOT.2017.2782223.

[89] A. A. Rifat *et al.*, “Surface Plasmon Resonance Photonic Crystal Fiber Biosensor: A Practical Sensing Approach,” *IEEE Photonics Technol. Lett.*, vol. 27, no. 15, pp. 1628–1631, Aug. 2015, doi: 10.1109/LPT.2015.2432812.

[90] M. S. Islam *et al.*, “Localized surface plasmon resonance biosensor: an improved technique for SERS response intensification,” *Opt. Lett.*, vol. 44, no. 5, p. 1134, Mar. 2019, doi: 10.1364/ol.44.001134.

[91] J. R. DeVore, “Refractive Indices of Rutile and Sphalerite,” *J. Opt. Soc. Am.*, vol. 41, no. 6, p. 416, Jun. 1951, doi: 10.1364/josa.41.000416.

[92] G. V. Naik, V. M. Shalaev, and A. Boltasseva, “Alternative Plasmonic Materials: Beyond Gold and Silver,” *Adv. Mater.*, vol. 25, no. 24, pp. 3264–3294, Jun. 2013, doi: 10.1002/adma.201205076.

[93] S. Novais, M. S. Ferreira, and J. L. Pinto, “Determination of thermo-optic coefficient of ethanol-water mixtures with optical fiber tip sensor,” *Opt. Fiber Technol.*, vol. 45, no. August, pp. 276–279, Nov. 2018, doi: 10.1016/j.yofte.2018.08.002.

[94] M. Rakibul Islam, M. M. I. Khan, F. Mehjabin, J. Alam Chowdhury, and M. Islam, “Design of a fabrication friendly & highly sensitive surface plasmon resonance-based photonic crystal fiber biosensor,” *Results Phys.*, vol. 19, p. 103501, Dec. 2020, doi: 10.1016/j.rinp.2020.103501.

[95] M. Rakibul Islam, A. N. M. Iftekher, K. Rakibul Hasan, M. J. Nayen, and S. Bin Islam,

"Dual-polarized highly sensitive surface-plasmon-resonance-based chemical and biomolecular sensor," *Appl. Opt.*, vol. 59, no. 11, p. 3296, Apr. 2020, doi: 10.1364/ao.383352.

[96] P. Bing, S. Huang, J. Sui, H. Wang, and Z. Wang, "Analysis and Improvement of a Dual-Core Photonic Crystal Fiber Sensor," *Sensors*, vol. 18, no. 7, p. 2051, Jun. 2018, doi: 10.3390/s18072051.

[97] S. Chakma, M. A. Khalek, B. K. Paul, K. Ahmed, M. R. Hasan, and A. N. Bahar, "Gold-coated photonic crystal fiber biosensor based on surface plasmon resonance: Design and analysis," *Sens. Bio-Sensing Res.*, vol. 18, pp. 7–12, Apr. 2018, doi: 10.1016/j.sbsr.2018.02.003.

[98] M. Aminul Islam, M. Rakibul Islam, M. Moinul Islam Khan, J. A. Chowdhury, F. Mehjabin, and M. Islam, "Highly Birefringent Slotted Core Photonic Crystal Fiber for THz Wave Propagation," *Phys. Wave Phenom.*, vol. 28, no. 1, pp. 58–67, Jan. 2020, doi: 10.3103/S1541308X20010021.

[99] V. Kaur and S. Singh, "Design approach of solid-core photonic crystal fiber sensor with sensing ring for blood component detection," *J. Nanophotonics*, vol. 13, no. 02, p. 1, May 2019, doi: 10.1117/1.jnp.13.026011.

[100] Lu Peng, Fukun Shi, Guiyao Zhou, Shu Ge, Zhiyun Hou, and Changming Xia, "A Surface Plasmon Biosensor Based on a D-Shaped Microstructured Optical Fiber With Rectangular Lattice," *IEEE Photonics J.*, vol. 7, no. 5, pp. 1–9, Oct. 2015, doi: 10.1109/JPHOT.2015.2488278.

[101] F. Chiavaioli, C. A. J. Gouveia, P. A. S. Jorge, and F. Baldini, "Towards a uniform metrological assessment of grating-based optical fiber sensors: From refractometers to biosensors," *Biosensors*, vol. 7, no. 2. MDPI AG, Jun. 21, 2017, doi: 10.3390/bios7020023.

[102] X. Zhang *et al.*, "Twist sensor based on surface plasmon resonance excitation using two spectral combs in one tilted fiber Bragg grating," *J. Opt. Soc. Am. B*, vol. 36, no. 5, p. 1176, May 2019, doi: 10.1364/josab.36.001176.

[103] C. Caucheteur, M. Loyez, Á. González-Vila, and R. Wattiez, "Evaluation of gold layer configuration for plasmonic fiber grating biosensors," *Opt. Express*, vol. 26, no. 18, p. 24154, Sep. 2018, doi: 10.1364/OE.26.024154.

[104] V. Kaur and S. Singh, "Design of titanium nitride coated PCF-SPR sensor for liquid sensing applications," *Opt. Fiber Technol.*, vol. 48, pp. 159–164, Mar. 2019, doi: 10.1016/j.yofte.2018.12.015.

[105] A. A. Rifat, G. A. Mahdiraji, Y. G. Shee, M. J. Shawon, and F. R. M. Adikan, “A Novel Photonic Crystal Fiber Biosensor Using Surface Plasmon Resonance,” in *Procedia Engineering*, 2016, vol. 140, pp. 1–7, doi: 10.1016/j.proeng.2015.08.1107.

[106] X. Yang, Y. Lu, B. Liu, and J. Yao, “Analysis of Graphene-Based Photonic Crystal Fiber Sensor Using Birefringence and Surface Plasmon Resonance,” *Plasmonics*, vol. 12, no. 2, pp. 489–496, Apr. 2017, doi: 10.1007/s11468-016-0289-z.

[107] M. N. Hossen, M. Ferdous, M. Abdul Khalek, S. Chakma, B. K. Paul, and K. Ahmed, “Design and analysis of biosensor based on surface plasmon resonance,” *Sens. Bio-Sensing Res.*, vol. 21, pp. 1–6, Nov. 2018, doi: 10.1016/j.sbsr.2018.08.003.

[108] C. Liu *et al.*, “Analysis of a highly birefringent asymmetric photonic crystal fibre based on a surface plasmon resonance sensor,” *J. Mod. Opt.*, vol. 63, no. 12, pp. 1189–1195, Jul. 2016, doi: 10.1080/09500340.2015.1135257.

[109] D. Li, W. Zhang, H. Liu, J. Hu, and G. Zhou, “High Sensitivity Refractive Index Sensor Based on Multicoating Photonic Crystal Fiber With Surface Plasmon Resonance at Near-Infrared Wavelength,” *IEEE Photonics J.*, vol. 9, no. 2, pp. 1–8, Apr. 2017, doi: 10.1109/JPHOT.2017.2687121.

[110] M. A. Mollah, A. K. Paul, and S. M. A. Razzak, “Dual Polarized Plasmonic Refractive Index Sensor based on Photonic Crystal Fiber,” in *2018 10th International Conference on Electrical and Computer Engineering (ICECE)*, Dec. 2018, pp. 73–76, doi: 10.1109/ICECE.2018.8636749.

[111] A. K. Paul, A. K. Sarkar, and S. M. A. Razzak, “Graphene coated photonic crystal fiber biosensor based on surface plasmon resonance,” in *2017 IEEE Region 10 Humanitarian Technology Conference (R10-HTC)*, Dec. 2017, pp. 856–859, doi: 10.1109/R10-HTC.2017.8289088.

[112] Z. Liu *et al.*, “Reflective-distributed SPR sensor based on twin-core fiber,” *Opt. Commun.*, vol. 366, pp. 107–111, May 2016, doi: 10.1016/j.optcom.2015.12.018.

[113] M. Murawski, L. R. Jaroszewicz, and K. Stasiewicz, “A photonic crystal fiber splice with a standard single mode fiber,” *Photonics Lett. Pol.*, vol. 1, no. 3, pp. 115–117, Sep. 2009, doi: 10.4302/plp.2009.3.05.

[114] D. Fan *et al.*, “Extremely High-Efficiency Coupling Method for Hollow-Core Photonic Crystal Fiber,” *IEEE Photonics J.*, vol. 9, no. 3, pp. 1–8, Jun. 2017, doi: 10.1109/JPHOT.2017.2697969.

[115] H. Wei, Y. Zhu, and S. Krishnaswamy, “Numerical Analysis of Waveguide Coupling Between Photonic Crystal Fiber and Single-Mode Fiber,” *IEEE Photonics Technol.*

Lett., vol. 27, no. 20, pp. 2142–2145, Oct. 2015, doi: 10.1109/LPT.2015.2454506.

[116] H. Yokota, H. Yashima, Y. Imai, and Y. Sasaki, "Coupling Characteristics of Fused Optical Fiber Coupler Formed with Single-Mode Fiber and Photonic Crystal Fiber Having Air Hole Collapsed Taper," *Adv. Optoelectron.*, vol. 2016, pp. 1–8, 2016, doi: 10.1155/2016/6219895.

[117] M. Al Mahfuz, M. A. Hossain, E. Haque, N. H. Hai, Y. Namihira, and F. Ahmed, "Dual-Core Photonic Crystal Fiber-Based Plasmonic RI Sensor in the Visible to Near-IR Operating Band," *IEEE Sens. J.*, vol. 20, no. 14, pp. 7692–7700, Mar. 2020, doi: 10.1109/jsen.2020.2980327.

[118] M. S. Islam, J. Sultana, A. Dinovitser, B. W.-H. Ng, and D. Abbott, "A Gold Coated Plasmonic Sensor for Biomedical and Biochemical Analyte Detection," in *2018 43rd International Conference on Infrared, Millimeter, and Terahertz Waves (IRMMW-THz)*, Sep. 2018, pp. 1–2, doi: 10.1109/IRMMW-THz.2018.8510018.

[119] M. N. Sakib *et al.*, "Numerical Study of Circularly Slotted Highly Sensitive Plasmonic Biosensor: A Novel Approach," *Results Phys.*, vol. 17, Jun. 2020, doi: 10.1016/j.rinp.2020.103130.

[120] G. A. Mahdiraji *et al.*, "Challenges and solutions in fabrication of silica-based photonic crystal fibers: An experimental study," *Fiber Integr. Opt.*, vol. 33, no. 1–2, pp. 85–104, Jan. 2014, doi: 10.1080/01468030.2013.879680.

[121] T. Zhao, S. Lou, X. Wang, W. Zhang, and Y. Wang, "Simultaneous Measurement of Curvature, Strain and Temperature Using a Twin-Core Photonic Crystal Fiber-Based Sensor," *Sensors*, vol. 18, no. 7, p. 2145, Jul. 2018, doi: 10.3390/s18072145.

[122] M. Liu, X. Yang, P. Shum, and H. Yuan, "High-sensitivity birefringent and single-layer coating photonic crystal fiber biosensor based on surface plasmon resonance," *Appl. Opt.*, vol. 57, no. 8, p. 1883, Mar. 2018, doi: 10.1364/AO.57.001883.

[123] J. N. Dash and R. Jha, "Graphene-based birefringent photonic crystal fiber sensor using surface plasmon resonance," *IEEE Photonics Technol. Lett.*, vol. 26, no. 11, pp. 1092–1095, Jun. 2014, doi: 10.1109/LPT.2014.2315233.

[124] M. R. Hasan *et al.*, "Spiral photonic crystal fiber-based dual-polarized surface plasmon resonance biosensor," *IEEE Sens. J.*, vol. 18, no. 1, pp. 133–140, Jan. 2018, doi: 10.1109/JSEN.2017.2769720.

[125] A. Aray, H. Saghafifar, and M. Soltanolkotabi, "Calculation of Dispersion Relation and Single Mode Operation in Surface Plasmon Resonance Based Fiber Optic Refractive Index Sensors," *J. Light. Technol.*, vol. 34, no. 11, pp. 2782–2788, Jun. 2016, doi:

10.1109/JLT.2016.2542199.

[126] Z.-W. Ding, T.-T. Lang, Y. Wang, and C.-L. Zhao, “Surface Plasmon Resonance Refractive Index Sensor Based on Tapered Coreless Optical Fiber Structure,” *J. Light. Technol.*, vol. 35, no. 21, pp. 4734–4739, Nov. 2017, doi: 10.1109/JLT.2017.2755668.

[127] S. Jiao, S. Gu, H. Yang, H. Fang, and S. Xu, “Highly sensitive dual-core photonic crystal fiber based on a surface plasmon resonance sensor with a silver nano-continuous grating,” *Appl. Opt.*, vol. 57, no. 28, p. 8350, Oct. 2018, doi: 10.1364/ao.57.008350.

[128] E. Haque, M. A. Hossain, F. Ahmed, and Y. Namihira, “Surface Plasmon Resonance Sensor Based on Modified D-Shaped Photonic Crystal Fiber for Wider Range of Refractive Index Detection,” *IEEE Sens. J.*, vol. 18, no. 20, pp. 8287–8293, 2018, doi: 10.1109/JSEN.2018.2865514.

[129] E. Haque, M. Anwar Hossain, Y. Namihira, and F. Ahmed, “Microchannel-based plasmonic refractive index sensor for low refractive index detection,” *Appl. Opt.*, vol. 58, no. 6, p. 1547, Feb. 2019, doi: 10.1364/AO.58.001547.

[130] S. M. George, “Atomic Layer Deposition: An Overview,” *Chem. Rev.*, vol. 110, no. 1, pp. 111–131, Jan. 2010, doi: 10.1021/cr900056b.

[131] A. L. Johnson and J. D. Parish, “Recent developments in molecular precursors for atomic layer deposition,” 2018, pp. 1–53.

List of Publications

I. "Highly birefringent gold-coated SPR sensor with extremely enhanced amplitude and wavelength sensitivity," *Eur. Phys. J. Plus* (Impact Factor: **3.228**), vol. 136, no. 2, p. 238, Feb. 2021, DOI: https://doi.org/10.1140/epjp/s13360-021-01220-6
[*NB: This work has been discussed in chapter 7 of this book*]

II. "Design and Analysis of a Biochemical Sensor Based on Surface Plasmon Resonance with Ultra-high Sensitivity," *Plasmonics* (Impact Factor: **2.335**), Jan. 2021, DOI: https://doi.org/10.1007/s11468-020-01355-9
[*NB: This work has been discussed in chapter 9 of this book*]

III. "Design of a fabrication friendly highly sensitive surface plasmon resonance-based photonic crystal fiber biosensor," *Results Phys.* (Impact Factor: **4.019**), vol. 19, p. 103501, Dec. 2020, DOI: https://doi.org/10.1016/j.rinp.2020.103501
[*NB: This work has been discussed in chapter 8 of this book*]

IV. "Design and analysis of birefringent SPR based PCF biosensor with ultra-high sensitivity and low loss," *Optik* (Impact Factor: **2.187**), vol. 221, p. 165311, Nov. 2020, DOI: https://doi.org/10.1016/j.ijleo.2020.165311
[*NB: This work has been discussed in chapter 6 of this book*]

V. "Highly Birefringent Slotted Core Photonic Crystal Fiber for THz Wave Propagation," *Phys. Wave Phenom.* (Impact Factor: **0.745**), vol. 28, no. 1, pp. 58–67, Jan. 2020, DOI: https://doi.org/10.3103/S1541308X20010021